

UNIVERSITY OF CALIFORNIA

Santa Barbara

Overhauser Dynamic Nuclear Polarization to Study Hydration Dynamics

A Dissertation submitted in partial satisfaction of the
requirements for the degree Doctor of Philosophy
in Physics

by

Brandon Dean Armstrong

Committee in charge:

Professor Mark Sherwin (co-chair)

Professor Songi Han (co-chair)

Professor Andrew Cleland

Professor Philip Pincus

Professor Frederick Dahlquist

June 2010

The dissertation of Brandon Dean Armstrong is approved.

Songi Han

Andrew Cleland

Philip Pincus

Frederick Dahlquist

Mark Sherwin, Committee Co-Chair

May 2010

Acknowledgments

I thank Songi Han for being the driving force behind the work presented here. She is never short of ideas yet she gave me the independence to pursue my own scientific interests. Her positive attitude and enthusiasm for both the small and big successes made my graduate experience more enjoyable and rewarding.

The work presented here is also the work of many collaborators. I thank all my co-authors for their contributions and valuable insights. I especially thank Elliot Brown for his design of the microwave amplifier in chapter three and Silvia Cavegnero for providing samples and expertise for the work in chapter 4. I thank Mark Sherwin, Susumu Takahashi, Louis Claude Brunel, and Johan van Tol, who volunteered much of their time to help me understand and design the quasi-optical bridge of Chapter Five. Bruce Dunson, Terry Hart, Mike Johnson, and Richard Bock built much of the equipment used in these experiments and also contributed to their design. I thank all members of the Han group from 2005 to 2010 for many helpful discussions. I thank Colin Shepherd, Matt Shepard, Greg Dyer, Joe Paul, Charlie Wickersham, Ken Shen, and Gang Chen, with whom I spent many nights working on homework assignments. I thank Beth Wynstra for her wonderful support. I also thank my committee for taking time to critique my advancement exam and read this thesis.

I thank my mom and dad who taught me to always work hard. By encouraging me to be curious and to try and solve problems myself, they laid the foundation for my pursuit of physics. Thank you for all your love and support. This dissertation is as much a reflection of your hard work as it is mine.

VITA of Brandon Dean Armstrong

May 2010

EDUCATION

B.S. in Applied Mathematics, University of Northern Illinois, May 2004

B.S. in Physics, University of Northern Illinois, May 2004

Doctor of Philosophy in Physics, University of California, Santa Barbara, June 2010
(expected)

SCHOLARLY PRESENTATIONS

Invited Speaker: Magnetic Resonance Gordon-Kenan Research Seminar, University of New England (June 2009). “Water Dynamics of Apomyoglobin Folding using Dynamic Nuclear Polarization.”

Seminar Speaker: Chemistry Seminar, Massachusetts Institute of Technology (2008). “Dynamic Nuclear Polarization to Study Local Water Dynamics.” Guest of Robert Griffin.

Seminar Speaker: National High Magnetic Field Laboratory, Tallahassee, FL. (2007) “DNP as a Tool for Unique NMR Contrast.” Guest of Johan van Tol.

AWARDS AND RECOGNITION

Institute for Quantum and Complex Dynamics Travel Award: UC — Santa Barbara (2009).

Materials Research Laboratory Travel Fellowship: UC — Santa Barbara (2008)

Experimental Nuclear Magnetic Resonance Conference Travel Award (2007)

Dean’s Award: Northern Illinois University (2003)
Nominated by department for campus award

University Scholar Award: Northern Illinois University (2001)
Full tuition plus room and board scholarship for two years

PUBLICATIONS

- B.D. Armstrong**, J. Choi, C. J. López, D. Wesener, W. L. Hubbell, S. Cavagnero, and S. Han, "Site-Specific Hydration Dynamics in Native, Molten Globular and Unfolded Apomyoglobin," *in preparation*
- B.D. Armstrong**, D. T. Edwards, R. J. Wylde, S. A. Walker, and S. Han, "A 200 GHz dynamic nuclear polarization spectrometer," *Phys. Chem. Chem. Phys.* doi: 10.1039/c002290j
- S. Garcia, J. H. Walton, **B.D. Armstrong**, S. Han, and M. J. McCarthy, "L-band Overhauser dynamic nuclear polarization," *J. Magn. Reson.* 203 (2010) 138-143
- B.D. Armstrong**, P. Soto, J-E. Shea, and S. Han, "Overhauser dynamic nuclear polarization and molecular dynamics simulations using pyrroline and piperidine ring nitroxide radicals," *J. Magn. Reson.* 200 (2009) 137-141
- B.D. Armstrong**, and S. Han, "Overhauser Dynamic Nuclear Polarization to Study Local Water Dynamics," *J. Am. Chem. Soc.* 131 (2009) 4641-4647
- E.R. McCarney, **B.D. Armstrong**, R. Kausik, and S. Han, "Dynamic Nuclear Polarization Enhanced Nuclear Magnetic Resonance and Electron Spin Resonance Studies of Hydration and Local Water Dynamics in Micelle and Vesicle Assemblies," *Langmuir* 24 (2008) 10062-10072.
- S. Han, E.R. McCarney, and **B.D. Armstrong**, "Dynamic Nuclear Polarization Studies of Local Water Dynamics at 9.8 GHz," *Appl. Magn. Reson.* 34 (2008) 439-451.
- B.D. Armstrong**, M.D. Lingwood, E.R. McCarney, E.R. Brown, P. Blümler, and S. Han, "Portable X-band system for solution state dynamic nuclear polarization," *J. Magn. Reson.* 191 (2008) 273-281.
- S. Han, E.R. McCarney, **B.D. Armstrong**, and M.D. Lingwood, "Dynamic Nuclear Polarization-Enhanced Magnetic Resonance Analysis at X-Band Using Amplified ^1H Water Signal" (2008), In S.L. Codd and J. D. Seymour (Eds.), *Magnetic Resonance Microscopy: Spatially Resolved NMR Techniques and Applications* (pp. 161-176). Weinheim, Germany: Wiley-VCH
- B.D. Armstrong**, R. Kausik, and S. Han, "Local Hydration Dynamics in Soft Matter by Dynamic Nuclear Polarization of ^1H -water," *Magnetic Resonance in Porous Media: Proceedings of the 9th International Bologna Conference on Magnetic Resonance in Porous Media, AIP Conf. Proc.*, 1081 (2008) 14-17.

- B.D. Armstrong**, and S. Han, "A New Model for Overhauser-Enhanced Nuclear Magnetic Resonance Using Nitroxide Radicals," *J. Chem. Phys.* 127 (2007) 104508-10.
- E.R. McCarney, **B.D. Armstrong**, M.D. Lingwood, and S. Han, "Hyperpolarized Water as an Authentic Magnetic Resonance Imaging Contrast Agent," *Proc. Nat. Acad. Sci. USA.* 104 (2007) 1754-1759.
- B. Dabrowski, O. Chmaissem, P.W. Klamut, S. Kolesnik, M. Maxwell, J. Mais, Y. Ito, **B.D. Armstrong**, J.D. Jorgensen, and S. Short, "Reduced Ferromagnetic Transition Temperatures in SrRu_{1-x}O₃ Perovskites from Ru-site Vacancies," *Phys. Rev. B.* 70 (2004) 014423.

ABSTRACT

Overhauser Dynamic Nuclear Polarization to Study Hydration Dynamics

By

Brandon Dean Armstrong

Hydrophobic and hydrophilic interactions of water with biomolecules are known to mediate important processes such as protein folding, protein aggregation, and the formation of lipid bilayers and vesicles. Yet the exact role water plays in many biological processes is complex, spanning a large range of length and timescales, and is not well understood in quantitative detail despite extensive interest and decades of study. Experimentally, water – surface interactions are difficult to study as water lubricating a protein surface or moving across a membrane does not have a unique spectroscopic signature. While nuclear magnetic resonance (NMR) is an ideal technique for studying biological systems since it is non-invasive and uses low energy radio frequencies to irradiate the sample, it cannot differentiate between bulk and surface water. To overcome this obstacle, I advanced dynamic nuclear polarization (DNP) as a technique to study water interactions with biomolecules. I present here my work to develop a new theoretical model to quantify DNP experiments, apply DNP to experimentally measure the timescale of water interactions in an intermediate state of a protein, and in designing and building hardware to improve DNP performance and extend these techniques to large magnetic fields.

TABLE OF CONTENTS

I. Overhauser Dynamic Nuclear Polarization	
A. Motivation.....	1
B. Theory of the Overhauser Effect	8
C. Modeling the Overhauser Effect.....	15
D. Spin Labeled Electron Paramagnetic Resonance.....	24
II. The Overhauser Effect with Nitroxide Radicals	
A. Introduction.....	28
B. A new model describing the saturation factor.....	30
C. Results and Discussion.....	35
D. Conclusion.....	47
E. Materials and Methods.....	48
III. Portable DNP and Improved Hardware	
A. Introduction.....	51
B. Results and Discussion.....	52
C. Conclusion.....	61
D. Materials and Methods.....	62
IV. Site Specific Hydration Dynamics of Apomyoglobin	
A. Introduction.....	66
B. Results and Discussion.....	69
C. Conclusion.....	80

D. Materials and Methods.....	82
V. A 200 GHz Quasi-Optical DNP and EPR Spectrometer	
A. Introduction.....	88
B. Experimental.....	91
C. Results and Discussion.....	98
D. Conclusion.....	105
VI. Conclusion.....	107
References.....	110

I. Overhauser Dynamic Nuclear Polarization

A. Motivation

Nuclear magnetic resonance (NMR) is a powerful spectroscopic technique with applications ranging from reaction monitoring [1, 2], protein structure determination [3], medical imaging [4], and even quantum computing applications [5]. As the NMR experiment is both non-invasive and uses low energy radio frequency (RF) irradiation to excite the nuclear spins, it is an ideal tool for the study of biological samples and processes at ambient temperatures. However, NMR suffers from an inherent lack of sensitivity due to the small thermal polarization of nuclear spins which follow Boltzmann statistics. For example, the world's largest NMR spectrometer currently operates at 23.5 T. At room temperature the ^1H nuclear spin polarization at this field is still only 0.008%. Sensitivity becomes even more problematic with other nuclei which are less abundant and have smaller gyromagnetic ratios. Additionally, spectral overlap of the signal from like nuclei can complicate the spectra requiring two and three dimensional techniques to separate the peaks. The result is that some experiments can be prohibitively time consuming requiring days or weeks of signal averaging, and in some cases cannot be performed at all due to lack of sensitivity. It is a testament to the wealth of information available from an NMR experiment that it is one of the most widely used spectroscopic techniques despite these shortcomings.

Of all the efforts put into improving the sensitivity of an NMR experiment, Dynamic Nuclear Polarization (DNP) offers the largest potential gain. DNP is the process by which an unpaired electron transfers its larger spin polarization to dipolar

or scalar (Fermi-contact) coupled nuclei, thereby enhancing the NMR signal by 2-3 orders of magnitude. The process was originally predicted in 1953 by Albert Overhauser for conduction electrons and nuclei in metals [6] and quickly verified experimentally by Carver and Slichter [7]. It was soon found that the effect was not confined just to metals but also to diamagnetic crystals and paramagnetic molecules in solution [8]. The e^- spin polarization can be transferred to a coupled nuclear spin through several DNP mechanisms: the Overhauser Effect (OE) [6], the solid effect [9, 10], thermal mixing [10, 11], and the cross effect [12]. The OE is effective when the strength of the dipolar or scalar coupling is modulated by relative motion of the e^- and nuclear spin. If the timescale of this motion is $\lesssim 1/\omega_e$, where ω_e is the e^- Larmor frequency, then transitions involving mutual e^- - nuclear spin flips will occur with a high probability, and the e^- spin polarization can be transferred to the nuclei by irradiation of the e^- resonance transition.

The other three DNP mechanisms occur in insulating solids where the dipolar or scalar coupling is essentially static or modulated very slowly. In this case, transitions involving mutual e^- - nuclear spin flips are forbidden. In the solid effect, the width of the e^- spin resonance is narrow compared to the nuclear Larmor frequency, ω_n . Perturbation theory gives a small mixing of the energy levels such that high power irradiation at $\omega = \omega_e \pm \omega_n$ can drive these 'forbidden' transitions, thereby enhancing the NMR signal. Both thermal mixing and the cross effect can occur in systems where the width of the e^- resonance is on the order of, or broader than ω_n . In each case, the application of off-resonant irradiation of the electron resonance line induces mutual

spin flips of two e^- spins separated in frequency by ω_n , resulting in enhanced (positive or negative) NMR signal. In the case of thermal mixing the e^- spin resonance is homogeneously broadened, while the cross effect describes the situation where the e^- spin resonance is inhomogeneously broadened due to \mathbf{g} or \mathbf{A} anisotropy.

The overall focus of this dissertation is on using DNP to study the dynamics between an e^- spin and nuclear spin, with a particular emphasis on hydration water surrounding biological molecules. As the OE is the only DNP mechanism that is effective in liquids, it forms the basis for most of the experiments presented in this work. Therefore, a detailed description will be given in the next two sections. We define hydration water as water molecules that have their translational, rotational, and hydrogen bonding dynamics perturbed by the presence of a surface. The interaction of water with hydrophobic and hydrophilic regions of biomolecules is known to play an important role to mediate processes such as protein folding, protein aggregation, and the formation and stabilization of lipid bilayers. However, as hydration water does not have a unique spectroscopic signature, there is a lack of experimental techniques capable of measuring the dynamics of water on the heterogeneous surface of a protein or macromolecular assembly with site-specificity. For example, both electron paramagnetic resonance (EPR) and femto-second fluorescence spectroscopy have been applied to study local water dynamics on the surface of proteins [13-16]. Both methods, however, indirectly measure local water dynamics and are sensitive not only to the local motion of water, but also to the local structure of the protein (e.g. alpha-helix or beta-sheet), complicating the interpretation of results.

In the Han group, we propose attaching a free radical (molecule with an unpaired e^-) with site specificity to biomolecules, and then use DNP to directly measure the ^1H NMR signal enhancement of water. The dipolar interaction that causes the DNP effect is short range, with 80% of the relaxation occurring within 5 Å [17], so the ^1H signal enhancement is heavily weighted to water close to the surface. As will be shown, the NMR signal enhancement from DNP is strongly dependent on the distance of closest approach between the two spin bearing molecules, d , and the local diffusion of water. Thus, DNP can provide a measure of local water dynamics.

Several necessary steps were needed to achieve the goal of using DNP to study local water dynamics. First, the existing theory of the DNP parameter known as the saturation factor (to be defined shortly) for experiments using nitroxide free radicals (which have a nitrogen covalently bonded to an oxygen with an unpaired e^- ; see Fig. 1.2) as the source of unpaired electrons was inadequate to explain our experimental results. Nitroxide radicals will be discussed in more detail later, but they are a very important class of free radicals because they are stable, soluble in water, and are easy to covalently bind to biomolecules with site specificity. In chapter two, I show the shortcoming of the existing DNP theory. I then detail a modified description of the saturation factor and show experimental evidence to support the new model [18, 19].

In chapter three I detail our work on developing hardware for maximizing DNP signal enhancements. The original motivation for this work was to produce larger DNP enhancements for magnetic resonance imaging experiments. Our work in improving hardware resulted in nearly a factor of three improvement in our DNP

signal enhancements compared to a commercially available X-band (8 - 12 GHz) EPR bridge. Additionally, the setup was made portable by means of a tunable 9.5 – 10 GHz microwave cavity and a variable field Halbach magnet [20] allowing the necessary equipment to easily be taken to an imaging facility rather than having a dedicated instrument. However, for theoretical and practical reasons to be discussed, 0.35 T is a good choice of magnetic field to study local water dynamics with the OE, and our custom X-band amplifier has become a piece of standard equipment in our group's studies on hydration dynamics.

Armed with new theory and improved hardware, chapter four summarizes our work on applying this new technique to a sample of biological importance. Sperm whale apomyoglobin (apoMb) is widely studied in protein folding experiments because it has a stable intermediate that can be populated at low pH and salt concentrations. Most importantly, the stable intermediate closely resembles a kinetic folding intermediate allowing a wide range of experimental techniques to be used to study what is normally a short lived state [21]. Though apoMb is widely studied, it is unknown if water is excluded from the hydrophobic core of the stable intermediate. This is an important question since protein folding models differ on whether the exclusion of water occurs after the initial collapse of a hydrophobic core or after the protein has found its native structure. In chapter four, our DNP results show strong evidence for a hydrated hydrophobic core in the intermediate state of apoMb. In addition to the work presented here, this new technique has been applied in our group

to study water diffusion across membranes [22, 23], inside coacervates [24], and to elucidate early forming species in the aggregation of tau protein [25].

While the experiments presented in chapters two through four were done at 0.35 T, most NMR experiments are done at much higher magnetic fields due to increased spin polarization and greater spectral resolution. Despite the wide range of samples that DNP experiments could be applied to at high magnetic fields (arbitrarily defined here as > 5 T), the technique has not been widely used, largely due to hardware difficulties. DNP requires resonant or near resonant irradiation of the electron Larmor frequency. Magnetic fields up to 16 T are commonly used in NMR experiments which would require a 450 GHz source for DNP experiments to be implemented. The problem is not just limited to the availability of high frequency sources, but other challenges must be overcome such as dielectric absorption by the sample, high microwave power needed to excite broad electron spin resonances, and difficulties building the necessary RF and microwave equipment into the bore of a superconducting magnet without sacrificing spectral resolution. Recent technological developments in microwave technologies [26, 27] have renewed interest in high field DNP. The wider availability of hardware and increased interest has led to several commercial instruments, notably, a 9 T gyrotron-based system from Bruker Biospin for solid state magic angle spinning experiments (ssMAS) and a diode-based, 1.1 K dissolution DNP setup for liquid state spectroscopy from GE and Oxford. In the latter, the sample is cooled to 1.1 K during microwave irradiation in a 3.35 T magnet and then quickly dissolved and shuttled to a high resolution NMR magnet. The

former uses a gyrotron to produce high power (several watts) 250 GHz irradiation and over-moded waveguides to propagate the microwaves to the sample inside a ssMAS probe in a 9 T magnet. Both systems are expensive, require significant lab space, and do not incorporate the ability to detect the EPR signal of the sample which can also contain a wealth of information about electron-nuclei interactions. In chapter five we detail our work to bridge this cost—space—EPR gap with the development of a 7 T DNP and EPR spectrometer based on quasi-optical techniques with a low power, 200 GHz diode source. In this chapter we present our initial DNP and EPR results on a test sample at 4 K. Our experimental design allows for EPR and NMR detection in the same setup without changing the sample. Also, we show the benefit of using quasi-optical techniques for microwave propagation as the polarization of incident radiation can be changed to maximize DNP enhancements or isolate the small EPR signal from the large background.

As previously mentioned, all of the work at low field relies on the OE. As the goal of these experiments is to understand the dynamics of water on biological surfaces, an understanding of the theory is necessary. I therefore dedicate the next two sections to the theory of the OE and paramagnetic relaxation by dissolved solutes. I end this introductory chapter by giving a brief introduction to EPR with spin labeled molecules because, as I show in chapter four, EPR and DNP can give complementary information and together paint a more complete picture of the dynamics of proteins.

B. Theory of the Overhauser Effect

The Hamiltonian for two coupled spins, \mathbf{I} and \mathbf{S} , in a magnetic field is given by Equation 1.1 [28]. Though the equation is general for any two spins, the focus in this dissertation is on the coupling between an unpaired electron spin, \mathbf{S} , and nuclear spin, \mathbf{I} , and this will be assumed throughout unless otherwise stated.

$$H = \hbar\gamma_s(\mathbf{S}\cdot\mathbf{H}_0) + \hbar\gamma_I(\mathbf{I}\cdot\mathbf{H}_0) + H_s + H_d \quad (1.1a)$$

$$H_s = \frac{\gamma_s\gamma_I\hbar^2 8\pi}{3} |\psi(0)|^2 (\mathbf{I}\cdot\mathbf{S}) \quad (1.1b)$$

$$H_d = \gamma_s\gamma_I\hbar^2 \left[\frac{\mathbf{I}\cdot\mathbf{S}}{r^3} - \frac{3(\mathbf{I}\cdot\mathbf{r})(\mathbf{S}\cdot\mathbf{r})}{r^5} \right] \quad (1.1c)$$

The first two terms of Eq. 1.1a describe the Zeeman interaction of the spins in the applied magnetic field, \mathbf{H}_0 . H_s is known as the scalar interaction, though in some contexts it is referred to as the Fermi-contact term. The strength of the scalar interaction depends on the probability of the e^- being at the position of the nucleus, $|\psi(0)|^2$. In general, this is not known, making the scalar interaction difficult to predict except in simple situations [29]. The final term, H_d , describes the dipolar interaction between two magnetic moments where r is the distance between the two spins. The experiments described in this work are dominated by the dipolar interaction so it is worth discussing this term in some detail. By evaluating the dot products in Eq. 1.1c, converting I_x , I_y , S_x , and S_y to raising and lowering operators, and writing \mathbf{r} in spherical coordinates, (r, θ, ϕ) , the effect of H_d is more easily observed [28].

$$H_d = \frac{\gamma_s \gamma_I \hbar^2}{r^3} (A + B + C + D + E + F) \quad (1.2a)$$

$$A = I_z S_z (1 - 3 \cos^2 \theta) \quad (1.2b)$$

$$B = -\frac{1}{4} (I^+ S^- + I^- S^+) (1 - 3 \cos^2 \theta) \quad (1.2c)$$

$$C = -\frac{3}{2} (I^+ S_z + I_z S^+) \sin \theta \cos \theta e^{-i\phi} \quad (1.2d)$$

$$D = -\frac{3}{2} (I^- S_z + I_z S^-) \sin \theta \cos \theta e^{i\phi} \quad (1.2e)$$

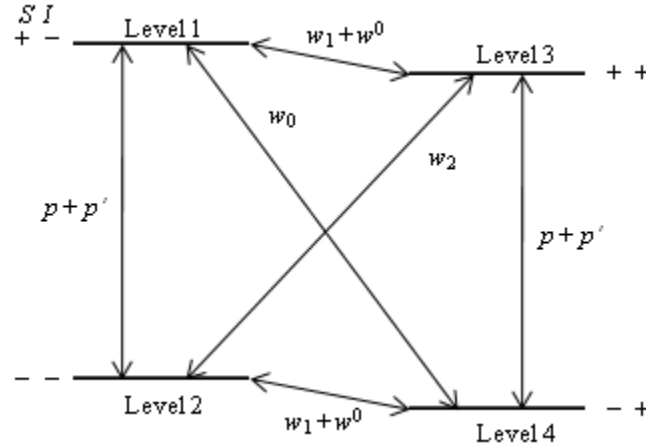
$$E = -\frac{3}{4} I^+ S^+ \sin^2 \theta e^{-2i\phi} \quad (1.2f)$$

$$F = -\frac{3}{4} I^- S^- \sin^2 \theta e^{2i\phi} \quad (1.2g)$$

It is now clear that H_d can cause mutual spin transitions. Let us assume, not only for simplicity of the discussion, but also because it is appropriate for the OE experiments in this work, that spin \mathbf{I} is a ^1H nuclear spin, $1/2$. We also assume that the magnetic field is large enough that the energy of the Zeeman interaction is much greater than H_s or H_d so they can be treated as a perturbation. We can then assume a four level energy diagram as shown in Fig. 1.1. Term B in Eq. 1.2 is responsible for the zero quantum transition, w_0 . Terms C and D flip only the e^- or ^1H nucleus and are shown as w_1 and p' . Finally terms E and F represent the double quantum transition, w_2 , where both spins flip in the same direction. It is important to note that the $(\mathbf{I} \cdot \mathbf{r})(\mathbf{S} \cdot \mathbf{r})$ term in Eq. 1.1c is responsible for the double quantum transition. Therefore, if H_s is the only important coupling term in the Hamiltonian then only the w_0 , w_1 , and p' transitions are possible, while for pure dipolar coupling, all the transitions shown are

all possible. Determining these transitions rates is very important and will be discussed in the next section. For now I will assume only that these transitions exist. Lastly, there are relaxation mechanisms of the electron and ^1H nuclear spins that are not due to scalar or dipolar coupling, and these transition rates are denoted $w^0 = 1/T_{10}$ and $p = 1/T_{1e}$, where T_{10} and T_{1e} are the longitudinal relaxation times of the nucleus and electron in the absence of any coupling between them. Also, the electron spin has much stronger relaxation mechanisms other than dipolar coupling to the nucleus so the assumption $p \gg p'$ will be made.

Figure 1.1. Four level energy diagram for two coupled spin $\frac{1}{2}$'s, appropriate for an electron and nucleus with a positive gyromagnetic ratio such as ^1H .



Given these transition probabilities, we can write equations for the time rate of change of the population of each energy level by adding together the different relaxation pathways in or out of that particular level. As an example, the equation for the population of level 1 (n_1) is given in Eq. 1.3 with similar equations for the other three energy levels.

$$\frac{dn_1}{dt} = -(p + w_0 + w_1 + w^0)n_1 + pn_2 + (w_1 + w^0)n_3 + w_0n_4 \quad (1.3)$$

In an NMR experiment the net magnetization, $\langle I_z \rangle$, is measured which is the total number of spin up nuclei minus the number of spin down.

$$\langle I_z \rangle \propto n_3 + n_4 - (n_1 + n_2) \quad (1.4)$$

Using Eq. 1.3 (and the equations for n_2 , n_3 , and n_4), and Eq. 1.4 we can write,

$$\frac{d\langle I_z \rangle}{dt} = -(w_0 + 2w_1 + w_2 + w^0)(\langle I_z \rangle - I_0) - (w_2 - w_0)(\langle S_z \rangle - S_0) \quad (1.5)$$

where I_0 and S_0 are the nuclear and electron spin equilibrium magnetizations. This is one of the famous Solomon equations for describing the magnetization of two dipolar coupled spin $\frac{1}{2}$'s [30]. There is of course a similar equation for the electron, but because the electron spin has other strong relaxation mechanisms not due to coupling with the nucleus we can ignore it. Using the relation $S_0/I_0 = \gamma_s/\gamma_I$, we can define the NMR signal enhancement, $E = \langle I_z \rangle/I_0$, in the steady state by rearranging the terms in Eq. 1.5.

$$\frac{\langle I_z \rangle}{I_0} = E = 1 - \rho f s \frac{|\gamma_s|}{\gamma_I} \quad (1.6a)$$

$$\rho = \frac{w_2 - w_0}{w_0 + 2w_1 + w_2} \quad (1.6b)$$

$$f = \frac{w_0 + 2w_1 + w_2}{w_0 + 2w_1 + w_2 + w^0} \quad (1.6c)$$

$$s = \frac{S_0 - \langle S_z \rangle}{S_0} \quad (1.6d)$$

In these equations ρ is known as the coupling factor, f is the leakage factor and is the ratio of the dipolar relaxation rate to the total relaxation rate, and s is the saturation factor.

The most striking feature of Eq. 1.6a is the ratio $|\gamma_S|/\gamma_I$, which for an electron spin and ^1H nuclear spin is ~ 660 . It is therefore possible to achieve a large NMR signal enhancement by irradiating the electron spin resonance and driving $\langle S_z \rangle$ away from its thermal equilibrium value and towards 0. Assuming the validity of the Bloch equations for the electron spin [31] and on-resonant irradiation of the EPR transition, the saturation factor can be written as function of the applied radiation power,

$$s = \frac{\alpha P}{1 + \alpha P} \quad (1.7)$$

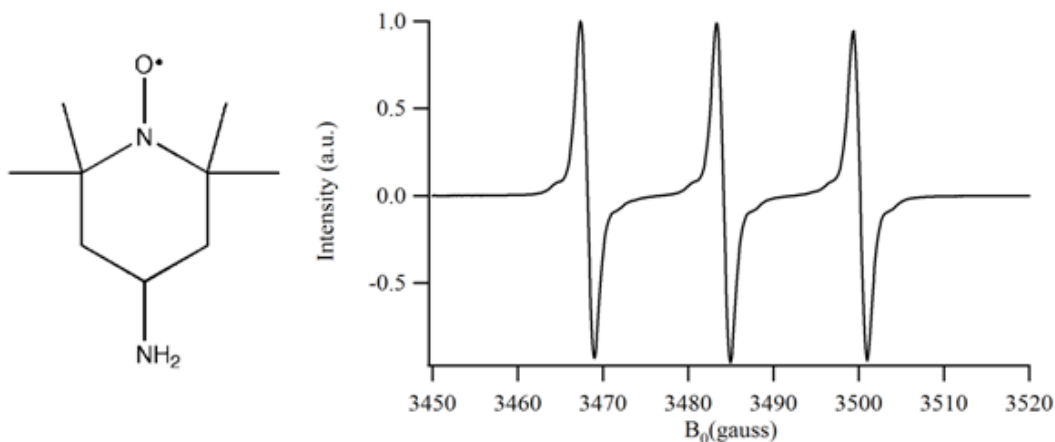
where α is a constant related to the electron spin relaxation times, T_{1e} and T_{2e} , as well as the coil or cavity properties used to irradiate the sample [29]. To account for differences in the saturation factor due to different experimental setups or differences in applied power, a typical experiment consists of measuring the NMR signal enhancement as a function of power. The results are then extrapolated to infinite power using Eq. 1.7 (where $s \rightarrow 1$) to measure the maximum possible enhancement, $E_{\max} = E(P \rightarrow \infty)$.

An assumption in this discussion of the saturation factor is that the species containing the unpaired electron has only a single resonance line. This is often not the case due to hyperfine coupling of the electron spin to a nucleus with non-zero spin. A widely used family of free radicals in DNP and EPR experiments is nitroxide radicals. An example of a nitroxide radical is shown in Fig. 1.2 along with its EPR spectrum. There is a hyperfine interaction between the unpaired electron and the spin = 1 ^{14}N nucleus, giving the 3-line EPR spectrum. A standard EPR spectrometer operates at X-band, so resonant cavities are typically employed to irradiate the sample. The use of a

cavity implies only a single line of the EPR spectrum can be irradiated due to the narrow bandwidth. Also, the nuclear spin polarization is very low, so the electron spin population is equally distributed among the three spin states of the ^{14}N nucleus. This is easily seen by the nearly equal intensities of the EPR spectrum in Fig. 1.2.

Therefore, the saturation factor is usually modified by multiplying Eq. 1.7 by a factor of $1/n$ where n is the number of hyperfine lines. The maximum saturation factor for nitroxide radicals is then $\frac{1}{3}$ instead of 1. This assumption will be shown to be incorrect in Chapter 2 where a new saturation factor is derived for nitroxide radicals.

Figure 1. 2. Chemical structure of the radical 4-Amino-Tempo and an X-band EPR spectrum taken in a TE_{102} resonant cavity. The B_0 field is modulated at 100 kHz and slowly swept while the sample is continuously irradiated with microwaves, so the 1st derivative of the absorption signal is measured.



In many cases, the leakage factor can be easily determined. The denominator of Eq. 1.6c is just the sum of the different longitudinal relaxation rates, that is, $1/T_1 = w_0 + 2w_1 + w_2 + w^0$. Remembering that w^0 is the relaxation rate in the absence of dipolar or scalar coupling we can rewrite Eq. 1.6c as

$$f = 1 - \frac{T_1}{T_{10}} \quad (1.8).$$

For samples where a paramagnetic solute is being used to hyperpolarize the solvent, f can be determined by measuring the longitudinal nuclear spin relaxation in the presence of the paramagnetic species (T_1) and absence of the paramagnetic species (T_{10}). Thus, the leakage factor is a measure of how effectively the e^- relaxes the nuclei compared to other mechanisms. In the limit that all nuclear spin relaxation occurs via coupling to the electron spin, $T_1 \ll T_{10}$ and f approaches 1. The total relaxation rate caused by the e^- spins obviously depends on the concentration of electron spins. For a dilute concentration of electron spins compared to the nuclei, all dipolar relaxation rates are all linear in e^- spin concentration. We can then write Eq. 1.6c as

$$f = \frac{kCT_{10}}{1 + kCT_{10}} \quad (1.9),$$

where k is known as the relaxivity constant and C is the unpaired e^- concentration.

The coupling factor is so named because it provides information on the type of interaction between the electron spin and nuclear spin. If the coupling is purely scalar, the double quantum transition does not exist, and ρ is negative. If the coupling is purely dipolar, then $w_2 > w_0$ (this will be shown in the next section) and ρ is positive. Additionally, as Eq. 1.6b contains only transitions rates caused by coupling to the e^- spin, there is no concentration dependence in ρ . This makes ρ the fundamental parameter to determine from an Overhauser DNP experiment. The transition rates, w_0 , w_1 , and w_2 , contain information on the type of coupling as well as the dynamics modulating the coupling. It is therefore important to calculate these transition rates so that useful information can be extracted.

C. Modeling the Overhauser Effect

In the previous section, we showed that both s and f can approach one, and thus large NMR signal enhancements are possible if there is efficient cross relaxation. In this section we show under what conditions this is in fact true. We also now narrow the focus to the dipolar coupling between an electron of a paramagnetic solute and the nucleus of a solvent. In this situation, the dipolar Hamiltonian, H_d , is time dependent due to the diffusion of molecules. This implies that \mathbf{I} , \mathbf{S} , and \mathbf{r} , are all functions of time. Since diffusion is a random process, H_d is stationary, so the evolution from time t to t' depends only on their difference, τ . The transition probability between two energy levels from time dependent perturbation theory is then [32]

$$w_{mn} = \int_{-\infty}^{\infty} \overline{\langle m|H_d(t)|n\rangle\langle n|H_d(t+\tau)|m\rangle} e^{-i\omega_{mn}\tau} d\tau \quad (1.10)$$

where the bar represents a statistical average. Eq. 1.10 looks like a Fourier transform, and we can define a spectral density function, $J(\omega)$, and a correlation function, $G(\tau)$,

$$J(\omega) = \int_{-\infty}^{\infty} G(\tau) e^{-i\omega\tau} d\tau \quad (1.11)$$

where

$$G(\tau) = G(-\tau) = \overline{\langle m|H_d(t)|n\rangle\langle n|H_d(t+\tau)|m\rangle} \quad (1.12).$$

The first equality of Eq. 1.12 is true because $G(\tau)$ is stationary. If the time dependence of r , θ , ϕ in Eq. 1.2 is known, the transition rates can be calculated. However, in general an exact calculation of the transition rates is not possible as not only the diffusion of the two molecules needs to be modeled, but also the electrostatic

forces interacting between them. Fortunately, the field of paramagnetic relaxation enhancement (PRE) is an active community with applications ranging from aiding in protein structure determination to magnetic resonance imaging (MRI) contrast agents, so much theoretical and experimental work has been done [33-42]. Three relatively straight forward scenarios exist that have relatively simple solutions and apply to a wide range of samples: a translational Brownian diffusion model where the spins are centered on hard spheres with no forces acting between them (force, free hard sphere model; FFHS, also referred to as the translational model) [36, 38], a rotational model where the two spins form a bound complex so that r is a constant and H_d is modulated by rotational motion [29, 32], and a model combining these two theories for samples that exhibit both types of relaxation [42]. In chapter two we show that the FFHS model approximates the nitroxide radical – ^1H of water system fairly well. We therefore calculate ρ and T_1 using this model to show the behavior of the DNP signal enhancement as a function of dynamics and magnetic field. We also compare these results to a simple rotational model to show how the two differ and how the different phases of motion may be separated.

The FFHS model is a simplified case of a more general treatment of paramagnetic relaxation developed by Hwang and Freed and remains a widely used model to describe dipolar relaxation in liquids mediated by translational diffusion. The important parameter describing the dynamics between the two spin bearing molecules is the translational correlation time defined as

$$\tau_t = \frac{d^2}{D_l + D_s} \quad (1.13)$$

where d is the distance of closest approach and D_I and D_S are the diffusion coefficients of the spin bearing molecules. Eq. 1.13 is important for determining local hydration dynamics with the OE. If we can determine τ_t from a DNP experiment, we can gain knowledge of the local diffusion of water. The FFHS model also included the spin lattice and spin-spin relaxation times of the electron. If these times are long compared to τ_t , which is the case for nitroxide radicals, they can be ignored and there is a single reduced spectral density function for all the dipolar transition rates [36],

$$j(\omega, \tau_t) = \frac{1 + \frac{5\sqrt{2}}{8}(\omega\tau_t)^{1/2} + \frac{\omega\tau_t}{4}}{1 + (2\omega\tau_t)^{1/2} + \omega\tau_t + \frac{\sqrt{2}}{3}(\omega\tau_t)^{3/2} + \frac{16}{81}(\omega\tau_t)^2 + \frac{4\sqrt{2}}{81}(\omega\tau_t)^{5/2} + \frac{(\omega\tau_t)^3}{81}} \quad (1.14)$$

(Note: In reference [36], equation 2 is correct, but in equation 4 the $(\omega\tau_t)^2$ term in the denominator is incorrectly missing). The total ^1H nuclear spin relaxation rate of water in this model is [43]

$$\frac{1}{T_1} = \frac{32\pi N_A}{4.05 \times 10^5} \gamma_I^2 \gamma_S^2 \hbar^2 S(S+1) C \frac{\tau_t}{d^3} [j(\omega_S - \omega_I, \tau) + 3j(\omega_I) + 6j(\omega_S + \omega_I)] + \frac{1}{T_{10}} \quad (1.15)$$

where S is the electron spin (1/2 for a nitroxide radical), N_A is Avogadro's number, C is the molar concentration, and ω_S and ω_I are the electron and ^1H angular Larmor frequencies.

The dominator of Eq. 1.6c is also the total relaxation rate, $w_0 + 2w_1 + w_2 + w^0$. The first term of Eq. 1.15 corresponds to the zero quantum transition rate, w_0 , the second term to $2w_1$ and the third term to w_2 . The zero and double quantum transitions

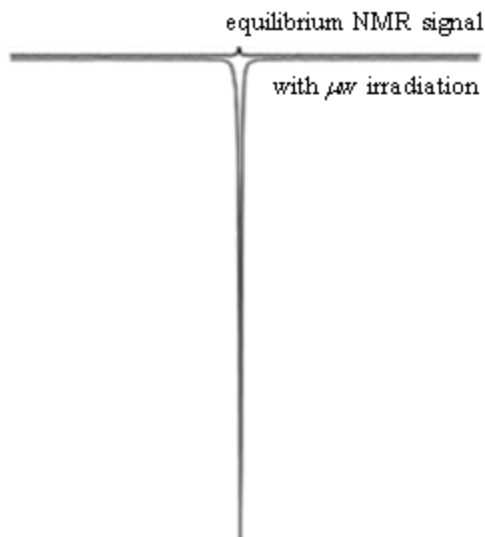
involve simultaneous electron – ^1H spin flips, and thus depend on ω_S , while the single quantum transition involves only a nuclear spin flip and therefore depends on ω_I . Since $\omega_S \gg \omega_I$, the double quantum transition rate is about six times larger than the zero quantum transition rate. Thus upon irradiation of the electron spin resonance, the population of level 2 in Fig. 1.1 will become more populated than level 4 due to preferential relaxation through w_2 , resulting in an NMR signal that is inverted compared to thermal equilibrium. An example of this is shown in Fig. 1.3 where a -130 fold signal enhancement of the ^1H nuclear spin of water was recorded at 0.348 T. We can also rewrite Eq. 1.6b in terms of the reduced spectral density function,

$$\rho = \frac{5j(\omega_S, \tau_t)}{7j(\omega_S, \tau_t) + 3j(\omega_I, \tau_t)} \quad (1.16)$$

where we have made use of the assumption $\omega_S \pm \omega_I \approx \omega_S$. By determining ρ in a DNP experiment, Eq. 1.16 can be used to calculate τ_t . Eqs 1.16, 1.14, and 1.13 form the foundation for using DNP to study hydration dynamics. By measuring the DNP signal enhancements, the leakage factor with Eq. 1.8, and determining the saturation factor with the model to be developed in chapter 2, ρ and τ_t can be calculated. It is important to remember that the coupling factor can be found from Eq. 1.6a without invoking a dynamic model. Additionally, Eq 1.16 is not specific to the FFHS model, but is applicable anytime the system can be described by a single spectral density function. This will be the case whenever the electron spin relaxation times do not contribute to the time dependence of H_d , i.e. T_{1e} and $T_{2e} \gg \tau_c$, the correlation time (for nitroxide radicals, T_{1e} , T_{2e} is typically tens of ns while τ_c is typically tens of ps).

Therefore determining ρ can still yield qualitative results even if an appropriate dynamic model is not known. Given the lack of experimental techniques capable of measuring hydration water, this makes DNP a particularly promising technique.

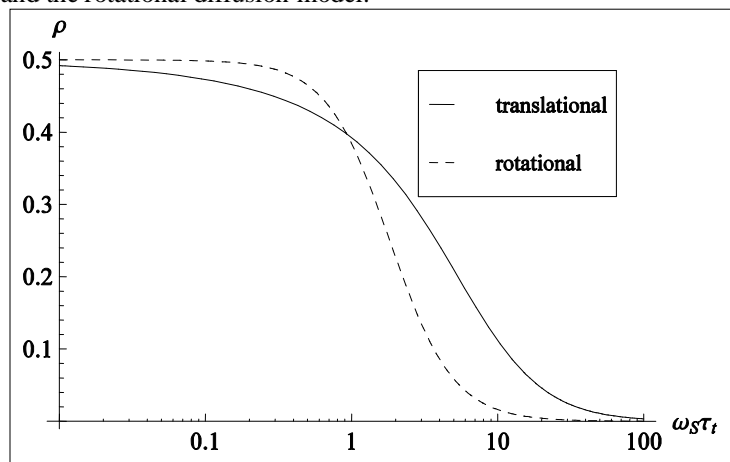
Figure 1.3. The 0.348 T ^1H NMR signal of water taken without (top trace) and with (bottom trace) irradiation of the center electron resonance for a 15 mM concentration of the nitroxide radical 4-oxo-Tempo dissolved in water. The signal enhancement is ~ 130 fold.



The result in Fig. 1.3 clearly shows that there is efficient cross relaxation at 0.35 T, but we have yet to show the behavior of the coupling factor with τ_t or ω . Furthermore, we also need an experimental test of the validity of the FFHS model if we are to use Eq. 1.16 to determine τ_t . Beginning with the former, it is easy to see from Eq. 1.14 that if $\omega\tau_t \ll 1$, then $j(\omega, \tau_t) \approx 1$ and $\rho = \frac{1}{2}$ from Eq. 1.16. This is the upper limit on ρ , so the maximum possible ^1H enhancement due to the OE from Eq. 1.6a is -330 fold. The coupling factor is plotted as function of $\omega_S\tau_t$ in Fig. 1.4 using the FFHS model (solid line). The shape of this curve is important for determining how sensitive Overhauser DNP is to changing dynamics through τ_t . For $1 < \omega_S\tau_t <$

30, ρ decreases rapidly with increasing values of $\omega_S\tau_t$, while outside this region, ρ varies slowly with $\omega_S\tau_t$. In our experiments at 0.35 T, the electron resonance frequency is ~ 9.8 GHz. From the above condition, the OE will be a good technique for studying translational dynamics on the timescale of $\sim 10 - 500$ ps. This timescale nicely covers the range of values other reports have found for the dynamics of hydration water [15, 16, 44-46]. Thus, from a theoretical standpoint, 0.35 T is a good choice of magnetic field to perform these experiments. It also turns out to be quite fortuitous as this is the standard field for EPR studies so that much of the hardware needed for DNP is commercially available.

Figure 1.4. Comparison of the field dependence of the coupling factor for the FFHS translational diffusion model and the rotational diffusion model.



The total relaxation rate (Eq. 1.15) contains the same information as the coupling factor and can also be used to study hydration dynamics, though it is experimentally more difficult. The method of nuclear magnetic resonance dispersion (NMRD) measures the relaxation rate of a system as a function of magnetic field, and uses the data to find the shape of the spectral density functions. Typically, milli-molar concentrations of nitroxide radicals are needed for an NMRD experiment due to the

concentration dependence of the relaxation rate. The solubility of proteins is generally lower than this, so it is difficult to generate much contrast in the field dependence of the relaxation data. DNP, on the other hand, is still a viable technique as the contrast generated is the ^1H NMR signal enhancement, and concentrations as low as $50\ \mu\text{M}$ of nitroxide radicals can still give measurable enhancement [18]. However, NMRD is a widely used and powerful technique because the relaxation curves can be used to distinguish different dynamic models. An example of this is shown in Fig. 1.5 where the FFHS model is compared to a rotational diffusion model to be discussed shortly. The initial decrease in the relaxation rate for both models is due to a decrease in w_0 and w_2 which fall off at lower magnetic fields due to their ω_S dependence. The w_1 transition doesn't begin to decrease rapidly until much later and causes the high field behavior. The field dependence of DNP data, in principle, also discriminates between diffusion models as seen by the different behavior of ρ with the translational and rotational models shown in Fig. 1.4. This is experimentally difficult to realize as several microwave sources and resonant structures would be needed to irradiate the electron resonance over a large enough field range to fit the data to a dynamic model.

Though the dipolar relaxation rates decrease monotonically with increasing field, this is not the case when looking at the relaxation rates as a function of τ_t at constant field. Fig. 1.6 shows the leakage factor with the FFHS model at 0.35 T for a $200\ \mu\text{M}$ concentration of free radical as a function of τ_t . At small values of τ_t , f is small while ρ is quite large as seen in Fig 1.4. If τ_t increases due to slower diffusion, as opposed to a larger d , then f begins to increase while ρ decreases. For large values of

Figure 1.5. Comparison of the dipolar relaxation rate due to translational motion and rotational motion. Each plot was made with the $\tau_c = 20$ ps and $C = 5$ mM. For the two models, $d = b = 2.5$ Å was used. The bound water lifetime was neglected in the calculation as explained in the text.

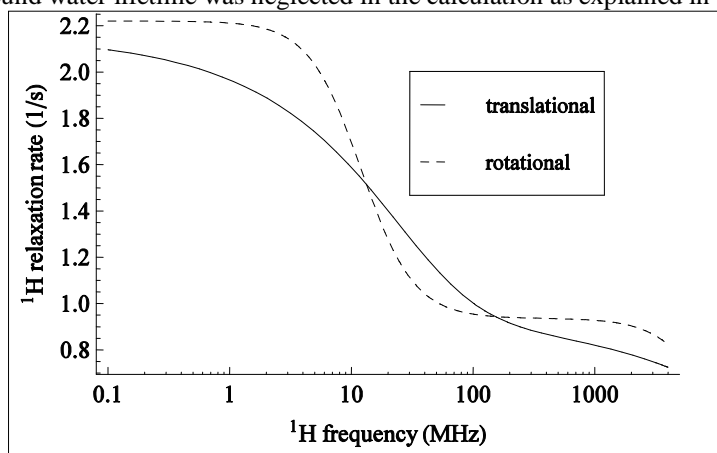
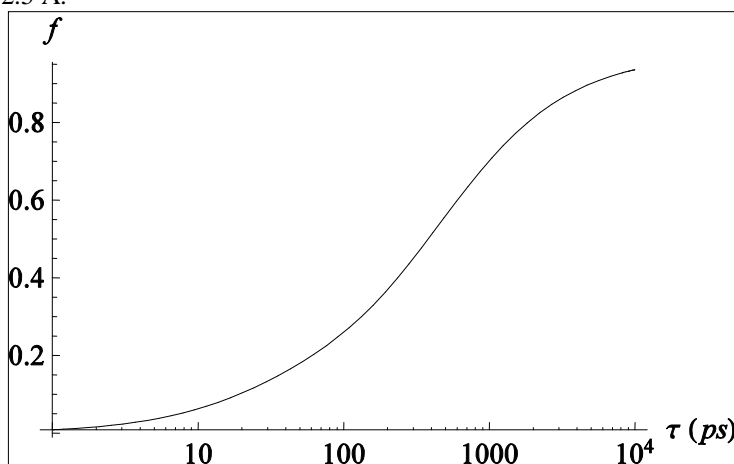


Figure 1.6. A plot of the leakage factor for the ^1H –electron system, using the FFHS model with $C = 200$ μM and $d = 2.5$ Å.



τ_t, f can approach 1 even for very small concentrations of radical, while ρ is nearly 0. This observation is important for interpreting DNP signal enhancements with Eq. 1.6a as will be discussed in chapter four with apoMb. It seems somewhat counter-intuitive at first that a larger leakage factor can result in smaller measured DNP enhancement, but this turns out to actually be the case *if* the increase in τ_t is due to slower local diffusion and not due to a change in the distance of closest approach, d . If the distance of closest approach increases, the relaxation rates also decrease, because of the factor

of $1/d^3$ in Eq. 1.15. Therefore, a decrease in ρ that is associated with an increase in f is likely due to slower local diffusion while a decrease in ρ accompanied by a similar or smaller f is more likely caused by an increase in d .

It is appropriate to briefly discuss dipolar relaxation mediated by rotational motion as some proteins are known to have strongly bound water molecules that tumble with the protein as a whole [47]. In this case, the distance between the e^- and ^1H nuclear spins is taken to be a constant and H_d is modulated by rotational diffusion.

The relaxation rate is given in 1.17a [42],

$$\frac{1}{T_1} = \frac{P_m}{T_{1m} + \tau_m} \quad (1.17a)$$

$$\frac{1}{T_{1m}} = \frac{\gamma_I^2 \gamma_S^2 \hbar^2}{10b^6} \tau_c (7j(\omega_S, \tau_c) + 3j(\omega_I, \tau_c)) \quad (1.17b)$$

$$j(\omega, \tau) = \frac{1}{1 + \omega^2 \tau^2} \quad (1.17c)$$

$$\frac{1}{\tau_c} = \frac{1}{\tau_r} + \frac{1}{\tau_m} \quad (1.17d)$$

where P_m is the mole fraction of bound water, which is proportional to concentration, b is the distance between the two spins when bound, τ_m is the lifetime of bound water, τ_r is the rotational correlation time of the bound complex, and $1/T_{1m}$ is ^1H relaxation rate in the bound complex. It has already been assumed in Eq. 1.17 that the spin of the electron is $1/2$ and $\omega_S \gg \omega_I$. Though the rotational model appears somewhat complicated because we have to account for the lifetime of the bound complex, it is often the case that $1/\tau_r \ll 1/\tau_m \ll 1/T_{1m}$ so that τ_m can be ignored. From Figs. 1.4 and 1.5, we can see that the spectral density function for rotational

motion remains fairly constant until higher fields than in the translational model, but then falls off much more rapidly as the magnetic field is increased. Because of this different behavior, NMRD experiments are useful for evaluating different relaxation models and will be done in the next chapter. Combining the two models for mixed modes of relaxation can be done by adding the relaxation rates together: $1/T_1 = (1/T_1)_{FFHS} + (1/T_1)_R + 1/T_{10}$.

As a final note for this section, it is now clear as to why the OE, though discovered in 1953, has not found widespread use in NMR spectroscopy (unlike the nuclear OE that is a standard technique in NMR). The coupling factor rapidly decreases at higher magnetic fields, and small sample volumes must be used to avoid dielectric absorption. The DNP signal enhancements at high field are not substantial enough to overcome the loss in sample volume or hardware difficulties. However, our focus is not on increasing absolute sensitivity, but on gaining information on the dynamics between the two spin bearing molecules. As the preceding discussion has shown, and chapters two through four will prove, DNP is well suited for this role.

D. Spin Labeled Electron Paramagnetic Resonance

Electron paramagnetic resonance using nitroxide spin labels (often referred to as electron spin resonance, ESR, with organic radicals) is widely used to study the structure and dynamics of biological systems [48]. Unlike NMR, EPR is not limited by the size of the paramagnetic label or spin labeled protein and can be used with μM sample concentrations. Hence, many proteins that are inaccessible to NMR can be studied with EPR. The same will be true for measuring hydration dynamics with DNP

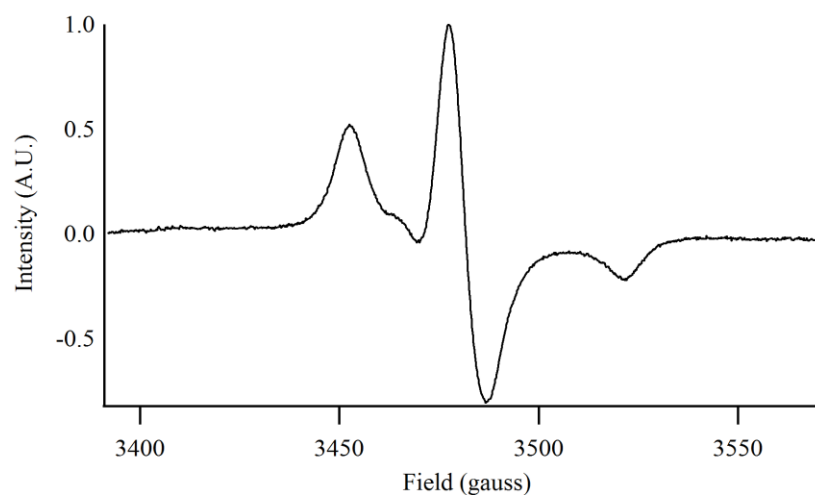
since the ^1H NMR signal of water, and not that of the protein, is being measured. EPR is also sensitive to a faster dynamic timescale than NMR due to the larger Larmor frequency of the electron spin. Protein conformational motions in the μs timescale, for example, are averaged in a NMR experiment, but show up as distinct peaks or changes in the lineshape of an X-band EPR spectrum. As our proposed method of measuring local water dynamics with DNP relies on spin labeled molecules, EPR is a natural technique to employ in our study of these systems. In chapter four we show how the two methods give quite complementary information and can be used together to narrow the possible interpretations of the results for complex systems. One important point is that EPR spectra are usually taken in continuous wave, meaning the sample is irradiated with low power microwaves at constant frequency while the B_0 field is swept slowly. A direct absorption peak could be measured, but to increase sensitivity, the B_0 field is usually modulated at 10—100 kHz and the signal detected with a lock—in amplifier. The resulting spectrum is the derivative of the absorption signal and most EPR spectra presented in this dissertation are derivative spectra.

The electron \mathbf{g} and \mathbf{A} tensor values (\mathbf{A} being the strength of the hyperfine interaction with the ^{14}N nucleus) of a nitroxide radical are anisotropic since the unpaired electron resides in a p-orbital. For fast rotational motion, (tens to hundreds of ps at 0.35 T) the \mathbf{g} and \mathbf{A} values are averaged, and the spectrum appears isotropic as in Fig. 1.2. As the tumbling of the nitroxide slows, the anisotropic values for \mathbf{g} and \mathbf{A} result in line broadening and spreading out of the spectrum. A rigid-limit powder spectrum of a nitroxide, shown in Fig 1.7, is drastically different from the liquid

spectrum in Fig 1.2. Thus, an EPR spectrum can be used to estimate rotational motion of molecules occurring on the nanosecond timescale at X-band. Additionally, the \mathbf{g} and \mathbf{A} tensor values depend on the local environment of the nitroxide. A_{zz} in particular is sensitive to local polarity [49-51]. Much effort has been put into calculating and fitting EPR spectra to gain information about the local dynamics of the molecule the label is attached to, such as protein backbone dynamics. This is not a trivial matter as there are many free parameters. In addition to \mathbf{g} -values, \mathbf{A} -values, and rotational motion, the lineshape can also be influenced by unresolved hyperfine couplings and local order parameters. At X-band excitation frequencies where most EPR is done, there is significant spectral overlap of these quantities, and care must be taken when fitting spectra and interpreting results. Nevertheless, the importance of spin labeled EPR of biological samples with nitroxide radicals has motivated the development of two programs to fit spectra, Easyspin [52] and NLSL [53-56]. Details of the fitting procedure will be given in chapter four where we use NLSL to estimate the local motions and polarity of apoMb.

Though an EPR spectrum contains a wealth of information about the local environment of the spin label, it is not directly measuring water dynamics. Certainly the rotational motion of the protein backbone is influenced by the motion of local water, but the EPR spectra will also depend on whether the spin labeled residue is in an α -helix, β -sheet, or an unstructured loop. Further, the spectrum is influenced by the rigidity of the bond linking the nitroxide radical to the protein backbone [57]. This

Figure 1.7. Rigid-limit EPR spectrum of the nitroxide radical, 4-oxo-TEMPO. The sample was prepared by 1 mM 4-oxo-TEMPO and 100 mM trehalose sugar in water and then drying the sample.



is not meant to imply that valuable information cannot be gained from EPR, but to emphasize that Overhauser DNP and EPR are measuring different interactions. DNP directly measures the ^1H NMR signal enhancement of water which depends on the dynamics of $^1\text{H}-e^-$ interactions, while EPR reports directly on the rotational motion and local environment of the spin probe.

II. The Overhauser effect with nitroxide radicals

A. Introduction

Nitroxide radicals have been used in liquid DNP studies for over 30 years and are commonly used in proton—electron double resonance imaging experiments [58-64]. Two of the advantages of these radicals are their stability and that they can be functionalized for different applications. For example, the amine (NH₂) group of 4-Amino Tempo shown in Fig 1.2 can be replaced by a hydroxyl or carboxyl group, as well as many other functional groups. This is very useful for attaching nitroxides to various molecules as local spin probes. Due to their usefulness in DNP experiments, several studies have been performed to quantify which radicals of this family have the largest coupling factor [65-67]. However, the results of these studies have varied greatly with values of ρ ranging from ~ 0.2 to larger than the theoretical maximum of 0.5. The differences are not consistent with the experiments being done at different magnetic fields. All three of these studies were done at low magnetic fields in the range of 6 to 15 mT. In this field range, ρ should be varying only slowly with increasing field, and dramatic differences should not be observed (see Fig 1.4). There is also no explanation for a measured $\rho > 0.5$. Common to these studies was the use of Eq. 2.1 for the saturation factor

$$s = \frac{1}{3} \frac{\alpha P}{1 + \alpha P} \quad (2.1).$$

To account for variances in applied power, the DNP enhancement is measured as a function of power, and the result extrapolated to infinite power. Thus we define

$$E_{\max} = E(P \rightarrow \infty) = 1 - \rho f s_{\max} \frac{|\gamma_S|}{\gamma_I} \quad (2.2)$$

where $s_{\max} = 1/3$ from Eq. 2.1. The leakage factor depends on the radical concentration through Eq. 1.9, but can be measured and accounted for with Eq. 1.8. Thus, no matter what concentration of radical is used, Eq. 2.2 can be used to find ρ . As we show in the Results and Discussion section, this method fails for nitroxide radicals. The three hyperfine lines of the nitroxide radical are not independent, but are coupled through collision induced electron spin exchange and through rapid relaxation of the ^{14}N nucleus of the nitroxide due to slow molecular tumbling [68]. A model for the saturation factor taking into account e^- spin exchange was originally proposed in 1977 by Bates and Drozdowski [69] in a rarely cited paper that I will discuss shortly. We show that this model works very well for nitroxides dissolved freely in solution, but does not explain our experimental results of spin labeled proteins and gels. These results require a model incorporating nitrogen nuclear spin relaxation into the saturation factor. It is important to note that in none of the studies investigating the coupling factor mentioned above (one as recent as 2006), did the authors use the work of Bates and Drozdowski in explaining their experimental data. Though nitroxide radicals were being widely used in Overhauser DNP experiments, and effort was being put into determining the ones that gave the best performance, a thorough investigation into these radicals and a quantitative understanding was lacking.

We also apply the FFHS model to the DNP and NMRD results as a check on the validity of this model. Our results show that the FFHS model fits the NMRD data

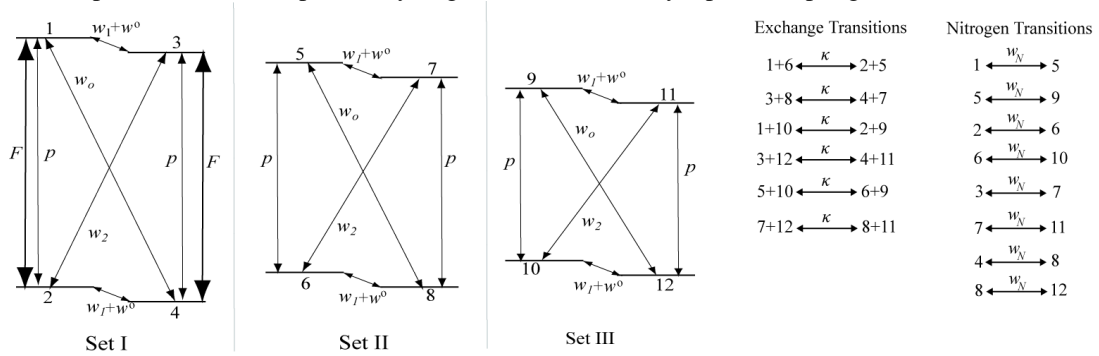
well. However, there is an unresolved discrepancy between the DNP and NMRD analysis. These experiments are important for showing that DNP can be used to gain information on hydration dynamics and for evaluating the limitations of the technique. Finally, we compare the DNP, NMRD, and molecular dynamics (MD) simulations results of two widely used types of nitroxide radicals; a pyrroline (5-membered ring) based and piperidine (6-membered ring) based ring structure. We show that the change in ring structure does not measurably change the coupling factor or relaxation behavior. This is relevant because a particular structure can be chosen for spin labels based on symmetry or ease of chemical modification, and the DNP results can still be compared. For example, 5-membered rings are usually used as spin labels for proteins and lipid tail groups, while 6-membered rings are often used on poly-electrolytes and lipid head groups. Additionally, our MD experiments discussed below show that the local diffusion coefficient of water is unaffected by the presence of the nitroxide radical. Hence, the measured DNP enhancements reflect the actual timescale of water diffusion and are not significantly perturbed by the spin label.

B. A new model describing the saturation factor

Bates and Drozdowski proposed that collision based electron spin exchange mixes the three hyperfine lines of a nitroxide radical. Since spin exchange requires a collision between two radicals, the effect will depend on concentration. Instead of assuming the simple four level model of Fig. 1.1, all three hyperfine states must be included. The new 12-level model is shown in figure 2.1 along with the possible exchange transitions with rate, $\kappa = \kappa' C$. Only exchange transitions involving

electrons in opposite spin states are shown as these result in a change of electron spin population for a particular set. However, the total electron spin population is conserved. In the figure, F represents e^- transitions induced by the applied microwave field and is only applied to one of the hyperfine states. Bates and Drozdowski made four assumptions: (1) the energy difference between the three hyperfine states is small so that the dipolar transition rates in each of the hyperfine sets can be considered equal, i.e. w_0 in set I equals w_0 in sets II and III. (2) The ^1H nuclear spin does not change during a spin exchange transition. (3) The rates p , F , and κ which involve only electron spins are much faster than the rates involving nuclear spin so small and second order terms can be ignored. (4) The ^{14}N nuclear spin is constant. I first summarize the results from Bates and Drozdowski and then discuss what happens when this fourth assumption is removed.

Figure 2.1. 12-level diagram describing the energy levels for a coupled e^- - ^1H system when using a nitroxide radical. The exchange transitions were first proposed in ref [69] while inclusion of ^{14}N nuclear spin transitions was part of my original work [18]. Only dipolar coupling is assumed.



Using the 12 level model, a set of 12 equations similar to Eq. 1.3 can be written, but we now include spin exchange transitions and explicitly include transitions induced by the microwave field, F . I leave the explicit details of how the equations were set up and solved to the original work [69], but the end result is

$$E = 1 - \rho f \frac{\omega_{\text{ESR}}}{\omega_{\text{NMR}}} \frac{1}{3} \left(\frac{a/p P}{1 + \frac{a(1+\kappa/p)}{p(1+3\kappa/p)} P} \right) \quad (2.3)$$

where we have assumed $F = aP$, and a is constant relating microwave power to F . There are several important aspects of Eq. 2.3 to notice. The first is that the power dependence is exactly the same as Eq. 1.7 and 2.1 as it should be since this is observed experimentally. Secondly, $|\gamma_S|/\gamma_I$ has been replaced by $\omega_{\text{ESR}}/\omega_{\text{NMR}}$. This implies that the maximum possible DNP enhancements depend on which hyperfine state is being irradiated. Bates and Drozdowski did observe this effect at magnetic fields of 5 to 9 mT, but at 0.35 T where our experiments were done, this change is negligible. Most importantly, however, is the inclusion of κ into the equation for E . Since $\kappa = \kappa' C$, there is now an extra concentration dependence of the DNP enhancements in addition to f . The result of this is seen more easily if we take the limit of infinite power; then

$$E_{\text{max}} = 1 - \rho f \frac{1}{3} \left(\frac{1 + 3C \kappa' / p}{1 + C \kappa' / p} \right) \frac{\omega_{\text{ESR}}}{\omega_{\text{NMR}}} \quad (2.4).$$

This equation is very similar to Eq. 2.2, but now s_{max} depends on the concentration of radical and T_{1e} . Additionally, in the limit of very high radical concentration

$$E_{\text{max}}(C \rightarrow \infty) = 1 - \rho \frac{\omega_{\text{ESR}}}{\omega_{\text{NMR}}} \quad (2.5).$$

Thus, if electron spin exchange is very fast compared to $1/T_{1e}$, irradiating one hyperfine line can effectively saturate the entire electron spin population, contrary to the previous assumption that only $1/3$ of the e^- spins can be fully saturated. However,

we recover this lower limit as $C \rightarrow 0$. While Bates and Drozdowski predicted this effect and used it to explain their larger than expected DNP enhancements, they did not attempt to quantify the effect by fitting for ρ or measuring T_{1e} and κ' .

A previous EPR study found that an isotope enriched ^{15}N -nitroxide radical dissolved in solution had a ^{15}N nuclear spin relaxation rate several orders of magnitude faster than the e^- spin relaxation rate for a range of tumbling times appropriate for spin labeled proteins [68]. Since ^{14}N is a quadrupolar nuclei even faster nuclear spin relaxation effects are expected, but no experimental studies were found in the literature. This work, along with our DNP experimental results on spin labeled molecules, motivated us to develop a model for the saturation factor that takes nitrogen nuclear spin relaxation into account. In developing the model, we follow the work of Bates and Drozdowski, but we allow the ^{14}N nuclear spin to change by ± 1 with rate w_N as shown in Fig. 2.1. Upon adding these new transitions, the DNP enhancement factor is given by [18]:

$$E = 1 - \rho f \frac{\omega_{\text{ESR}}}{\omega_{\text{NMR}}} \frac{1}{3} \left(1 - \frac{\frac{2w_N \omega_N}{p \omega_{\text{ESR}}}}{2 + \frac{w_N}{p} + \frac{6\kappa}{p}} \right) \times \left(\frac{\frac{aP}{p}}{1 + \frac{aP \left[4 + \left(\frac{w_N}{p} + \frac{2\kappa}{p} \right) \left(\frac{w_N}{p} + \frac{6\kappa}{p} \right) + 2 \left(\frac{3w_N}{p} + \frac{8\kappa}{p} \right) \right]}{\left[p \left(2 + \frac{w_N}{p} + \frac{6\kappa}{p} \right) \left(2 + \frac{3w_N}{p} + \frac{6\kappa}{p} \right) \right]}} \right) \quad (2.6)$$

where ω_N is the ^{14}N Larmor frequency. The first term in parenthesis in this equation is ~ 1 even if w_N/p is large due to the $\omega_N/\omega_{\text{ESR}}$ term, and will be ignored in the remaining discussion. In the second term, we see that the power dependence is the

same as Eq 2.3, agreeing with experimental results, but now the saturation factor depends on the e^- spin exchange rate, $1/T_{1e}$, and w_N . In the limit of infinite power, the maximum saturation factor becomes

$$s_{\max} = \frac{1}{3} \left[\frac{\left(2 + \frac{w_N}{p} + \frac{6\kappa}{p}\right) \left(2 + \frac{3w_N}{p} + \frac{6\kappa}{p}\right)}{4 + \left(\frac{w_N}{p} + \frac{2\kappa}{p}\right) \left(\frac{w_N}{p} + \frac{6\kappa}{p}\right) + 2 \left(\frac{3w_N}{p} + \frac{8\kappa}{p}\right)} \right] \quad (2.7).$$

If w_N is unimportant, then Eq. 2.7 reduces to the saturation factor of Eq. 2.4.

However, in the absence of any e^- spin exchange we still have

$$s_{\max}(\kappa = 0) = \frac{1}{3} \left[\frac{\left(2 + \frac{w_N}{p}\right) \left(2 + \frac{3w_N}{p}\right)}{4 + \frac{6w_N}{p} + \left(\frac{w_N}{p}\right)^2} \right] \quad (2.8).$$

Thus, if the nitroxide radical is tethered to a larger molecule to eliminate e^- spin exchange, s_{\max} can still approach 1 if $w_N \gg p$. A plot of Eq. 2.7 is shown in Fig 2.2.

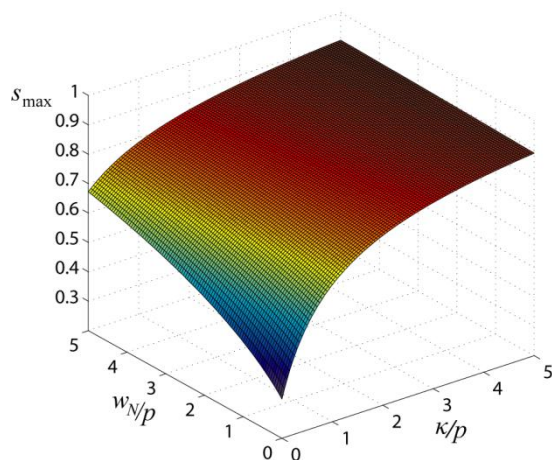
As either κ or w_N becomes large compared to p , s_{\max} approaches 1 due to efficient mixing of the hyperfine states. As they both go to 0, s_{\max} reduces to $1/3$ as expected.

Also, s_{\max} increases more rapidly with κ/p than with w_N/p . This is because an exchange interaction is a bimolecular process involving two nitroxide radicals, whereas nitrogen nuclear spin relaxation involves only one molecule.

Lastly, we also derived a saturation factor for a ^{15}N enriched nitroxide radical where there are only two hyperfine states. The maximum saturation factor is

$$s_{\max}(^{15}\text{N}) = \frac{1}{2} \left[\frac{1 + \frac{w_N}{p} + \frac{2\kappa}{p}}{1 + \frac{w_N}{2p} + \frac{\kappa}{p}} \right] \quad (2.9).$$

Figure 2.2. The maximum saturation factor using Eq. 2.7.



Of course if there is no mixing of hyperfine states, then a ^{15}N nitroxide radical will have a larger s_{max} of $\frac{1}{2}$ compared to $\frac{1}{3}$ for natural abundance ^{14}N . For fast nitrogen nuclear spin relaxation or e^- spin exchange, s_{max} for both ^{14}N and ^{15}N nitroxide radicals will converge to 1, though the ^{15}N nitroxide converges slightly faster. However, for spin labeled molecules where w_{N}/p can be on the order of 100-1000, using a ^{15}N labeled nitroxide has no advantage over the ^{14}N natural abundance nitroxide.

C. Results and Discussion

Quantifying the saturation factor

To test the model of Bates and Drozdoski, ^1H of water DNP experiments were performed with different concentrations of the nitroxide radical 4-oxo-TEMPO (Fig 2.3b) at 0.35 T (see Materials and Methods Section at the end of the chapter for more details). The NMR signal enhancements were measured at various microwave powers, and the results extrapolated to infinite power to find E_{max} . The leakage factor was also measured to verify Eq. 1.9 and the results are shown in Fig 2.4. If there is no

mixing of the hyperfine states, then knowing E_{\max} and f would be enough to determine ρ with Eq. 2.2 since all the concentration dependence is included in f . The calculated coupling factors using this method are shown in Fig 2.5. Clearly ρ is not constant as would be expected if $s_{\max} = 1/3$. Also, ρ was found to be greater than the theoretical maximum for every concentration above 2 mM. The experimental data for the leakage factor on the other hand, is accurately described by Eq. 1.9. Since f depends on the same dipolar relaxation rates as ρ , with the addition of w^0 , and Eq. 1.9 fits the data for f well, it is unlikely that there is an unaccounted for dependence of ρ on C . Thus we must re-examine the data using a model that incorporates mixing between the different hyperfine states.

The rotational correlation time of nitroxide radicals freely dissolved in solution (i.e. not being used as a spin label) is on the order of 20 ps and w_N/p is expected to be small [68, 71]. Thus, we can neglect w_N/p in this case and use Eq. 2.4 to analyze the DNP results. A plot of E_{\max} vs. C for 4-oxo-TEMPO is shown in Fig. 2.6 (solid circles; proxyl will be discussed below) and the data was fit to equation 2.4 with two fit parameters, ρ and κ'/p . The model fits the data well and gives $\rho = 0.22 \pm 0.01$ and $\kappa'/p = 1.0 \pm 0.3$. The electron spin exchange rate and relaxation time can be measured independently to serve as a check for the validity of this model, and the assumption that w_N/p can be ignored. Note that ρ , however, can actually be found from this method without measuring the leakage factor, spin exchange rate, or T_{1e} .

Figure 2.3. Chemical structures of two nitroxide radicals used in this chapter. a) 3-carbamoyl-2,2,5,5-tetramethyl-3-pyrrolin-1-oxyl (proxyl), and b) 4-oxo-2,2,6,6-tetramethyl-1-piperidinyloxy (4-oxo-TEMPO). Structures used in MD simulations of c) proxyl and d) 4-oxo-TEMPO created with PyMOL [70] and an example of the orientation of hydrogen bounded water molecules as discussed in the text.

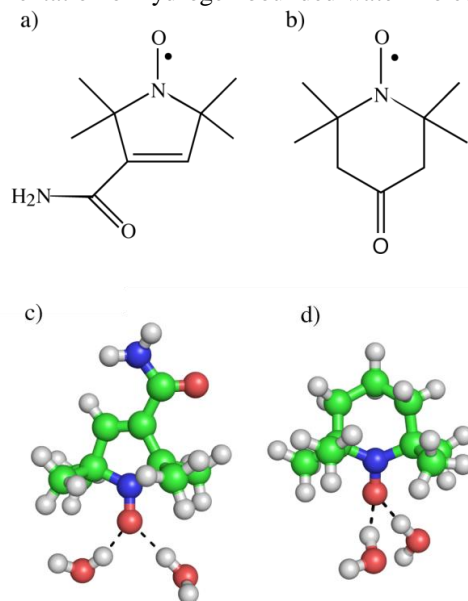


Figure 2.4. The leakage factor measured with Eq. 1.8 for different concentrations of 4-oxo-TEMPO. The solid line is the fit of the data to Eq. 1.9 and gives $k = 0.217 \text{ mM}^{-1} \text{ s}^{-1}$.

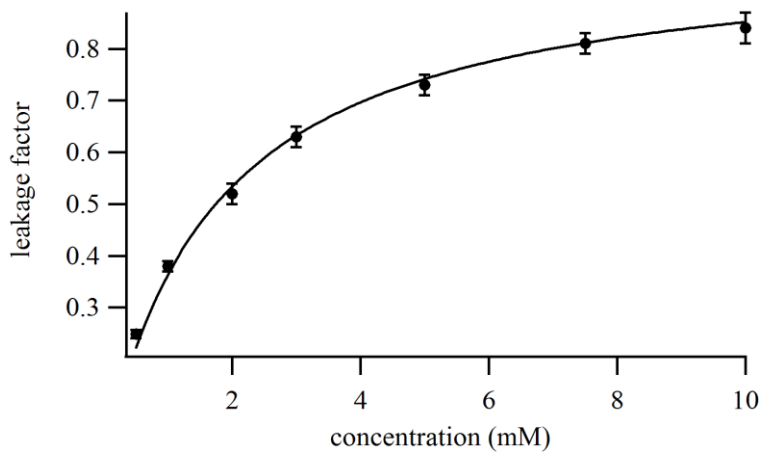


Figure 2.5. Calculated coupling factors for 4-oxo-TEMPO at various concentrations assuming $s_{\max} = 1/3$. ρ is clearly not constant under this assumption, and even exceed the theoretical maximum of 0.5.

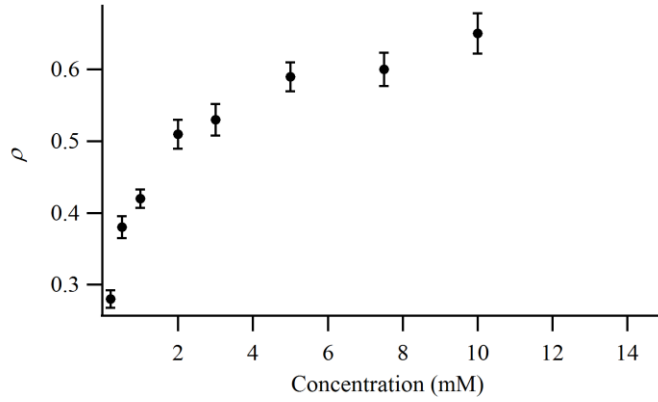
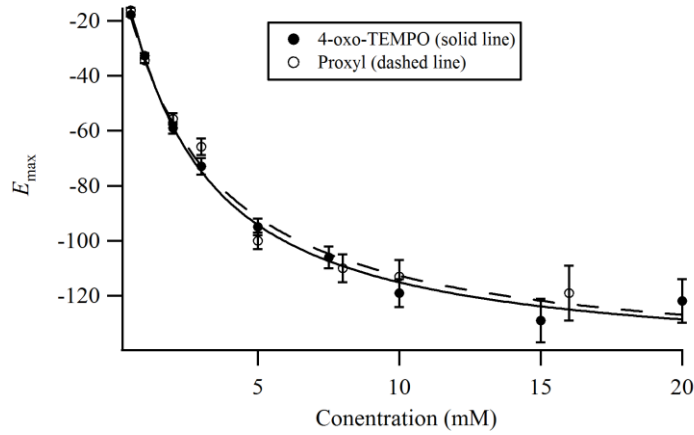


Figure 2.5. A plot of the maximum enhancement for different concentrations of 4-oxo-TEMPO and proxyl discussed in the chapter. The error bars represent estimated standard deviations from the fit parameters.

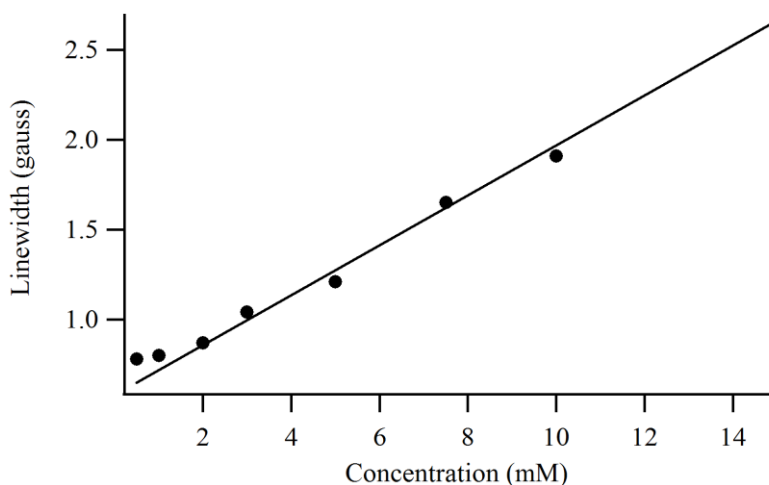


The electron spin exchange rate was determined by measuring the EPR linewidth for different concentrations of dissolved radical. As the electron spin exchange rate increases, the absorption linewidth, Γ , of the EPR spectra also increases according to the equation [72]

$$\Gamma = \Gamma_0 + \frac{2\kappa' C}{3\gamma_S} \quad (2.10)$$

where Γ_0 is the linewidth in the limit of no spin exchange, and the factor of $\frac{2}{3}$ is needed because $\frac{1}{3}$ of all collisions will involve nitroxides that have the same ^{14}N spin state. The results of this experiment are plotted in Fig 2.6. Notice that at low C the linewidth does not increase significantly as C is increased. This is because Eq. 2.10 only accounts for broadenings due to spin exchange. At low C the linewidth is dominated by unresolved hyperfine couplings that do not depend on C , and the effect of spin exchange is not easily observed until ~ 2 mM in this case. From the slope of the fit line in Fig. 2.6, $\kappa' = (3.7 \pm 0.1) \times 10^6 \text{ mM}^{-1} \text{ s}^{-1}$. The electron spin-lattice relaxation rate was measured with pulsed EPR to be $\sim 290 \pm 30$ ns. Thus, from experimental measurements $\kappa'/p = 1.1 \pm 0.1$. This is in excellent agreement with the fit value from the DNP data and is the first quantification of the predicted saturation factor of Bates and Drozdoski [19].

Figure 2.6. EPR absorption linewidth of 4-oxo-TEMPO dissolved in water at different concentrations.



From Fig 2.5, we can also see that both 4-oxo-TEMPO and proxyl have nearly the same E_{max} values at each concentration, and both have $\rho = 0.22$. This is encouraging

as it implies that we can compare DNP results using either radical. This will be further confirmed by the NMRD and MD simulations discussed below. We can extract the timescale of translational motion from ρ using the FFHS model with Eqns 1.14 and 1.16. Using $\rho = 0.22$, and solving for the translational correlation time gives $\tau_t = 76$ ps. This result will be discussed with the value for τ_t found from fitting the NMRD data shortly.

Including only e^- spin exchange into the saturation factor works well for nitroxide radicals freely dissolved in solution, but when the radical is attached to a protein we expect that collisions between nitroxide radicals will be eliminated. Hence, if nitrogen nuclear spin relaxation is unimportant, then s_{\max} should be $\frac{1}{3}$. Additionally, the diffusion of water is expected to be slower near the surface of biomolecules, reducing ρ from its bulk value. Thus, at any concentration, the value of ρs_{\max} for a spin labeled molecule should be smaller than that for the free label. However, this was not observed when attaching a nitroxide radical to the human protein isoform tau187 (details of this sample can be found in reference [73]). Table 2.1 compares the DNP results for equal concentrations of 4-oxo-TEMPO free in solution and spin labeled tau. The leakage factors were measured, so that the values of ρs_{\max} can be compared. For 200 μM tau, ρs_{\max} is greater than for 200 μM 4-oxo-TEMPO. This result can only be explained if the saturation factor is larger than $\frac{1}{3}$. The increase in the saturation factor cannot be due to e^- spin exchange since the values of ρs_{\max} for 200 μM and 1 mM spin labeled tau are equal, and thus ρs_{\max} is independent of concentration. Thus, nitrogen nuclear spin relaxation must be mixing the electron

hyperfine state. Even if we were to assume the coupling factors for spin labeled tau and 4-oxo-TEMPO in solution are equal, then s_{\max} for tau would be 0.64, so greater than $\frac{1}{3}$. This places a lower limit on s_{\max} because ρ is likely smaller for spin labeled tau due to slower diffusion of water near its surface than in bulk. In fact, using the work of Robinson and coworkers, w_N/p is likely to be so large that s_{\max} is very close to 1 [23, 68]. This is an exciting result that had never before been predicted until our 2007 publication [18].

Table 2.1. Comparison of ρs_{\max} for spin labeled tau vs. freely dissolve 4-oxo-TEMPO, and for a ^{14}N natural abundance and ^{15}N isotope enriched nitroxide radical attached to a sepharose gel. The ^{14}N vs. ^{15}N comparison on sepharose was reported in reference [74].

Sample	E_{\max}	ρs_{\max}
200 μM tau	-8	0.14
1 mM tau	-27.5	0.13
200 μM TEMPO	-5.5	0.01
1 mM TEMPO	-32.6	0.15
^{14}N labeled gel	-42	0.07
^{15}N labeled gel	-46	0.08

As a final check for the validity of our new model for the saturation factor, McCarney and Han spin labeled sepharose beads that we had used previously to enhance water as a natural contrast agent to image the flow of water in a water saturated system [74, 75]. One sample was made with a nitroxide radical that was enriched with ^{15}N (spin $\frac{1}{2}$) instead of the naturally abundant ^{14}N . Since the nitroxides are tethered to the sepharose gel, e^- spin exchange should be negligible, but their rotational mobility is slowed, resulting in a large w_N/p value. As predicted by our model for s_{\max} , the enhancement values for the two spin labeled gels as well as the ρs_{\max} values are nearly identical as seen in Table 1. If the previous assumption that

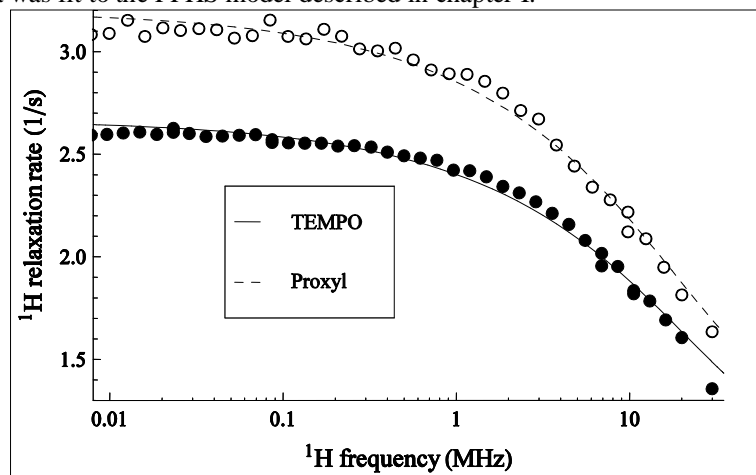
only one of the hyperfine states was affected by the microwave irradiation, the ^{15}N nitroxide radical should give much larger enhancements, but this is not observed. Again, this result can only be explained by efficient mixing of the electron hyperfine states.

Evaluating the Force Free, Hard Sphere Model

In chapter I, the theory of the FFHS model was discussed. Figure 2.7 shows the ^1H relaxation rate of water with 5 mM of 4-oxo-TEMPO (solid circles) and 5 mM proxyl (open circles) as a function of the ^1H Larmor frequency. The data was fit to FFHS model using Eq. 1.14 and Eq. 1.15. As seen in Fig 2.7, the FFHS model approximates the experimental data well. The parameters for the two radicals are in very good agreement with each other; for 4-oxo-TEMPO $\tau_t = 24$ ps and $d = 2.43$ Å, while for proxyl $\tau_t = 27$ ps and $d = 2.36$ Å. We consider these differences insignificant even though the data suggests that proxyl is more efficient at relaxing the ^1H of water. This is most likely due to an error in the measured concentrations as a deviation of $< 10\%$ would account for this difference. These measurements are also in very good agreement with previously published NMRD results of nitroxide radicals [76, 77].

While the FFHS model approximates the relaxation data well, it is apparent that for both nitroxide samples the ^1H relaxation rate does not initially decrease as rapidly as predicted. Further, at higher frequencies the data falls off more rapidly than predicted by the fit (note that standard NMRD spectrometers do go to higher

Figure 2.7. NMRD data for 4-oxo-TEMPO (solid circles) and proxyl (open circles) dissolved in water. The data was fit to the FFHS model described in chapter I.



frequencies than shown here, unfortunately missing the high frequency behavior shown in Fig. 1.5). This behavior suggests the possibility of a rotational component contributing to the relaxation rate (see Fig 1.5). This would be significant if water was hydrogen bound to the nitroxide radical with a lifetime, τ_m , that is on the same order of, or greater than the rotational correlation time of the complex, τ_r (see Eq. 1.17). The results were fit to a combined translational/rotational model, and the quality of the fit improved. However, the rotational component was only 9%, the fit values for d and τ_t changed by less than 5%, yet combined model requires three new fit parameters: b , τ_r , and τ_m . Given that the FFHS model is already an approximation, adding an additional three fit parameters is not justified given the small improvement. Also, our MD results discussed below do not show significant hydrogen bonding. It is unlikely that the deviation of the data from the fit occurs from a small rotational component, but rather reflects the shortcomings of the FFHS approximation.

The coupling factor found from our DNP measurements corresponds to $\tau_t = 76$ ps using the FFHS model, while the fit of the NMRD data gave $\tau_t \approx 25$ ps. Given the approximation of treating the spins as centered on hard spheres, a factor of three difference between the two experimental techniques is perhaps not surprising. There are several points worth emphasizing about this discrepancy. More realistic models describing the system have been used, such as moving the spins off center or allowing for some hydrogen bonding, only marginally improved the fit to the NMRD data but add several fit components and do not change the estimate for the timescale of dipolar interaction significantly [19, 77]. Steric factors and order parameters have been added to account for the molecules not being spherical or “hard”, but these parameters are usually treated as a constant term in front of the spectral density function [47, 78]. Thus, their inclusion may change the overall relaxation rate, but not the estimate of the timescale modulating the dipolar coupling. Also, all constant terms in front of the spectral density functions fall out of the equation for ρ (see Eq. 1.16) and so would leave τ_t calculated from DNP experiments unchanged. Thus, it seems likely that only by changing the form of the spectral density function from that given by the FFHS model can the two techniques be brought together. This was attempted in a recent study using MD simulations to calculate the coupling factor [79]. Not surprisingly, this work found that the nitroxide-water system cannot be defined by a single correlation time, and thus a calculation of τ_t from either technique would not be justified. However, at timescales of ~ 100 ps, the simulations were in relative agreement with the FFHS model and this agreement was forced upon the simulations

at longer timescales. This implies that Overhauser DNP can still be used to find the dynamics of water interacting with biological surfaces. DNP studies in the Han group on lipid vesicles have found values of τ_t that are within a factor of two of those found with NMRD on very similar systems (this time with DNP giving the smaller τ_t), suggesting that there is indeed better agreement as τ_t increases [22, 43]. It must be stressed that the MD simulations in reference [79] are unique for the particular case of a nitroxide dissolved in solution and offer no general method for studying local water interactions. The FFHS model remains the most widely used model describing dipolar relaxation due to translational diffusion [37, 42, 43, 77, 80, 81]. So even though the FFHS model is known to be an approximation, given the lack of experimental techniques, Overhauser DNP is still a promising method to study local hydration dynamics whose applicability can be widened with improved dynamic models.

It has been proposed that NMRD should be used to calculate ρ instead of DNP due to complications with the saturation factor [76]. Our work on the saturation factor above shows that s can be quantified, and DNP should be used for calculating ρ . Most importantly, determining ρ with DNP enhancements does *not* require a dynamic model to be invoked, unlike NMRD. Due to the discrepancy already discussed, NMRD is unlikely to report an accurate coupling factor. Also, in situations where the FFHS model is known to fail, DNP can still be used to gain qualitative information about local dynamics. Further, NMRD usually requires milli-molar concentrations, so it is not a viable technique for many proteins. Lastly, NMRD experiments are time consuming, especially at low concentrations, and so cannot be used to monitor

changes in dynamics with time resolution as has been done with our DNP method [25].

Molecular Dynamics Simulations

Our DNP and NMRD experimental results show that 4-oxo-TEMPO and proxyl are very similar, and suggest that results from experiments using either 6-membered or 5-membered ring nitroxide structures can be compared. However, a few questions remain: does water near the radical have the same translational dynamics as the bulk, is there significant hydrogen bonding of water to the nitroxide, and is the distance of closest approach similar between the two nitroxide structures? To answer these questions, MD simulations were performed on the two radicals, and the results are summarized in Table 2.2. Our findings for proxyl are in excellent agreement with previous MD simulations carried out by Pavone and colleagues who used MD to study the EPR properties of proxyl [82, 83]. There are small differences in the results depending on the water model used (a 3-site SPC-E model and a 4-site TIP4P model; see Materials and Methods at the end of this chapter), but the results for 4-oxo-TEMPO and proxyl are within their estimated error, agreeing with our experimental data. On average, two ^1H nuclei are hydrogen bound to the nitroxide (from two different water molecules, as shown in Fig. 2.3) but the lifetime is only on the order of 4-6 ps. The rotational tumbling time of the molecule is ~ 26 ps [68, 71], so we are justified in ignoring bound water when modeling the relaxation behavior as mentioned above. The distance between the ^1H of water and the center of mass (COM) of the N-O bond (where the electron probability is highest) is the same for

each radical. This supports our assumption that the offset in the relaxation data between proxyl and 4-oxo-TEMPO seen in Fig. 2.7 is likely due to errors in the concentration measurements. Most important is the result that the diffusion of water near the nitroxide radical is the same as the simulated diffusion of bulk water reported in the literature [84]. This means that the presence of the nitroxide does not significantly perturb the local water dynamics, and so the DNP enhancements reflect the actual local dynamics of water. If this were not the case, then DNP could not be used to estimate local hydration dynamics.

Table 2.2. Comparison of the MD result for 4-oxo-TEMPO and proxyl using two different water models. The $\text{NO}_{\text{com}}\text{-H}_{\text{solvent}}$ distance reported is the peak of the radial distribution function. The coordination number (Coord.) is the average number of ^1H nuclei that are hydrogen bound to the nitroxide. $D_1(\text{bulk})$ is taken from reference [84].

		$\text{NO}_{\text{com}}\text{-H}_{\text{solvent}}$ (Å)	Coord.	H-bond τ (ps)	$D_1(\text{radical})(\text{m}^2\text{s}^{-1})$	$D_1(\text{bulk})(\text{m}^2\text{s}^{-1})$
Proxyl	tip4p	2.7	2.0	4.6	4.1×10^{-9}	4.0×10^{-9}
	spc/E	2.8	2.0	5.5	3.0×10^{-9}	2.9×10^{-9}
TEMPO	tip4p	2.7	1.7	4.3	4.3×10^{-9}	4.0×10^{-9}
	spc/E	2.7	1.9	5.0	3.1×10^{-9}	2.9×10^{-9}

D. Conclusion

The results of this chapter lay the foundation for using DNP as a technique to study water-surface interactions. The coupling factor contains information on the dynamics between the two spins. This cannot be found, however, if the saturation factor is unknown. While the saturation factor with nitroxide radicals is complicated due to mixing of the electron spin hyperfine states, we have shown in this chapter that the saturation factor can be accurately determined. Additionally, we show that the FFHS model approximates the relaxation data well and can be used to give an

estimate of the timescale modulation the $^1\text{H}-e^-$ dipolar interaction. There remains an unresolved discrepancy between the results obtained from DNP and NMRD. Given the lack of experimental techniques available to study hydration water, we still expect DNP to be a valuable tool in these studies. Rough estimates of the timescale of the dipolar interaction can be obtained for systems such as spin labeled lipids and protein surfaces where the FFHS model describes the data well. However, determining the coupling factor from DNP does not rely on a dynamic model and can therefore give qualitative information on hydration dynamics with site specificity even if the dynamic model is not known. Lastly, our MD simulations show that the nitroxide radical does not disturb the diffusion of local water molecules. This implies our DNP enhancements will accurately reflect changes in local dynamics and are not affected by the nitroxide spin probe. Further, the MD simulations show that hydrogen bonding of water to the nitroxide probe is not significant and we are justified ignoring its contribution when modeling DNP signal enhancements.

E. Materials and Methods

3-carbamoyl-2,2,5,5-tetramethyl-3-pyrrolin-1-oxyl (proxyl), and 4-oxo-2,2,6,6-tetramethyl-1-piperidinyloxy (4-oxo-TEMPO) were purchased from Sigma-Aldrich. 4-oxo-TEMPO was initially dissolved at a high concentration in DMSO and then diluted into water, the final solution containing at most 5% DMSO by volume. Proxyl was dissolved directly into water. For DNP and EPR measurements, $\sim 5 \mu\text{L}$ of sample was loaded into a 0.7 mm id capillary and sealed in beeswax. The sample was loaded into a homebuilt NMR probe and placed inside a commercial Bruker TE₁₀₂ X-band

cavity. NMR measurements were made with a Bruker Avance 300 NMR spectrometer at a magnetic field of ~ 0.35 T. The center electron resonance was irradiated with a high power, home built microwave amplifier described in the next chapter. Cooling air was flowed over the sample to minimize heating. Maximum enhancements were determined by fitting the enhancement vs. power data to

$$E = I_0 + \frac{AP}{1 + BP} \quad (2.11)$$

where I_0 , A , and B are fit parameters containing all the constants in Eq. 2.6. $E_{\max} = I_0 - A/B$. Igor Pro data analysis software was used to estimate errors in the fits.

For EPR linewidth analysis, the samples were prepared in the same way as for DNP experiments, only the sample was not loaded into an NMR probe to avoid possible linewidth distortions. ^1H T_1 inversion-recovery experiments were performed at 0.35 T using a commercial Bruker BBFO 5 mm probe with ~ 200 μL of sample to determine the leakage factors for the different samples. NMRD measurements were performed at the Technical University of Ilmenau on a Stelar FFC 2000-1T field cycling relaxometer and the data was fit in Mathematica. The electron spin relaxation time, T_{1e} , was measured on an ELEXYS pulsed X-band EPR spectrometer at Bruker Biospin with inversion recovery and a π pulse of 4 ns. The estimated error of 10% for T_{1e} arises from incomplete inversion off all three of the nitroxide hyperfine lines.

MD simulations were performed with the GROMACS.x software package [84, 85]. The all-atom OPLS force field [86, 87] was used to describe the solute and tip4p [88] and spc/e [89], were used to model the solvent. The temperature and pressure were maintained near 300K and 1 bar by weak coupling to an external bath [90] with

a coupling constant of 0.1 ps for temperature and 1.0 ps for pressure. The LINCS [91] algorithm was used to constrain bond lengths within the solute. The SETTLE [92] algorithm was used to constrain bond lengths and the bond angle in water. A 2 fs integration times step was used. A smooth particle mesh Ewald method [93] was used to evaluate Coulomb interactions with a real-space cut-off of 0.9 nm, grid spacing of 0.12, and quadratic interpolation. van der Waals interactions were evaluated using a cut-off method, with a cut-off distance of 0.9 nm. Neighbors lists were updated every five steps. The structure of each solute was initially generated with Molden [94] and then optimized at the level of HF/6-13G* using Gaussian03 [95]. Partial charges on the atoms were obtained by fitting the gas phase electrostatic potential calculated at the HF/6-13G* level using RESP [96]. The solute molecule was initially solvated in a periodic 21.45 nm³ box. Initial velocities were assigned from a Maxwellian distribution at 300K. Cartesian coordinates were stored every 100 fs. For data acquisition in each solvent model, an initial 2 ns trajectory was generated. Then ten snapshots from this trajectory were chosen to initiate 10 independent 2 ns trajectories, of which the first 200 ps were disregarded for analysis. Values are reported after averaging over the 10 independent trajectories.

III. Portable DNP and Improved Hardware

A. Introduction

In this chapter we report two advances in improving Overhauser DNP signal enhancements. Using a custom built, high power microwave amplifier we were able to increase our measured ^1H of water NMR signal enhancements, E , by nearly a factor of three. This microwave amplifier has become the standard equipment used in our lab for DNP experiments, and two similar systems have since been built in our lab. As both the microwave source and amplifiers are compact, we also developed a fully portable DNP system at 0.35 T. As portable NMR systems operate at low magnetic fields due to the limited field strength of small permanent magnets, so the sensitivity gain from DNP may be advantageous [97]. Also, a portable system has proved useful in applying DNP to imaging experiments developed in our lab [75]. Instead of dedicating an MRI instrument for use with DNP imaging experiments, the microwave equipment can be taken to a MRI facility for imaging experiments [98].

The main challenge in designing a portable DNP setup at 0.35 T is efficiently irradiating the electron spin resonant transition. Resonant cavities are preferred, but have a narrow bandwidth available for exciting the electron transition. In a fixed field permanent magnet, a resonant cavity will not have much flexibility since the field cannot be varied to match the resonance of the cavity. To overcome this difficulty, we employed two different techniques: (1) A commercial TE_{102} cavity was modified with a movable wall, providing a tuning range of nearly 400 MHz for use in a fixed field permanent magnet. (2) A variable field Halbach permanent magnet was used to match

the magnetic field to the resonance of a commercial TE₁₀₂ cavity. This last method resulted in larger signal enhancements, but at the time these experiments were performed a variable field Halbach magnet was not commercially available [20]. We characterize the DNP efficiency of our custom source under ideal conditions using a commercial resonator and sweepable electromagnet and compare these results to those obtained in our two portable setups. The field homogeneity of the variable Halbach magnet is characterized in the Materials and methods section.

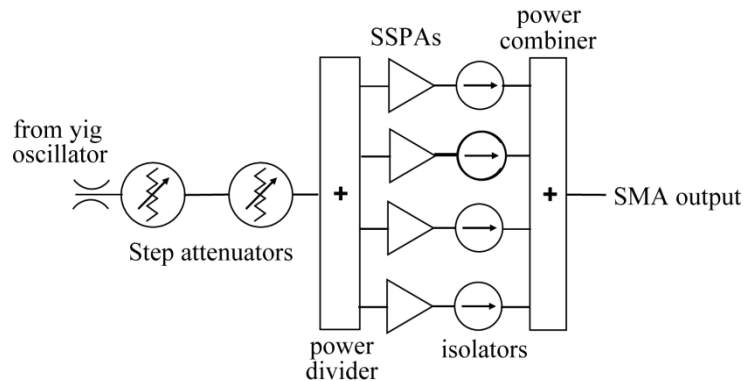
B. Results and Discussion

Characterization of high power microwave amplifier

A circuit diagram of our microwave amplifier is shown in Fig 3.1. A yttrium-iron-garnet (YIG) oscillator outputs ~ 27.5 mW with a tunable frequency range of 8-10 GHz. After amplification by four solid state power amplifiers (SSPAs) in parallel, the output power is ~ 23 W. Two step attenuators allow the power to be varied from ~ 23 W to 370 mW. An EIP 548A frequency counter equipped with a power meter was used to measure the forward power after 30 dB of attenuation. However, this measurement is the power exiting the amplifier and not the actual power being delivered to the sample. The source was characterized by measuring the ¹H of water NMR signal enhancements, with different nitroxide radical solutions (see Table 3.1). To estimate the power delivered the sample, DNP enhancements with our custom microwave amplifier were compared to those measured using a commercial Bruker EMX spectrometer that displays the power under leveled and matched conditions. For example, the measured ¹H of water NMR signal enhancement for a sample of 4-oxo-

TEMPO dissolved in water with 126.9 mW of power from the commercial system was -23.5. The same enhancement was measured with 460 mW of forward power leaving the homebuilt amplifier. Thus only $\sim 1/4$ of the input power was found to actually reach the sample. This is because the TE_{102} cavity was not matched while using the high power source due to damage caused to the iris of the cavity at powers nearing 20 W. Using a directional coupler, both the forward power leaving the amplifier and the reflected power returning from the sample were measured. The ratio of forward power to reflected power was found to be constant, so we conclude that an increase of 1 dB in forward power corresponds to a 1 dB increase in power reaching the sample.

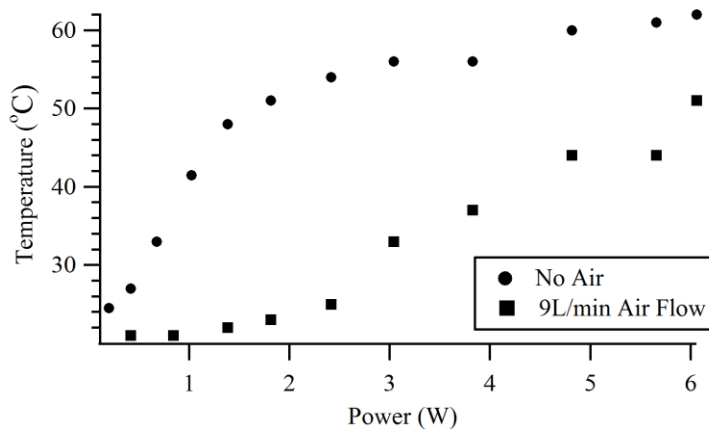
Figure 3.1. Circuit diagram of the custom X-band amplifier. Output of the YIG synthesizer is sent through two step attenuators (0-9 dB each) to vary the power. The power is divided and passed through 4 amplifiers (SSPAs) in parallel. Isolators protect the SSPAs from reflected power. The power is combined and sent to an SMA output to be coupled to the load.



Dielectric absorption is known to be problematic at 10 GHz, and with watts of power being delivered to the sample significant heating is expected. To measure the extent of heating, a 1mm inner diameter pasteur pipette was loaded with water and placed in the resonator. A thermocouple was placed inside the pasteur pipette just

outside of the microwave region. The temperature was recorded as the microwave power was increased. As seen in Fig. 3.2, there is an immediate increase in sample temperature and severe heating at less than 1 W of power to the sample. However, by flowing air over the sample at 9 L/min this heating was greatly reduced with a small increase in sample temperature at 2.4 W. In a typical DNP experiment, our sample is loaded into a 0.6 or 0.7 mm inner diameter capillary. We therefore expect these measurements to be an upper limit on heating as a narrower sample should have a smaller E field component in the sample region resulting in less dielectric absorption and more efficient heat dissipation from the cooling air.

Figure 3.2. Sample temperature measured as a function of microwave power reaching the sample with (squares) and without (circles) cooling air. Cooling air greatly reduces heating such that at 2.4 W of power the sample temperature was only 25 °C compared to 54 °C without the use of cooling air.



Our initial DNP experiments were performed using a commercial Bruker EMX spectrometer (for EPR experiments) as our microwave source. The maximum output power of this source was only 200 mW, and it was clear from our DNP signal enhancements versus power measurements that our measured enhancements were far from what was theoretically possible. For example, in my initial work on the

saturation factor, the largest measured signal enhancement was only -55 for an 8 mM sample of ^{15}N 4-oxo-Tempo dissolved in water [18]. However, at high concentrations of nitroxide radicals where $E_{\text{max}} \approx 1 - \rho|\gamma_S|/\gamma_I$ (remember that $E_{\text{max}} = E(P \rightarrow \infty)$, Eq. 2.2), enhancements approaching -145 should be possible (using $\rho = 0.22$ found last chapter) for ^1H of water with a nitroxide radical. This was the primary motivation for developing a high power amplifier. Table 3.1 summarizes our results with the nitroxide radicals 4-oxo-TEMPO and 4-amino-TEMPO as well as their ^{15}N isotope enriched counterparts. Most importantly, with this new amplifier we measured signal enhancements greater than 100. At the time these results were submitted, this was the largest reported ^1H DNP enhancements of water at 0.35 T [20].

Table 3.1. Comparison of measured ^1H NMR signal enhancements for 6 different solutions using our custom microwave amplifier and commercial TE_{102} resonator. The EPR derivative linewidth, ΔB_{pp} , is a good indicator of how easy a particular sample is to saturate. The listed measured enhancements were taken with 2.4 W of power and cooling air except*; this sample was measured at maximum power. Measured E with the commercial was only -46 for 15 mM ^{15}N 4-oxo-TEMPO.

Radical	Conc (mM)	ESR ΔB_{pp} (gauss)	Meas. E	E_{max}	cooling air
^{15}N 4-oxo*	15	1.15	-131 ± 6	----	no
^{15}N 4-oxo	15	1.15	-112 ± 4	-136 ± 8	yes
^{14}N 4-oxo	15	1.57	-98 ± 3	-131 ± 8	yes
^{15}N 4-Amino	15	1.6	-94 ± 4	-127 ± 8	yes
^{14}N 4-Amino	15	2.33	-88 ± 3	-126 ± 6	yes
^{15}N 4-Amino	100	7.35	-72 ± 3	-121 ± 9	yes
^{14}N 4-Amino	100	7.72	-71 ± 3	-124 ± 10	yes

The derivative EPR linewidths are reported in the table because they provide a good measure of how easy a particular sample is to saturate. Previously we only measured an enhancement of -46 for 15 mM ^{15}N 4-oxo-TEMPO with our 200 mW source [18]. For the same linewidth, we now measured an enhancement of -112 under conditions where we expect sample heating to be limited. This is almost a threefold

improvement in our DNP efficiency and the measured enhancement is nearing the predicted maximum for this sample. As the linewidth of the sample increases, our measured DNP enhancements decreased, but even for 100 mM radical concentrations large signal enhancements were measured. Also, the E_{\max} values for all samples are nearly identical. This again provides more evidence that e^- spin exchange must be effectively mixing the electron hyperfine states as the ^{15}N nitroxide sample would be expected to have $\sim 50\%$ larger signal enhancements in the absence of mixing of the hyperfine states due to having only two hyperfine lines instead of three.

It is interesting that our largest measured enhancement factor of -131 compared to room temperature thermal polarization was measured under conditions where significant sample heating is expected (6 W of power, and no cooling air). This effect can partially be explained by examining the expected changes of thermal polarization and ρ with increasing temperature. An increase in temperature from 20 to 60° C (Fig. 3.2) corresponds to a loss of thermal polarization of about 17%. The increase in temperature also causes a decrease in the viscosity of water by approximately 50% [99]. We can use this change in solvent viscosity to estimate the change in ρ using the FFHS model; the result giving $\rho \sim 0.3$. This increase in ρ more than offsets the loss in thermal polarization, and thus results in a larger measured signal enhancement. It should be pointed out that this is not a general result and is specific to this case. Since both f and s_{\max} are both close to 1 and changing slowly at 15 mM nitroxide concentration, I have ignored any changes in these parameters. However, with heating f is expected to change (Eq. 1.15) and s_{\max} will increase due to more rapid e^- spin

exchange caused by more frequent collisions (Eq. 2.4 and Fig. 2.2). Additionally, the increased e^- spin exchange rate causes a broadening of the EPR line (Eq. 2.10) which can result in lower measured enhancements as discussed above. Therefore, the changes in ρ , f , s , and thermal polarization will have competing effects and the change in measured DNP enhancement will be highly sample and frequency dependent.

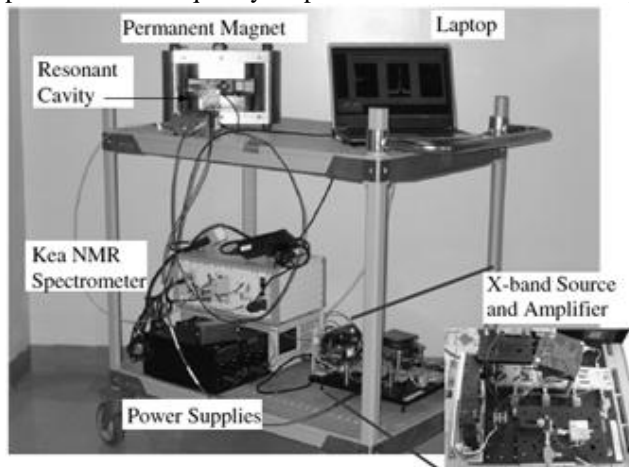
Portable DNP

Our custom microwave source not only outputs high power for efficient DNP enhancements, but is also very compact. The YIG synthesizer, 10 MHz reference, SSPAs, power supplies, and resonator all easily fit on a table top (Fig 3.3). The large electromagnet was replaced by two different types of permanent magnets. One is a fixed field, commercially available, permanent magnet with a 35 mm gap with B_0 normal to the pole surface (Fig 3.3). The second is a field adjustable Halbach magnet [100-102] with a 100 mm cylindrical bore and B_0 perpendicular to the cylindrical axis. This magnet was not commercially available at the time of development. Another possible solution would be to add resistive coils to the fixed field permanent magnet. This has the disadvantage of the coils causing a field drift by heating the permanent magnet.

Our commercial TE_{102} resonant cavity was modified to make it tunable for use in a fixed field permanent magnet. This was done by making the length of the long axis of the cavity variable with an adjustable wall. A spring was placed between a movable wall and a fixed plate attached to the cavity. A screw was used to vary the

position of the movable wall, thus varying the length of the resonator and its frequency. The DNP efficiency of the modified cavity was tested by placing it in an electromagnet so the field could be accurately adjusted to match the resonance

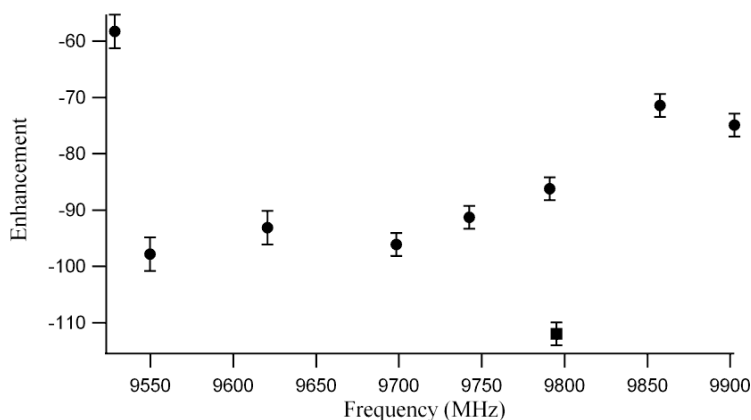
Figure 3.3. Complete portable setup. The power supplies, microwave source, and *Kea* NMR spectrometer are set on the bottom of the cart and the fixed field permanent magnet with the resonant cavity on top. A laptop controls the frequency output of the YIG and the NMR spectrometer.



condition. The resonance frequency of the cavity was monitored with a Bruker EMX spectrometer and EIP frequency counter. The YIG synthesizer was then set to the resonant frequency, coupled to the cavity, and the DNP enhancements were measured. Significant ^1H DNP enhancements of water were measured with ^{15}N 4-oxo-TEMPO for a frequency range of 9528.5—9902.5 MHz, corresponding to a change in magnetic field of 3389—3352 Gauss as seen in Fig 3.4. At 9528.5 MHz, there is a sudden drop in the signal enhancement that is likely caused by poor alignment of the adjustable wall as the mechanical limit of the wall position was reached. The largest recorded enhancement of -98 was smaller than the measured enhancement of -112 using an unmodified commercial cavity. We attribute this

decrease to a lower loaded Q of ~ 1400 in our modified cavity while the unmodified commercial resonator had a loaded Q of ~ 2200 .

Figure 3.4. Enhancement vs. frequency for our adjustable cavity with a sample of 4-oxo-TEMPO in solution (circles). An electromagnet was used so the field can be precisely adjusted to match the electron spin resonance condition. The square point represents the enhancement in the unmodified commercial cavity.



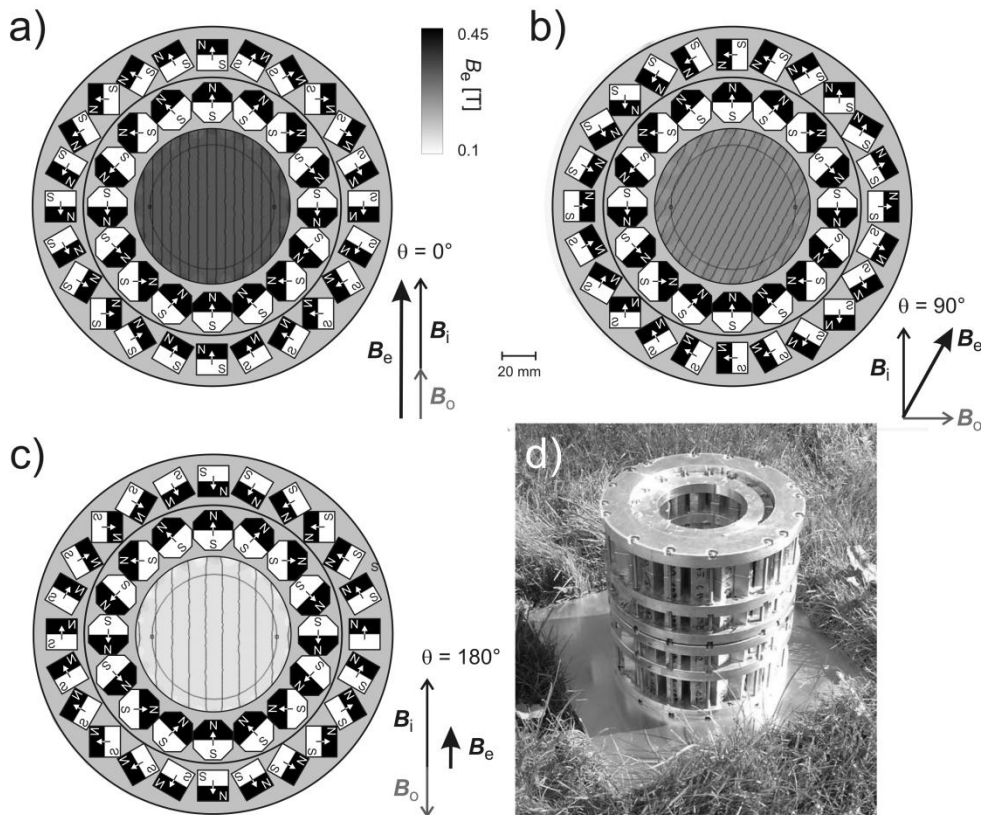
The tunable cavity was placed inside our portable, fixed field permanent magnet to evaluate its performance on the same 15 mM, ^{15}N 4-oxo-TEMPO solution. The ^1H NMR frequency was first measured and used to calculate the electron spin frequency. After setting the YIG to this frequency, the ^1H DNP enhancements were then measured while adjusting the position of the movable wall to bring the cavity into resonance. The largest measured enhancement was -65 and is about 25% less than -86 measured signal enhancement in the electromagnet at the same frequency. We believe the decrease in signal enhancement is primarily due to the difficulty in precisely adjusting the resonance of the cavity to match the electron Larmor frequency. An improved design, such as allowing for more fine adjustments of the moveable wall should increase the DNP efficiency of the portable setup. However, an enhancement

of -65 is still quite significant and this setup has been transported to other labs on campus for demonstration purposes.

As an alternative to the fixed permanent magnet and adjustable cavity, we employed a commercial TE₁₀₂ resonator in a field adjustable Halbach magnet (Fig. 3.5). As before, the resonance of the cavity was determined with a Bruker EMX spectrometer and EIP frequency counter. While the resonant frequency of the cavity depends on the NMR probe and sample, it was found to be repeatable as long as the probe, sample size, and sample position was not changed. Thus, once optimized the EMX spectrometer and frequency counter are not necessary so the setup can be portable. An SMA to waveguide adapter was used to couple the microwaves into the resonator, but this setup barely fit into the 100 mm bore of the Halbach magnet. This caused the sample to be placed off the center axis of the magnet where the field is less homogeneous by about a factor of 20 (see Materials and Methods section at the end of this chapter). We again determined the efficiency of this portable setup by measuring the DNP enhancement using 15 mM ¹⁵N 4-oxo-TEMPO dissolved in water. The magnetic field was adjusted so the electron spin Larmor frequency matched the resonant frequency of the cavity. This was done by measuring the ¹H NMR frequency as the field was adjusted. A ¹H enhancement of water of -80 was measured. This is lower than the -112 enhancement measured in the electromagnet and is likely due to significant broadening of the EPR line by the inhomogeneous magnetic field. Further work has been carried out to improve DNP efficiency in

inhomogeneous magnetic fields by adding small shim coils to the outside the cavity [98].

Figure 3.5. Function and design of the Halbach permanent magnet for DNP: a to c) rotation of the nested rings. a) both rings parallel ($\theta = 0^\circ$), b) perpendicular ($\theta = 90^\circ$) and c) antiparallel ($\theta = 180^\circ$). The vectors illustrate the vector addition of the fields. The center of the inner ring shows a simulation of the resulting field with field lines and gray shaded to illustrate direction and strength of the resulting field. d) photograph of the magnet.



C. Conclusion

This chapter described our efforts to improve the hardware for DNP experiments. In our initial work, a Bruker EMX EPR spectrometer was used as a microwave source. This source had a maximum power output of only 200 mW. The measured enhancement with 15 mM ^{15}N 4-oxo-TEMPO dissolved in water was only -46 while the predicted maximum enhancement was close to -130. Our custom built, high

power microwave source resulted in a measured enhancement of -112 for this sample, approaching the theoretical maximum. Further, as our microwave source and amplifier is compact, we developed two portable systems. Using a fixed field permanent magnet and a tunable cavity, we achieved a DNP signal enhancement of -65 using the same ^{15}N 4-oxo-TEMPO sample. Replacing the fixed field magnet with a variable field Halbach magnet and using a commercial resonator, an enhancement factor of -80 was measured. While neither portable system performed as well as the large electromagnet, improvements in cavity design should improve performance.

D. Materials and Methods

Sample Preparation

The free radicals 4-oxo-TEMPO and 4-amino-2,2,6,6-tetramethyl-1-piperidinyloxy (4-amino-TEMPO) were purchased from Sigma-Aldrich. Isotope enriched ^{15}N labeled 4-oxo-TEMPO was purchased from Cambridge Isotope Laboratories. ^{15}N labeled ammonia and D_6 -acetone were also purchased from Cambridge Isotope Laboratories and used to synthesize ^{15}N labeled 4-Amino-TEMPO following previously published procedures [74]. 4-Amino-Tempo was dissolved directly into de-ionized water while 4-oxo-TEMPO was initially dissolved at a high concentration into DMSO and then diluted into de-ionized water, the final solution containing no more than 5% DMSO by volume. Volumes of approximately 5 μL were loaded into 0.7 mm inner diameter silica capillaries and sealed with beeswax and used for both ESR and NMR measurements.

DNP and EPR measurements

ESR experiments were performed at 0.35 T in an field adjustable electromagnet (0—1.5 T) using a Bruker TE₁₀₂ rectangular resonant cavity operating at 9.8 GHz and a Bruker EMX spectrometer. A home built NMR probe for 14.85 MHz ¹H detection was inserted into the microwave cavity under tuned and matched conditions. The NMR experiments were carried out with a Bruker Avance 300 spectrometer when using the electromagnet and Kea NMR spectrometer (Magritek Limited, Wellington, New Zealand) was used with the portable magnets. DNP experiments were performed while continuously irradiating the sample at ~ 9.8 GHz using our custom built microwave amplifier. The frequency source is a phase-locked YIG synthesizer (Microlambda Wireless) with 27.5 mW output, tunable between 8-10 GHz with an accuracy of 100 Hz. The microwave output is sent through two step attenuators (Narda), split with Wilkinson power dividers (Minicircuits), directed through four solid state power amplifiers (Advanced Microwave Inc.) in parallel, protected against reflected power using coaxial isolators with at least 25 dB protection (UTE Microwave Inc), recombined again with a Wilkinson power combiner (MIDISCO), and directed into an SMA output with a measured output power of 23 W. A circuit diagram of this transmission device is shown in Fig. 3.1. The YIG oscillator requires a 10 MHz reference frequency input along with two voltage sources (5V, 0A and 15V, 0.34A) and a computer for adjusting the frequency via a parallel interface, with the supplied program (Microlambda Wireless). For these purposes, we employed an Instek PST-3201 triple output power supply and a Stanford Research Systems SC-10

as a 10 MHz reference source. A SMA to waveguide connector is used to couple the microwave output to the Bruker TE₁₀₂ cavity. The precise frequency for setting the YIG oscillator can be found by monitoring the DNP enhancement while adjusting the frequency or by monitoring the frequency at which the TE₁₀₂ cavity resonates when coupled to the Bruker X-band bridge (ER 041 MR; a Gunn diode source) using a frequency counter. This resonance frequency is accurately reproducible when using the same sample holder and NMR coil, but can vary significantly if either of these conditions is changed. For experiments using the fixed field magnet portable DNP setup, a 0.3487 Tesla (at 22.5° C with temperature variance of ~ 0.025%/°C) permanent magnet was purchased from Aster Enterprises, Inc. This magnet is relatively small in size and has a 35 mm gap to comfortably place the X-band microwave equipment.

For our portable DNP setup with a variable magnetic field, the custom built permanent magnet consists of two Halbach dipoles [100] realized by 2 nested MANDHALA rings [102] that can be turned relative to each other in order to change the resulting magnetic field manually [101]. The inner ring (ID 100 mm, OD 156 mm) is a stack of 8 layers each made from 16 octagonal permanent magnets (dimensions 24 × 24 × 22.2 mm) while the outer ring (ID 158 mm, OD 224 mm) consists of 6 layers of 24 quadratic permanent magnets (dimensions 18.6 × 18.6 × 32.1 mm). The principal design is shown in Fig. 3.5. All layers in both rings have individual distances optimized for maximal homogeneity using BEM software (AMPERES, Integrated Engineering Software, Winnipeg, Canada). Each layer

consists of an aluminum support with sockets to house the FeNdB magnets (Magnetic Component Engineering, Luton, UK) with a maximum energy product of 48.2 MGOe and a remanence of $B_r = 1.408$ T. Free rotation of the rings is assured by a ball-bearing at each end. The final magnet has a height of 230 mm and a weight of ca. 70 lbs. As shown in Fig. 3.5, the resulting effective magnetic field, B_e , is the vector sum of the fields of the inner ring, B_i , and the outer ring, B_0 . If the two rings are oriented at an angle, θ , the field is:

$$B_e = \sqrt{B_i^2 + B_0^2 + 2B_iB_0\cos\theta} \quad (3.1)$$

With $B_i \approx 0.3$ T and $B_0 \approx 0.15$ T the field can be varied from approximately 0.15 T at $\theta = 180^\circ$ to 0.45 T at $\theta = 0^\circ$. For X-Band DNP experiments with $B_e \approx 0.35$ T, $\theta = 84^\circ$. The homogeneity in the center of the magnet was determined by NMR to be better than 20 ppm over 5 mm diameter spherical volume at this field. DNP measurements were carried out 20 mm off center due to the size of the cavity with a field-homogeneity of ~ 400 ppm.

IV. Site Specific Hydration Dynamics of Apomyoglobin

A. Introduction

In the previous two chapters we developed a new theory for the saturation factor necessary for spin labeled biomolecules and improved our DNP efficiency with a custom microwave amplifier. In this chapter we apply Overhauser DNP to answer a question of biological relevance: is the hydrophobic core of a protein folding intermediate hydrated?

It is well appreciated that the hydrophobic effect is one of the dominant forces in protein folding [103-106]. However, the virtual absence of experimental evidence regarding the location and dynamics of disordered water has severely limited a quantitative assessment of the role of hydrophobic interactions to protein folding. Many proteins are known to fold via a rapid collapse of a hydrophobic core, followed by a slower search for the native state. The initial collapsed state is often identifiable as a discrete kinetic intermediate, and typically fits the description of a molten globule (MG). The exact nature of a MG is elusive as they are often unstable and lack significant structure. Generally however, a MG is compact, highly dynamic, and lacks a significant fraction of the native secondary structure. Whether MG folding intermediates bear a hydrated (i.e., wet) or dry nonpolar core, or whether any core-associated water is dynamic or motionally confined are current subjects of intense debate [107-112]. Experimental evidence on the nature of water interacting with the protein core is sorely needed given its fundamental relevance to the molecular nature of the hydrophobic effect and the putative mechanistic role of core-water extrusion in

protein folding. More generally, hydration water—defined as water whose dynamics are perturbed by the surface and extending up to 3 water layers—is increasingly recognized to play a direct role in equilibrium protein dynamics [44, 113], thus regulating protein function, activity, and binding events, in addition to folding. There is also disagreement on the timescale, nature, and role of this water [15; 16; 114-116], but experimental reports are lagging behind theoretical predictions. In order to obtain clarity on these fundamental questions, new techniques and more experimental studies are needed.

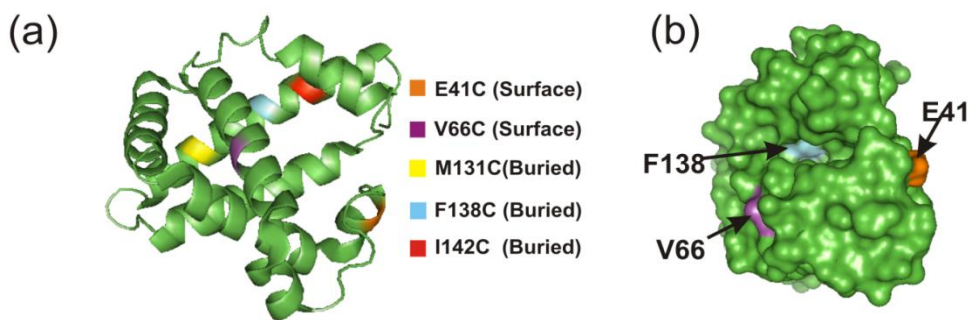
The experimental challenge is that hydration water of dilute protein solutions is difficult to detect since it has a spectroscopic signature largely indistinguishable from the more highly populated bulk water. Additionally, the landscape of protein hydration dynamics is extremely heterogeneous on the temporal (e.g. bound versus disordered water) as well as spatial (residue to domain) scale, requiring tools that can access hydration dynamics within a well defined timescale of interest as well as with site-specific resolution. Despite the availability of a number of techniques to study protein hydration water, including nuclear magnetic resonance relaxation dispersion [117-120], quasi-elastic neutron scattering [44; 121-123], inelastic neutron scattering [115, 124, 125], microwave dielectric spectroscopy [126, 127] and terahertz absorption spectroscopy [128], only femtosecond fluorescence spectroscopy [15, 16, 129-131] on (natural and substituted) tryptophan residues has been reported to map out protein hydration dynamics with site specificity.

In this chapter we apply the Overhauser DNP technique developed in the first three chapters of this dissertation to probe, with site-specific resolution, the translational dynamics of hydration water interacting with sperm whale apomyoglobin (apoMb) in its native (N-state), pH-unfolded (U-state), and MG states. The Overhauser DNP approach overcomes the above mentioned experimental challenges by amplifying the ^1H NMR signal of water within $\sim 10 \text{ \AA}$ around protein residues labeled with nitroxide radical spin labels [17]. As discussed in chapters one and two, the size of the signal enhancement at 0.35 T is sensitive to the translational (or rotational) dynamics of hydration water with correlation times between 10-500 ps. Also, as the same nitroxide spin label employed for DNP is used electron EPR, we conducted EPR measurements to gain information on the local environment, packing, and protein backbone dynamics around the spin label.

Apomyoglobin (apoMb; the prefix apo indicates the heme normally present as part of the structure is missing) is an eight α -helix globular protein that offers a unique chance to study the role of hydration water in protein folding since it populates a stable MG intermediate at $\sim \text{pH } 4.1$. While this species is clearly distinct from the apoMb kinetic folding intermediate, they have been shown to share key structural features [108, 132-136]. There exist several literature reports that investigate hydration dynamics in apoMb [44, 107, 117], but only time resolved femto-second fluorescence spectroscopy has reported water dynamics with site specific resolution [15, 16]. Figure 4.1 shows the native structure of apoMb and the sites chosen for site directed spin labeling (SDSL) with the nitroxide spin label

denoted R1 [14]. Three sites belonging to the H-helix, M131, F138, and I142, participate in the ABGH structural core populated in both the kinetic and MG folding intermediates. Site M131 is among the most protected sites in hydrogen/deuterium (H/D) exchange studies [137, 138] and is known to participate in nonspecific nonpolar interactions in equilibrium MG [139]. Two surface positions, E41 (C-helix) and V66 (E-helix), were also chosen as probes for hydration water on the protein exterior. We conclude that the MG state has a wet core with hydration dynamics intermediate between that of the native and the pH-unfolded states.

Figure 4.1. (a) Three-dimensional structure of native sperm whale myoglobin (PDB: 1mbc [140]). The solvent-exposed (E41C, V66C) and buried (M131C, F138C, I142C) mutation sites are highlighted in color. The image was created in PyMOL [70]. (B) Three-dimensional molecular surface representation of native myoglobin. This work focuses on apoMb so the heme group was omitted. This orientation enables visualizing solvent-exposed sites E41C and V66, and buried site F138 site, which faces the interior of the heme pocket.



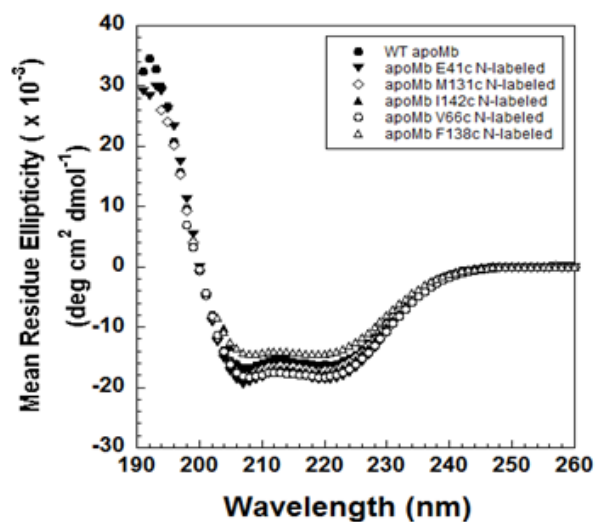
B. Results and Discussion

Effect of Spin Label on apoMb Structure

Introduction of a cystine point mutation and nitroxide spin label in each of the 5 apoMb single-variant species studied here is minimally perturbative and does not have a significant effect on the three-dimensional structure of the protein. This is illustrated

by the far-UV circular dichroism (CD) spectra of the five point mutations compared to the native wild type shown in Fig. 4.2. The five mutated species all have very similar CD spectra, showing the amount of α -helix formation in the mutants is near that of native apoMb. In addition, equilibrium pH titrations show that both the population of the MG intermediate at pH 4.1 and the pH dependence of apoMb unfolding is preserved in the mutants. Our previous molecular dynamics simulations with nitroxide radicals discussed in chapter 2 also showed the diffusion of water near the nitroxide radical to be very similar to that of bulk water [141]. Thus, we expect the dynamics of water near the spin probe of the five spin labeled mutants to be similar to those of native apoMb.

Figure 4.2. Far-UV circular dichroism spectra of wild type (●) and nitroxide-labeled (▼, ◇, ▲, ○, △) apoMb variants. Lyophilized protein samples (final concentration: 10-12 μ M) were dissolved in 10 mM sodium acetate at pH 6.1 followed by pH readjustment to 6.1. Data were collected at room temperature. The spectra shown in the figure represent the average of three independent experiments.

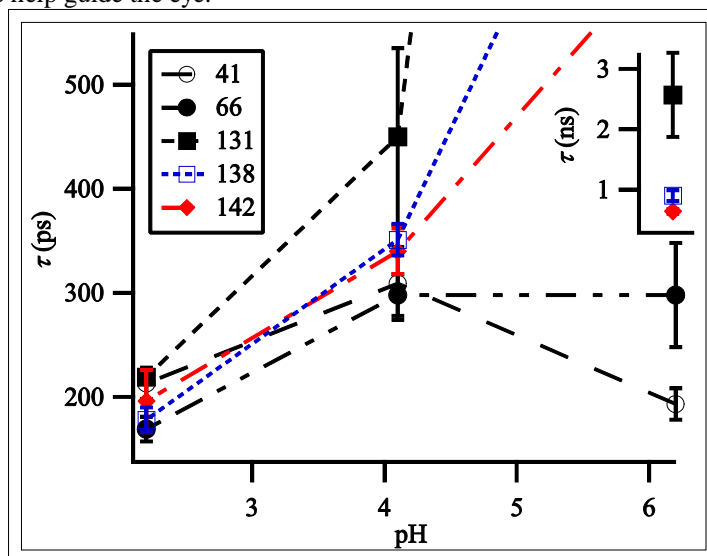


Hydrophobic Core

^1H DNP and T_1 measurements of water were used to determine the DNP coupling factor, ρ (Eq. 1.6). To estimate the timescale modulating the dipolar coupling we use the FFHS model discussed in chapters one and two. Although this is only an approximation, the trends displayed are general characteristics, i.e., ρ (which does not depend on a diffusion model) decreases with slower dynamics. The estimated values of τ_t for the different mutants in the N-, MG-, and U-state are shown in Fig. 4.3 and the corresponding ρ values are listed in Table 4.1. Clear differences are seen in τ_t among the chosen sites in the N-state. All the residues in the hydrophobic core display much slower dynamics than the exterior sites, implying the dipolar coupling is modulated on a slower timescale. From the view point of the FFHS model, this could be due to a smaller diffusion coefficient of water near the radical, D_I (Eq. 1.13; since $D_S \ll D_I$ for spin labeled molecules it can be ignored) or a larger distance of closest approach between the radical's e^- spin and ^1H nuclear spin of water, d . If the former is true, diffusion of water inside the protein core is not likely to be well approximated by the FFHS model, but the observed trends are still valid. Following the distinct differences in ρ , it is clear that interactions of water with the hydrophobic core occur on a much slower timescale than that of the solvent exposed sites, as expected. The values of the leakage factor, f , are also shown in Table 4.1. As discussed in chapter one (see Eq. 1.15 and Fig. 1.6), an increase in τ_t accompanied by an increase in f (for the same spin label concentration) is consistent with slower diffusion of nearby water. However, an increase in τ_t paired with a decrease in f is

consistent with a larger d . These are again general trends and not just true for the FFHS model, but are not necessarily the only possibilities as we discuss below. The value of f for the N-state of F138R1 is small compared to the other interior sites; hence we believe the slow τ_t for this residue is due to remote water on the surface of the protein, and not due to slowly diffusing water near the spin label. This is confirmed by our EPR results discussed below. Residues M131R1 and I142R1 have larger values of f , but quantitative EPR analysis were necessary to make a final determination to the cause of the observed larger τ_t .

Figure 3. Plot of τ_t in the N-state (pH 6.1), MG-state (pH 4.1), and U-state (pH 2.2) for the different mutants studied. The FFHS model was used to estimate τ_t from ρ . Note that the inset has a different scale. Lines are to help guide the eye.



The N-state EPR spectra of M131R1 and F138R1 shown in Fig. 4.4 display one highly immobile component and are consistent with tight packing of the side chains, suggesting there is no water in the immediate vicinity of these sites (technically there is a mobile component of these spectra as well, but this is due to a small amount of free label or unfolded protein and will be ignored). Additionally, frozen EPR spectra

(Fig 4.5) were taken for the purpose of determining the strength of the hyperfine A_{zz} interaction (listed in Table 4.1) since this parameter is sensitive to local polarity [49-51]. The N-states of M131R1 and F138R1 display the two smallest A_{zz} values, indicating the spin labels occupy nonpolar environments. These two sites have

Table 4.1. DNP results and the best fit values of microscopic order, macroscopic disorder fits of the EPR data. %*i* and %*m* are the % of the immobile and mobile component from the EPR fits respectively and τ_i and τ_m are the rotational correlation times of the *i* and *m* components. The *m* component of M131R1 and F138R1 in the N-state both show a small amount of free spin label or unfolded protein. Sample concentrations are $\sim 200 \mu\text{M}$.

Sample	f	$\rho \times 10^{-2}$	E_{max}	τ_i (ps)	A_{zz} (Gauss)	% <i>i</i>	τ_i (ns)	% <i>m</i>	τ_m (ns)
Free Tempo	0.1	22	-5.3	76	---	---	---	---	---
M131R1-N	0.74	0.15	0.3	2570	34.90	95	18.7	5	1.0
M131R1-MG	0.42	2.8	-6.8	450	35.10	60	18.7	40	2.0
M131R1-U	0.22	7.8	-10.1	219	---	---	---	---	---
F138R1-N	0.16	0.9	0.0	908	34.38	95	14.0	5	1.0
F138R1-MG	0.13	4.1	-2.5	351	35.38	59	14.0	41	2.1
F138R1-U	0.11	10.1	-6.3	178	---	---	---	---	---
I142R1-N	0.36	1.6	-2.8	642	35.40	61	10.0	39	1.5
I142R1-MG	0.27	4.3	-6.7	340	35.40	60	12.7	40	1.8
I142R1-U	0.21	9.0	-11.5	196	---	---	---	---	---
E41R1-N	0.24	9.1	-13.4	193	36.40	58	5.9	42	1.6
E41R1-MG	0.34	4.9	-10.0	309	35.74	57	8.5	43	2.1
E41R1-U	0.18	8.1	-8.4	213	---	---	---	---	---
V66R1-N	0.12	5.2	-3.1	298	36.22	---	---	100	3.1
V66R1-MG	0.16	5.2	-4.5	298	36.13	72	5.2	28	1.1
V66R1-U	0.12	10.7	-7.7	169	---	---	---	---	---

previously been found to have high protection factors from H/D exchange [137].

These results all point to the existence of a ‘dry’ hydrophobic core in the N-state of apoMb, implying the large values of τ_t for these residues is due to a larger d compared to the surface sites. However, a significantly larger f was measured for M131R1 compared to F138R1, pointing towards an interesting characteristic of M131R1, namely the possibility of bound water in the neighborhood of M131R1. It is

well appreciated that the contribution of a few bound water molecules (located in the protein interior or exterior) rotating with the global protein motion can contribute significantly to the overall relaxation rate [45, 47]. If a bound water molecule is near

Figure 4.4. Experimental EPR spectra (solid black lines) of the mutants studied in the N- and MG-state taken at X-band and 295 K. The dashed red lines are the fits to the data. The *i* and *m* indicate where changes in the immobile and mobile component are most visible. Note that the N-state spectrum of V66R1 is one component with resolved A_{\parallel} and A_{\perp} components. EPR spectra were taken with Ficoll 70 added to prevent global protein motion from contributing to the spectra.

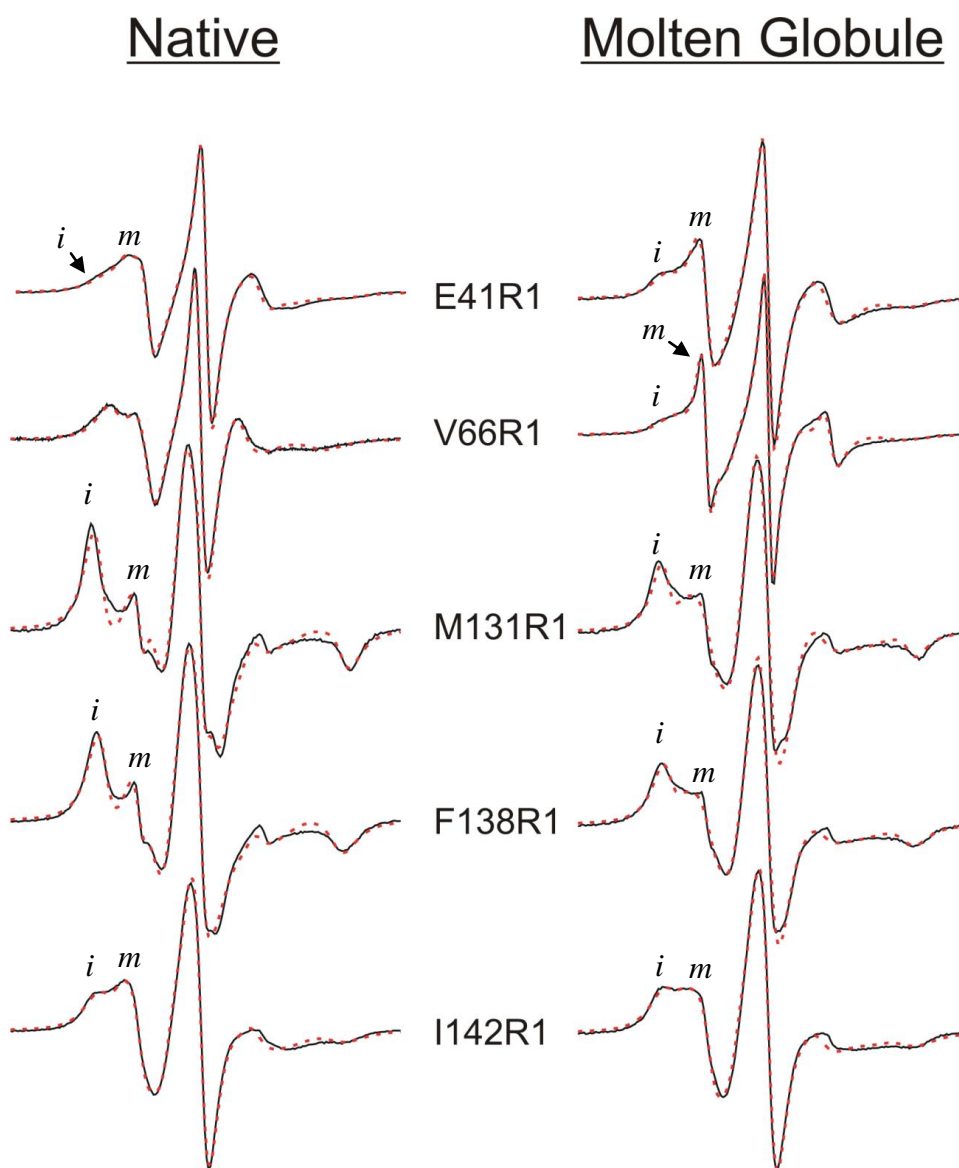
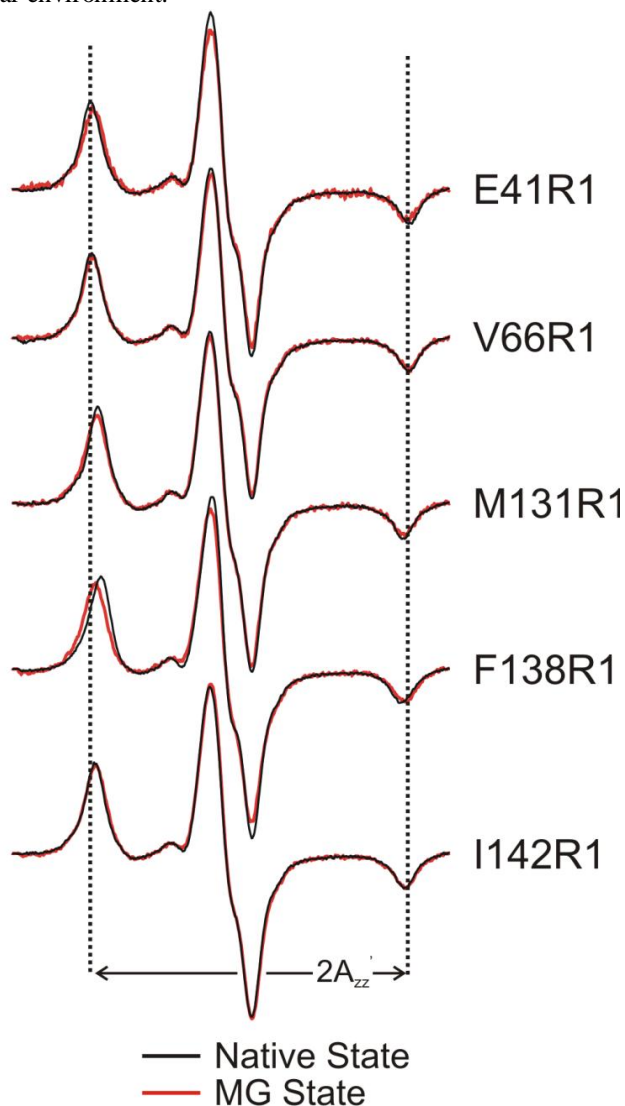


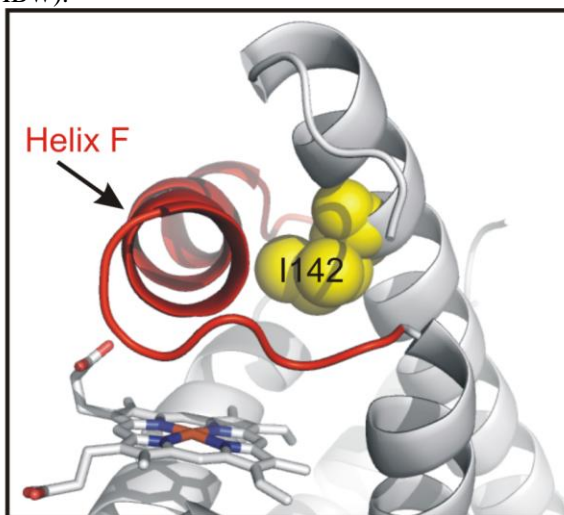
Figure 4.5. EPR taken at 223 K for accurate determination of A_{zz} . Larger values of A_{zz} indicate the spin probe is in a more polar environment.



an unpaired electron, the dipolar relaxation enhancement would be quite large. This extra relaxation would compete with the DNP effect, lowering ρ and increasing f , but the effect falls off with $1/r^6$ (Eq. 1.17b). Given the hydrophobic A_{zz} value and immobile EPR spectrum for M131R1, it is unlikely that the spin label is hydrated. Thus, we conclude that both M131R1 and F138R1 are ‘dry’ in the N-state and the

large differences in DNP parameters are due to the presence of bound water near M131R1.

Figure 4.6. Ribbon diagram of holo-myoglobin showing the position of the native isoleucine 142 in the holo-protein (PDB: 2MBW).



Among the buried sites in the native state, I142R1 has the smallest τ_t (fastest dynamics), largest A_{zz} value (highest polarity), and displays a two component EPR spectrum with a mobile and immobile component (Fig. 4.4). This second, mobile component is not observed for residues M131R1 and F138R1. Both NMR and EPR data have shown that the F-helix is in conformational exchange between a partially unfolded and folded structure resulting from the absence of the heme in the apo-protein [14, 21]. As shown in Fig. 4.6, I142R1 is packed against the F-helix in the holo-protein (i.e. myoglobin, not apoMb). We believe the two component EPR spectrum arises from a change in packing against the F-helix as it undergoes conformational exchange. These results taken with the DNP data imply I142R1 is partially hydrated, unlike M131R1 and F138R1. We therefore interpret the values of τ_t and f in terms of water dynamics, where the large values compared to the surface

sites imply a slow apparent diffusion coefficient for the hydration water instead of a larger d .

In the MG-state, all three buried sites have a two component EPR spectrum with an immobile component of $\sim 60\%$ and a mobile component contributing $\sim 40\%$ (Table 4.1). The more mobile spectra for M131R1 and F138R1 in the MG compared to the N-state suggest reduced packing of the side chains. Also, a measured increase in A_{zz} for F138R1, indicates this side chain is in a more polar environment in the MG-state than in the N-state. This is not unexpected as the A, B, G, and H helices making up the hydrophobic core are known to be *mostly* formed in the MG, but with some fraying at the ends [21] along with a decrease of H/D protection factors for all buried sites [137]. Taken together, these results point towards the hydrophobic core of apoMb being hydrated in the MG-state. This is consistent with the DNP measurements that display dynamic water with $\tau_t \sim 350\text{-}450$ ps for the buried sites in the MG state. Yet, the τ_t values for the buried sites in the MG-state are still larger than those of the exterior sites ($\tau_t \sim 300$ ps), consistent with the picture of a ‘looser’ hydrophobic core that is largely, but not completely formed.

While both the τ_t and f values of all interior sites significantly decrease in the MG compared to the N state, M131R1 again displays the largest τ_t and f values, and most immobile EPR spectrum. This could be due to the motion of water near M131R1 being more restricted compared to F138R1 and I142R1. It is also possible, that bound water continues to play a role in the MG-state (as assumed to be the case in the N-state), although to a lesser extent due to the more dynamic nature of the MG. It is

interesting that the EPR spectrum for I142R1 in the MG-state is similar to the N-state, while the DNP results show a significant decrease in τ_t and f , implying faster water dynamics near in the MG-state for this residue. This shows that hydration dynamics around protein residues can be distinctly different, while the local protein dynamics are similar. Lastly, it is important to note that the estimated τ_t of 350-450 ps represents a weighted average between the different conformations that the MG state is probing, as presented by the two EPR components.

Solvent Exposed Residues

The large differences in τ_t observed between the buried sites versus those exposed to the solvent (E41R1 and V66R1) in the folded state confirm that water is able to more freely diffuse on the exterior of the protein. The observation of heterogeneous surface hydration dynamics, especially in the N state, emphasizes the importance of employing site-specific probes as the charge, polarity and local topology may all contribute to variations of local water dynamics [15, 16, 142]. The N-state values for τ_t of 190 and 300 ps for E41R1 and V66R1 respectively are about 2-4 times slower than our measured τ_t of 76 ps for bulk water [19]. This is in agreement with previous results that found surface hydration water is slowed by a factor of 2-4 compared to bulk water [44, 45, 117, 123, 142]. The EPR spectrum for both surface sites also display much higher mobility compared to the buried sites, as expected (Fig. 4.4 and Table 4.1).

A dramatic increase in τ_t is observed for E41R1 in the MG-state compared to the N-state, which is an unexpected result. The EPR spectrum of E41R1 in the MG- as

well as in the N-state has two components, but the mobility of the side chain is reduced in the MG-state. The A_{zz} value of E41R1 also decreases, suggesting reduced polarity at this site in the MG- compared to the N-state. We propose the decreased mobility, polarity, and the increase in τ_t and f are due to the MG sampling non-native conformations in which E41R1 gets partially buried in more hydrophobic regions. This is consistent with NMR data on apoMb that implied stabilization of the C-helix was due to packing against the hydrophobic core, although this region undergoes considerable conformational averaging [21]. A previous study using time resolved fluorescence spectroscopy also mapped out hydration dynamics around site E41, but found faster hydration dynamics in the MG- compared to the N-state for this residue [16]. This study also found that the hydration dynamics of E41 were similar to those of buried sites—a trend clearly not observed with DNP nor generally expected. As mentioned for MG interior sites, our DNP results report on hydration dynamics averaged over different conformations. It is possible that tryptophan fluorescence spectroscopy is not equally sensitive to conformations with distinctly different exposure to water, which may explain the conflicting observations.

The DNP results for V66R1 in the MG-state are very similar to that of the N-state, but the EPR spectrum is quite different and now presents two components. The two component spectrum is likely due to conformational averaging in the E-helix as previously reported [21]. The A_{zz} value for V66R1 does not change much in the MG compared to the N-state, suggesting the polarity of the local environment remains similarly high. Although the backbone dynamics around 66R1 differ significantly

between the N and MG-state, the DNP results suggest the dynamics of hydration water is similarly fast between the two states. However, it is possible that the hydration dynamics of the two conformations of the MG-state differ significantly and their weighted average coincidentally happens to be the same as the N-state. Given that the N-state is already hydrated with dynamic water, we consider this scenario unlikely.

Acid Unfolded State

All residues studied display characteristics of full solvent exposure with τ_t between 169-219 ps in the U-state and mobile single component EPR spectra. The dispersion in τ_t is much smaller than observed in the MG and N-states, but small differences are still observed. The dramatic decrease in the dispersion of τ_t suggest that the local topology, charge, hydrophobicity, and polarity upon formation of the secondary or tertiary structure is a stronger determinant of local hydration dynamics than the characteristics of the primary protein sequence. The small dispersion that persists in the U-state may arise from non-negligible polar or charge effects in the primary amino acid sequence, or from some remaining helical structure known to persist in the U-state [21].

C. Conclusion

We find the hydration dynamics of the native state of apomyoglobin to be vastly heterogeneous, with clear differences observed for each site investigated. In the N-state, the interior residue I142R1 directly interacts with dynamic water, but on a much slower timescale than the solvent exposed residues. This is likely due the disordered

F-helix of the apo-protein, while the interior residues, M131R1 and F138R1 display characteristics of a ‘dry’ hydrophobic core. The two surface sites, E41R1 and V66R1, in the N state both display fast hydration dynamics that are only 2-4 times slower than bulk water dynamics. The EPR spectra of the molten globule agree with previous studies showing the H-helix is mostly formed. However, all sites studied show two component EPR spectra with a more mobile conformation, suggesting reduced packing of the side chains and some conformational averaging. The DNP experiments found significantly faster hydration dynamics for the buried sites in the MG-state compared to the N-state. Taking the DNP and EPR observations together, we conclude that the interior of the molten globule is hydrated with dynamic water. Still, the hydration dynamics of these buried sites are measurably slower than the surface sites in the MG-state. A peculiar observation was made for, E41R1, which displayed greatly slowed dynamics compared to the N-state; in contrast to a previous study [16]. We attribute this slowing down to the protein side chain sampling non-native conformations in which the spin label becomes somewhat buried in the MG state. The large dispersion for τ_t observed in the N-state is reduced in the MG-state, and further reduced in the acid unfolded state, implying that the local topology determined by the protein structure significantly impacts the hydration dynamics landscape and amino acid sequence specific effect play a secondary role.

D. Materials and Methods

Protein expression, purification and general characterization.

A modified pET-17b vector (Novagen, Madison, WI) carrying the gene for wild type sperm whale myoglobin was a generous gift from Steven Boxer (Stanford University, CA). Five mutagenic plasmid DNAs, each carrying one of the apoMb cysteine (Cys) point mutations E41C, V66C, M131C, F138C and I142C were generated via the QuickChange kit (Stratagene, La Jolla, CA), as described [14]. Each plasmid was transformed into *E. coli* BL21 DE3 cells (Novagen, Madison, WI). *In vivo* protein expression was carried out in LB medium at 37°C. ApoMb overexpression was induced upon addition of isopropyl-β-D-thiogalactopyranoside (1 mM) at OD₆₀₀ = 0.8. Cells were harvested at OD₆₀₀ ≈ 1.8. Cell lysis, inclusion body resuspension and HPLC purification were performed according to published procedures [143, 144]. Protein purity and identity were verified by reverse phase analytical HPLC and either electrospray ionization or MALDI mass spectrometry.

Generation of nitroxide-labeled apoMb.

Lyophilized apoMb was solubilized in 6 M urea and 10 mM sodium acetate at pH 6.1 for 30 min at 4°C. For mutants carrying surface Cys (E41C and V66C), the solubilized protein was diluted seven-fold in 10 mM sodium acetate at pH 6.1. A 10-fold molar excess of 1-oxyl-2,2,5,5-tetramethyl-Δ³-pyrroline-3-methyl methanethiosulfonate (MTSL, R1; Toronto Research Chemicals, North York, Ontario) was added under gentle stirring at 4°C. For mutants carrying buried Cys, (M131C, F138C and I142C) the solubilized protein was diluted 2.1-fold with 10 mM

sodium acetate at pH 6.1 to a final 2.8 M urea concentration before rapid addition of a 10-fold molar excess of MTSL under stirring at 4°C. Both reactions were allowed to proceed for 18 hrs at 4°C. The reaction mixture for the mutants carrying the buried Cys was diluted 3.3-fold with 10 mM sodium acetate at pH 6.1 and incubated for 30 min at 4°C under gentle stirring, to promote refolding. After the above treatment, each protein solution was dialyzed extensively against 10 mM sodium acetate at pH 6.1 at 4°C to eliminate urea and excess MTSL. Spin-labeled protein solutions were then independently concentrated with an Amicon Ultra device (3,000 MWCO; Millipore, Billerica, MA) and flash-frozen in separate aliquots. Protein concentrations were assessed by absorption spectroscopy ($\epsilon_{280} = 15,200 \text{ cm}^{-1}\text{M}^{-1}$). Labeling efficiencies were assessed by reverse phase analytical HPLC on a C₁₈ column (Grace, Deerfield). Labeling efficiencies for the E41R1 and V66R1 mutants were >95%, and labeling efficiencies for the M131R1, F138R1 and I142R1 mutants varied between 61 and 90%. Successful apoMb spin labeling was confirmed by electrospray ionization or MALDI mass spectrometry and electron spin resonance.

Sample preparation for DNP measurements

In preparation for DNP experiments, frozen sample aliquots were thawed in an ice bath and kept cold until ready for DNP data collection. The pH of the samples was adjusted using 0.1 M HCl or NaOH for the pH 4.1 and 6.1 samples and 1 M HCl was used to decrease the pH to 2.2 for the unfolded samples. Samples were then passed through a Sephadex G-25 column to remove any aggregated species [134]. Prior to loading the sample on the spin column, the column was equilibrated by repeated

washes with buffer at the sample pH as the sample. The concentration of protein was checked after the spin column by measuring the absorbance at 280 nm. Samples were slightly more dilute after the spin column with typical concentrations of $\sim 200 \mu\text{M}$.

Far-UV circular dichroism (CD): spectral data collection

Far-UV CD experiments were carried out at equilibrium on a MOS-450 spectropolarimeter (Bio-Logic Science Instruments, Claix, France) with a 1 mm pathlength cuvette (Hellma, Müllheim, Germany). CD scans were performed at room temperature in 1 nm steps, with 20 s signal averaging per step. Mean residue ellipticity (MRE; $\text{deg cm}^2 \text{dmoI}^{-1}$) was determined according to the relation $MRE = \theta / 10CN_A l$ where θ denotes the experimental ellipticity (in mdeg), C is the molar concentration of the protein, N_A is the number of amino acids ($N_A = 153$ for apoMb), and l is the cuvette path length (in cm).

Far-UV circular dichroism (CD): pH titrations

Equilibrium pH titrations on all the nitroxide-labeled apoMb variants were performed by far-UV CD at 222 nm quartz cuvettes with 10-mm path length at room temperature. A concentrated protein stock solution (ca. $300 \mu\text{M}$ in 10 mM sodium acetate, pH 6.1) was diluted into 1 mM sodium acetate at pH 6.1 to generate $\sim 20 \mu\text{M}$ protein solutions. The pH of these starting solutions was progressively lowered upon addition of either 0.1 M or 1 M acetic acid (to pH down to ~ 3) or concentrated HCl (to pH < 3). Samples were allowed to equilibrate at the desired pH for ≥ 10 min., prior to data acquisition, and data were collected in sequence on the same sample. Independent duplicate pH titrations were performed on each apoMb variant.

DNP and EPR Experiments

DNP experiments were performed at 0.35 T in a Bruker TE₁₀₂ rectangular cavity using a homebuilt NMR probe and a Bruker Avance 300 NMR spectrometer. Experiments were performed at room temperature and air was continuously flowed through the cavity to minimize sample heating. Also, only ~ 3 μ L of sample was loaded into a 0.64 mm inner diameter quartz capillary to minimize the electric field component of the microwave radiation at the sample, and thus heating. Further details of the DNP hardware were previously described in chapter three. Prior to each DNP experiment an EPR spectrum of the same sample was taken, and the magnetic field set to the position of the center line. To determine the leakage factor, T_1 measurements were performed in a wide bore Oxford superconducting magnet charged to 0.35 T. The broadband channel of a commercial Bruker probe was used to perform an inversion recovery pulse sequence and the data fit to $I_z = I_0 - 2A\exp(-t/T_1)$ where I_0 , A , and T_1 were fit parameters.

The EPR spectra were recorded at 295 K in a Bruker ELEXSYS 580 fitted with a high-sensitivity resonator using an incident microwave power of 20 mW and modulation amplitude of 1 Gauss. Samples of at least 6 μ l were loaded in sealed capillary tubes (0.6 ID X 0.84 OD; VitroCom, Inc., NJ). Spectra were recorded at X-band frequency with a scan width of 100 Gauss. The spectra were recorded in 25% (w/w) Ficoll 70 in order to increase the solution viscosity, and thereby minimize the contribution from protein rotational diffusion to the EPR spectral line shape [14]. The final protein concentration for EPR measurements was ~ 200-400 μ M. To obtain the

experimental hyperfine splitting values ($2A_{zz}$) in the absence of motion, the EPR spectra were recorded at 223 K using an incident microwave power of 0.2 mW and a modulation amplitude of 2 Gauss. The hyperfine splittings were determined by individually fitting the low- and high-field peaks to a mixture of Lorentzian and Gaussian lineshapes using the Xepr program (Bruker, Germany) and by measuring the magnetic field separation between the low- and high-field peaks to obtain $2A_{zz}$.

Single- and multiple- component EPR spectra were simulated with the NLSL program assuming a two-component MOMD (microscopic order, macroscopic disorder) model to describe the anisotropic motion of the nitroxide [53]; the software is available at <ftp://ftp.ccmr.cornell.edu/pub/freed>. For all simulations the starting values for the \mathbf{A} and \mathbf{g} magnetic tensors were taken as $g_{xx} = 2.0078$, $g_{yy} = 2.0058$, $g_{zz} = 2.0022$, and $A_x = 6.2$, $A_y = 5.9$. The A_z value for each residue was obtained as described above (223 K) and was kept constant during the fitting procedure. The \log_{10} of the three components of the rotational diffusion tensor are given in a modified spherical form as $\langle R \rangle = \frac{1}{3}(R_x + R_y + R_z)$, $N = R_z - \frac{1}{2}(R_x + R_y)$, and $N_{xy} = (R_x - R_y)$, where R_x , R_y , and R_z are the principal components in Cartesian form. The immobile states of E41R1, V66R1 (MG-state), and I142R1 are taken to have isotropic motion with $N = N_{xy} = 0$, while the other states have axially symmetric z-axis anisotropic motion with tilt angles of the diffusion tensor $\alpha_D = 0^\circ$, $\beta_D = 36^\circ$, $\gamma_D = 0^\circ$, and subject to an ordering potential described by the coefficient C_{20} from which the order parameter is computed. Least-square fits were obtained by variation of $\langle R \rangle$, N , C_{20} . After these parameters were optimized, the principal values of \mathbf{A} and \mathbf{g} magnetic

tensor (except A_{zz}) were allowed to vary slightly to obtain the final best fit. From the final fits, the effective correlation time was calculated as $\tau = 1/6\langle R \rangle$ [53] and reported in Table 1.

V. A 200 GHz Quasi-Optical DNP and EPR Spectrometer

A. Introduction

As mentioned in chapter one, most NMR experiments are carried out high magnetic fields due to greater sensitivity and spectral resolution. These same advantages can be taken advantage of in DNP experiments at high field, although this is experimentally much more challenging as the e^- spin resonance frequency is already 95 GHz at 3.35 T (still a small magnetic field compared to standard NMR magnets). However, recent years have seen a resurgence in the use of high field DNP detected by both NMR and EPR with applications including structure and dynamics of biological molecules [145-147], reaction monitoring, [148, 149] imaging, [150, 151] and the study of electron-nuclei interactions [12; 152- 154]. Much of this is due to advances in methods [155, 156] and technology [26, 27] resulting in improved DNP efficiency, increasing the range of samples that can be studied, and wider availability of instrumentation. These developments have led to a number of commercial instruments, for instance a 9 T gyrotron-based system by Bruker Biospin and diode-based 3.35 T dissolution systems by GE and Oxford. As impressive as these achievements are, the fact remains that commercial instruments are expensive and require significant lab space, while building a gyrotron-based microwave source or a sub-1.5 K cryogenic system with rapid melting and sample shuttling is beyond the expertise of most groups. We pursue to bridge this gap by building a comparatively inexpensive and compact DNP and EPR spectrometer based on a solid

state 200 GHz source and a quasi-optical, millimeter-wave bridge. This system was added onto an existing 7 T, vertical bore magnet.

Quasi-optical techniques have been employed in EPR experiments for over two decades at frequencies ranging from 95 to 420 GHz [157-165]. Quasi-optical transmission has several advantages over waveguides for millimeter-wave propagation. As the radiation propagates through free space guided by mirrors and wire-grid polarizers, the quasi-optical bridge is nearly lossless. Another key feature of our bridge is that the only components that are frequency dependent are the source and detector, giving the potential to perform EPR and DNP experiments over a wide range of frequencies. Finally, optical techniques allow the polarization of the beam to be used as a means to separate the EPR signal returning from the sample from the reflected background signal, enabling up to 60 dB of isolation [166]. The capability of manipulating the polarization of light can be further utilized to excite electron spin resonance transitions using circularly, as opposed to linearly, polarized radiation that results in an up to two-fold gain in effective power [158, 162] as only the handedness of polarization in the direction of the e^- precession can excite e^- spin transitions. Solid state sources only have tens of milli-watts of power at 200 GHz, and many high field DNP experiments require high microwave power, particularly at higher temperatures where enhancements are often power limited. We propose to employ circularly polarized 200 GHz radiation for DNP experiments to make the most efficient use of available power.

In this chapter we describe our unique experimental setup that is capable of performing both DNP and EPR experiments and report on our initial results. The main components of this instrument are a quasi-optical bridge equipped with a frequency-tunable and switchable solid state 200 GHz diode source. A Martin-Puplett interferometer [162, 167] is built into the quasi-optical bridge to allow for easy adjustment from circularly polarized radiation for DNP experiments to linearly polarized radiation for induction mode EPR detection. The bridge is mounted on an optical table and aluminum stand, and guides the beam into a corrugated waveguide placed within a cryostat inside the vertical bore of a 7 T magnet. The entire setup does not require significant space around the magnet, can be added to existing standard or wide bore magnets, and is an order of magnitude less expensive than commercial instruments. Few systems exist above 5 T that can make both NMR-detected DNP and EPR measurements [168], and ours is unique as field swept EPR detection is built in as a permanent part of the setup. This bridge design has since been copied by other groups for DNP experiments [169]

DNP and EPR experiments were carried out at 4 K on a sample of ^{13}C labeled urea with 40 mM trityl radical dissolved in a deuterated glycerol/water solution. Unlike nitroxide radicals, the unpaired electron of a trityl radical belongs to a carbon nucleus that is 99% ^{12}C which is spin 0. Therefore, the trityl radical has only a single, narrow EPR line. For these sample conditions DNP signal enhancements were not limited by the power of our diode source. We also demonstrate that when operating in a power-limited regime, utilizing circularly polarized radiation increased

the DNP signal enhancements by 28% compared to linear polarization. The ability to manipulate the polarization of light demonstrates the value of using quasi-optical techniques. Further improvement is expected at higher temperatures or when saturating broader EPR spectrum where limited power becomes more problematic.

B. Experimental

Quasi-Optical bridge

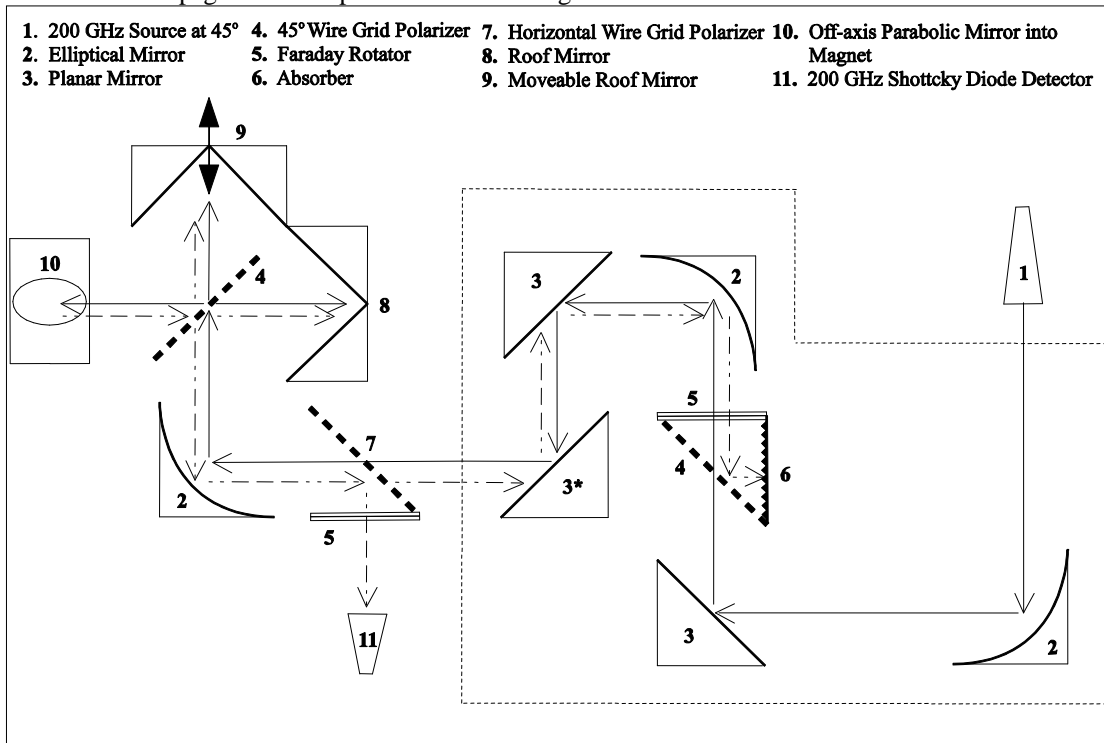
A figure of the reflection mode, quasi-optical EPR bridge is shown in figure 5.1. The diode source, purchased from Virginia Diodes Inc., is tunable in the range of 193-201 GHz, and consists of a 12 – 12.5 GHz yttrium-iron-garnet (YIG) oscillator (from Microlambda Wireless) that passes through a voltage-controlled attenuator before being multiplied up 16 times by 4 doublers. The peak power of the source is ~ 70 mW. The setup currently operates in continuous wave (cw) mode, but it is possible to implement pulse operation in the future with the addition of a pin switch. The source connects to a feed horn that outputs a Gaussian beam with a waist radius of 4 mm. The output horn, quasi-optical bridge, and a corrugated waveguide for propagation of the microwaves into the magnet were purchased from Thomas Keating Ltd. (with a corrugated waveguide extension purchased from Bridge 12 Technologies Inc.). All optical components are mounted onto an aluminum plate, patterned so that pieces can be easily moved for different applications.

In configuration A (defined in Fig. 5.1) the source is mounted so that the polarization of the beam is 45° to the normal of the page. The beam reflects off an elliptical mirror (all elliptical mirrors have a focal length of 25 cm), planar mirror,

and then into the quasi-optical equivalent of an isolator [170] consisting of a 45° wire-grid polarizer (transparent to the incoming beam), Faraday rotator, and absorber.

The Faraday rotator changes the polarization by 45°, so the beam that exits is

Figure 5.1. Schematic of the quasi-optical bridge. This experimental setup is referred to as configuration A. The section in the dashed box was removed for some to avoid the misalignment losses of the extra mirrors needed to maintain the correct path length between elliptical mirrors. In this setup, the source is placed at planar mirror 3* and oriented such that the polarization leaving the source is normal to the page. This setup is referred to as configuration B.



polarized normal to the page. These first two elliptical mirrors are necessary so that an image of the source is formed at the location of the planar mirror 3* [171] to act as a source for the Martin-Puplett interferometer. The planar mirrors are only necessary due to the limited space on our optical bridge and in principle are not necessary. None of the components in the boxed in portion of Fig. 5.1 are necessary for DNP, EPR detection, or to switch the polarization between linear and circular, but the addition of the quasi-optical isolator reduces standing waves which increases the isolation of the

EPR signal, and also helps to protect the source from reflected power. The Faraday rotator has a small loss of ~ 2 dB but this loss is usually offset by gains from the elimination of standing waves. Misalignments of the extra mirrors needed for the isolator (discussed below) however resulted in larger losses. Therefore, some DNP experiments presented were done with this section removed, and the source placed at the location of the planar mirror 3*, oriented such that the polarization leaving the source was normal to the page (referred to as configuration B). It is important to mention that more careful and accurate alignment should reduce the observed power losses significantly.

From the third planar mirror, the beam passes through a horizontal wire-grid polarizer and into the Martin-Puplett interferometer. There, a 45° wire-grid polarizer acts as a beam splitter, creating two separate path lengths. The two roof mirrors rotate the polarization 90° upon reflection. The recombined beam leaving the beam splitter will have a polarization that is a function of the path length difference, Δ , between the two roof mirrors. When $\Delta = 0 \pm 2\pi n$ or $\lambda \pm 2\pi n$, where n is an integer, the polarization of the beam is linear, while for $\Delta = \lambda/4 \pm 2\pi n$ or $3\lambda/4 \pm 2\pi n$ the polarization is left or right circularly polarized respectively [167]. Note that for all other path length differences, the polarization exiting the interferometer will be elliptical.

When on resonance with linear polarization irradiating the sample, a small cross polarized EPR signal is reflected back up the corrugated waveguide along with a large background signal [162]. In the ideal situation, only the EPR signal (dashed line

in Fig. 5.1) is reflected by the horizontal wire-grid polarizer and into the 200 GHz Schottky diode detector (Virginia Diodes Inc.). The remaining background signal (dotted-dashed line in Fig. 5.1) will travel back to the quasi-optical isolator and dumped into the absorber. If circularly polarized radiation is incident upon the sample (as is done for DNP experiments), the opposite is true and most of the reflected power from the sample will be directed into the detector. Typically a 15-20 dB of isolation was measured between the forward power and power reflected into the detector when linear polarization was used. Inclusion of the isolator in configuration A increased the isolation an additional 6-10 dB through the elimination of standing waves. Currently, our EPR detection has limited sensitivity as we lack homodyne or heterodyne detection. This is not a fundamental impediment however, and can be added to the bridge by adding a local oscillator reference arm to the bridge.

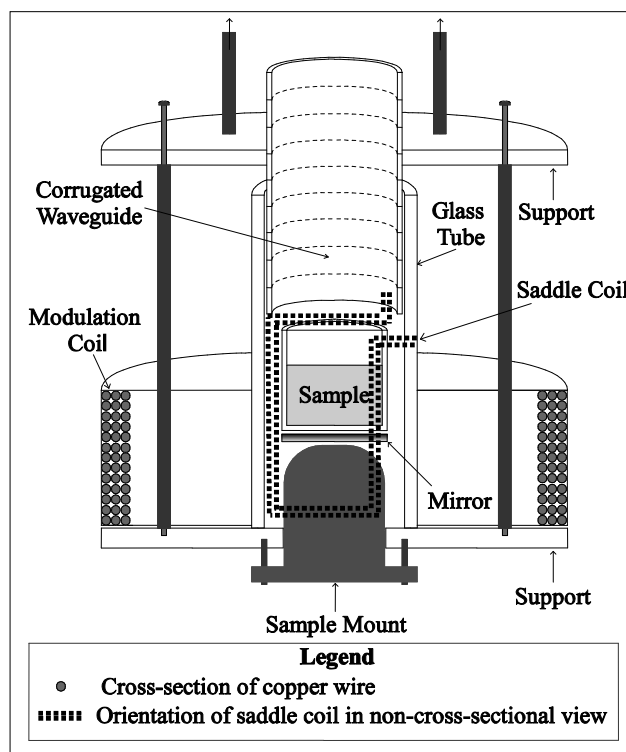
The optical bridge is held above the magnet with an aluminum stand (homebuilt) that allows for adjustment of the bridge in all three dimensions as well as the angle for accurate alignment of the microwave beam into the waveguide. As the wavelength is only 1.5 mm, the ability to adjust the height, position, and angle of the quasi-optical bridge above the magnet is crucial as coupling of the microwaves into the corrugated waveguide is sensitive to small misalignments [172]. The alignment was checked with a pyroelectric detector at the end of the corrugated waveguide inside the magnet to measure the relative power that is coupled into the waveguide.

EPR/DNP Probe

From the quasi-optical bridge, the microwaves are coupled into a 12.5 mm diameter corrugated waveguide that is placed into the 89 mm bore of a 7 T Bruker magnet. As the waveguide approaches the center of the magnetic field, it tapers to 5.3 mm. Figure 5.2 shows a schematic of the combination EPR/DNP probe. Approximately 50 μL of sample is placed in a polyethylene sample holder that rests on a mirror, and is placed against the exit of the corrugated waveguide. A 75.5 MHz copper wire saddle coil was built around a 12 mm OD/10 mm ID pyrex glass tube, that encloses the sample and is held in place from the bottom by a support attached to the waveguide. No effort was made to contain the microwaves between the end of the waveguide and the mirror below the sample. This certainly results in a loss of sensitivity in our EPR detection and may also reduce our isolation due to scattering of radiation. The tuning circuit for the NMR coil was a simple parallel LC circuit made with non-magnetic fixed chip capacitors (American Technical Ceramics) that were mounted near the coil. A 3.8 cm OD solenoid modulation coil (magnetic field parallel to B_0) for EPR was wrapped around a teflon cylinder and placed just below the sample and outside the NMR coil. Semi-rigid coaxial cables were used to connect the modulation coil to the output of a Stanford Research Systems lock-in amplifier and the NMR coil to a Bruker Avance 300 MHz (2 channel) NMR spectrometer. A resistive sweep coil, generously provided to us by R. David Britt at UC-Davis [173], was placed inside the bore of the 7 T magnet. An Agilent 120 V, 18 A power supply provides the sweep coil with a maximum field of ± 380 Gauss. A Janis STVP-200-NMR cryostat was custom designed to fit inside the resistive sweep coil and used to

cool the sample to 4 K. Temperature was measured with a Cernox temperature sensor (Lake Shore Cryotronics, Inc.) placed below the NMR coil and controlled with an Oxford ITC 503 temperature controller. A vacuum tight support structure for the waveguide and cables was designed by Bridge 12 Technologies Inc. and built in the Chemistry Department machine shop at UCSB.

Figure 5.2. Drawing depicting the EPR/NMR probe. Not shown are the capacitors that were mounted on the glass tube or connections to the coaxial cables.



EPR and DNP measurements

Before performing an EPR experiments, the setup first needs to be adjusted to ensure linear polarized radiation is employed. For this purpose, the moveable roof mirror position of the Martin Puplett interferometer (see Fig. 5.1) was varied, while the source was amplitude modulated at 200 Hz with a TTL pulse for lock-in

detection. The reflected power on the detector was measured as a function of mirror position. The minimum of this curve corresponds to linear polarization, and this position was used for induction-mode EPR detection. During an EPR experiment, the B_0 field was swept using the resistive sweep coil. A lock-in amplifier was used to drive a solenoid B_0 modulation coil at 35 kHz and detect the signal from the 200 GHz Schottky diode detector. The source power and modulation amplitude were chosen to minimize line broadening of the EPR signal. The program Labview was used to control the resistive coil and record the signal from the lock-in amplifier, as well as control the position of the moveable roof mirror. Since our current setup does not allow for coherent detection, data was exported into Mathematica and a Hilbert transform was applied to adjust the phase of the EPR spectra [174].

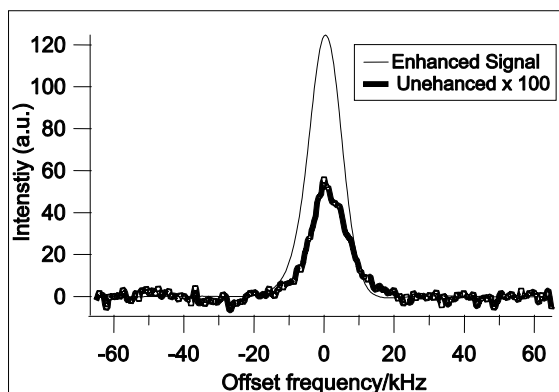
Except where noted, DNP experiments were done with maximum microwave power (~ 70 mW). The NMR saddle coil was measured to have a $\pi/2$ pulse of $8 \mu\text{s}$ at 75.48 MHz. A DNP experiment began by applying a series of saturation pulses of 25 ms duration to destroy the ^{13}C z-magnetization. This was followed by a delay time, during which the sample was irradiated with microwaves. The resulting ^{13}C z-magnetization was read out using a $\pi/2$ excitation pulse. The only exception to this sequence was when measuring the decay of magnetization after irradiating the sample with microwaves for ~ 2 hours. In this experiment the microwaves were turned off and 1° rf excitation pulses applied at various times to measure the decay of the DNP-enhanced NMR signal without substantially depleting the z-magnetization.

C. Results and Discussion

To characterize our setup, we performed DNP and EPR experiments on a sample of 12 M ^{13}C labeled urea dissolved in a 50/50 by volume mixture of D_2O and d-glycerol with 40 mM of the trityl radical Oxo 63 at 4 K (the structure of this radical can be found in ref. [175]). Ardenkjaer-Larsen et. al. used a similar sample in their pioneering work, and although they noticed a decrease in NMR signal enhancements above 15 mM trityl concentrations, there was also a significant shortening of the DNP build up and T_1 relaxation times [26]. The 40 mM trityl concentration was thus chosen to shorten the experimental time, while still obtaining high DNP polarization. Figure 5.3 shows the ^{13}C NMR spectra with and without microwave irradiation after a build up time of 3,500 s using configuration B (Fig. 5.1). The measured enhancement factor is 225. The DNP enhancement was not observed to vary with decreasing microwave power until ~ 7 dB of attenuation was applied (i.e. ~ 15 mW output power) in this setup. Even though the Faraday rotator was measured to have only 2 dB of insertion loss, its inclusion as part of configuration A decreased the enhancement values further than what is expected from the 2 dB decrease in power. We estimate that the effective attenuation amounts to ~ 10 dB when switching from configuration B to A. We attribute this to misalignment of the five extra mirrors in configuration A that must be included with the quasi-optical isolator in order to maintain the correct path length to image the source on the corrugated waveguide [171, 176]. It is a known problem that at higher microwave frequencies, as employed here, that misalignment of optical components results in greater losses than at lower frequencies [172]. We observed decreases in power to the sample as large as 50% with misalignments of

0.1°. More careful alignment should reduce this loss. In our current setup, the alignment can only be checked by removing the NMR probe and replacing it with a pyroelectric detector. Thus, once the sample was cooled in the magnet, the alignment was not re-adjusted when switching from configuration B to A in Fig. 5.1.

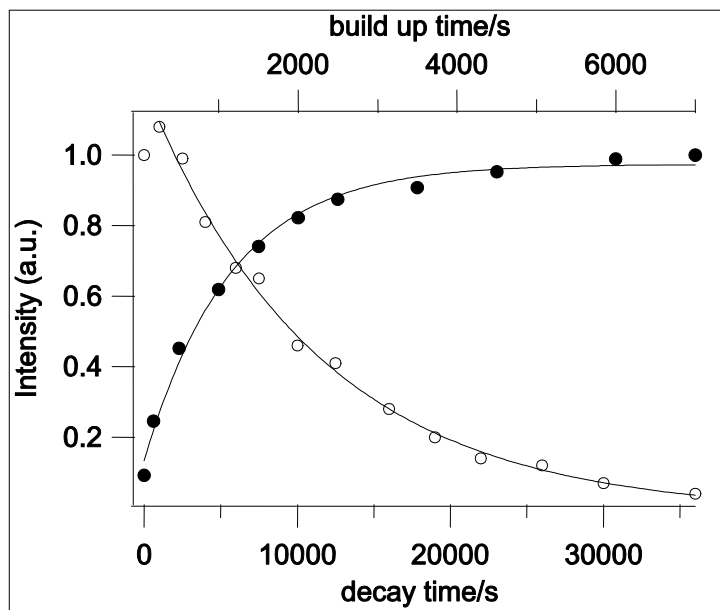
Figure 5.3. A DNP enhanced spectra and a thermally polarized spectrum multiplied 100 times. The enhancement factor is 225. For both spectra, the polarization was allowed to build up for 3500 s after a saturating pulse. Configuration B was used.



The buildup of ^{13}C polarization with microwave irradiation and the decay of polarization after turning off microwave irradiation are shown in Fig. 5.4. The time constant for the buildup of polarization is $\sim 1,090$ s when employing maximum output power (approximately 70 mW) in configuration B. The decay curve gives a ^{13}C nuclear T_1 of 11,360 s. Both curves are fit with single exponentials. Based on the ^{13}C T_1 of 11,360, the unenhanced signal of Fig. 5.3 is only $\sim 26.5\%$ of the full ^{13}C thermal polarization. Thus, we can extrapolate that our largest measured signal (7,000 s build up time in Fig. 5.4) amounts to ~ 65 times that of full thermal polarization, corresponding to 3% nuclear spin polarization. However, it is important to note that since the time constant for nuclear spin polarization buildup with DNP is about 10 times faster than T_1 , the actual gain in NMR detection sensitivity is much greater.

Previous work at 3.35 T and 4.6 T at 1.15 K measured ^{13}C polarizations of $\sim 26\%$ [26, 175] and 58% [177] respectively for a similar sample as studied here. Theory predicts that solid state DNP decreases with increasing field [11, 178, 179], so the result of larger polarization at higher magnetic fields is very interesting. Since no clear theoretical explanation was provided for this observation, it is unclear if this trend is expected to continue at 7 T. The much lower polarization measured here compared to these previous studies is likely due to our smaller electron spin polarization compared to 4.6 T at 1.15 K (82.6% versus 99.1%). It will be interesting in future experiments to see if similar or higher ^{13}C polarization can be reached at 7 T when employing lower temperatures.

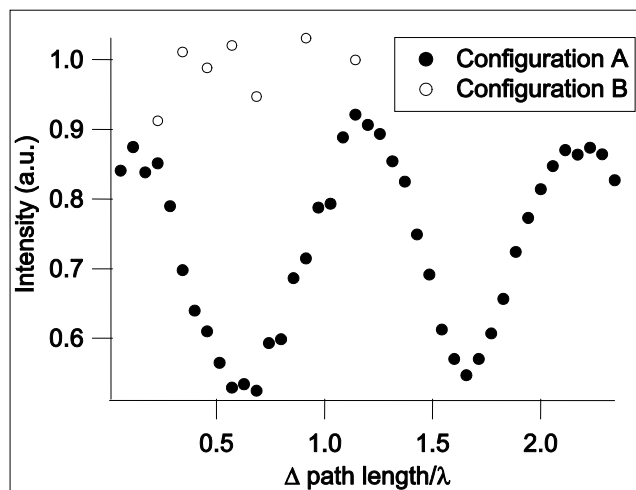
Figure 5.4. The build up (closed circles) of polarization with microwave irradiation and the decay (open circles) of magnetization after 2 hours of microwave irradiation. The solid lines are single exponential fits to the data. Both sets of data were taken using configuration B with ~ 70 mW of microwave power. The second point of the decay curve, taken 1000s after turning off the microwaves, was consistently larger than the point taken immediately after turning off the microwaves. The first point was not included in the fit.



When irradiating a sample, only the component of radiation rotating in the same direction as the precession frequency can cause a spin transition. Thus, the correct handedness of circularly polarized light should give a gain of two in effective power compared to linearly polarized light. To test the extent that the use of circularly polarized radiation increases DNP efficiency, the path length between the two roof mirrors of the Martin-Puplett interferometer was varied in increments of $70\ \mu\text{m}$, and the DNP-amplified NMR signal was recorded after 5 minutes of microwave irradiation. The results are shown in Fig 5.5. Using configuration B and employing maximum microwave power, the signal was not found to vary significantly with mirror position (open circles). However, when the Faraday rotator was included (configuration A), reducing our power to the sample as mentioned above, the expected cosine pattern was observed with a period equal to the wavelength of $1.51\ \text{mm}$ (closed circles in Fig. 5.5) [167]. The maximum of this curve corresponds to the correct handedness of circular polarization irradiating the sample, the minimum to the opposite direction of circularly polarized microwaves, and the inflection points to linear polarization. A gain in signal of 28% was observed for circular versus linear polarization. To verify that this was not due to changes in average power to the sample (which also increases with circular polarization), the path length between the two roof mirrors was varied, and the power at the end of the waveguide measured with a pyroelectric detector. The power reaching the sample had the expected cosine squared pattern [167]. Thus, we conclude that the observed changes in DNP signal

enhancements are from the change in the polarization of radiation, and not due to changes in average power delivered to the sample. This illustrates the advantage of using circular polarization for DNP experiments with sample conditions where one is power limited. Lastly, the improvement from using circular polarization versus linear polarization will depend on the change in saturation of the electron spins. For samples with broader lines, or at higher temperatures, we expect the advantage of using circular polarization to be more pronounced.

Figure 5. The measured DNP signal intensities as a function of the path length difference between the two roof mirrors for the same sample using configuration A (closed circles) and configuration B (open circles). Note that origin of the x-axis does not actually correspond to no path length difference between the two roof mirrors.



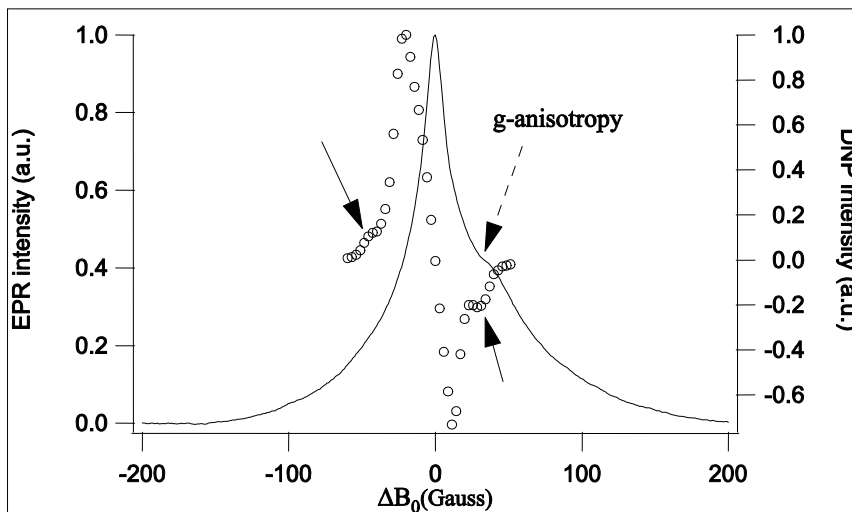
It is interesting that when using the wrong handedness of circular polarization, significant signal enhancement was still observed. We attribute this to small amounts of incorrectly polarized light due to scattering from the off-axis mirror into the waveguide, and scattering at the sample from the sample holder and NMR coil. The scattered polarization losses from an off-axis mirror can be estimated by the Murphy formula, $\Delta P = \frac{1}{4}(W_m/f)^2 \tan(\theta)$, where ΔP is the cross polarization losses, W_m is the

beam waist at the mirror, f is the mirror focal length, and θ is angle of incidence [180]. With $\theta = 45^\circ$ and $(W_m/f)^2 \sim 0.015$, the losses due the off-axis mirror is approximately 0.4% or 24 dB. This represents a lower bound as scattering from the saddle coil and sample are also likely to cause additional polarization losses. Significant enhancements were measured when the source power was attenuated by ~ 25 dB in configuration A, comparable to the enhancement recorded when the wrong handedness of circular polarization is employed. Thus, we believe the enhancements with the wrong handedness of circular polarization shown in Fig. 5.5 are consistent with polarization losses from the off-axis mirror and scattering from the NMR coil and sample.

Our setup also enables the detection of a high field EPR spectrum of the same sample without changes to the setup used for DNP. Only the position of the roof mirror needs to be adjusted so that a linearly polarized beam is incident upon the sample for induction mode detection [158, 162]. The solid line in Fig. 5.6 shows a single scan EPR spectrum of the same sample used for DNP experiments with a single scan signal to noise of ~ 80 . Larger signal to noise ratios were achieved with greater applied power and modulation amplitude, but at the expense of EPR line broadening. The full width at half max linewidth is 38 Gauss, and is comparable to previous measurements of the trityl radical [175, 181, 182]. A small g -anisotropy is observed as reported by others [175], and indicated by the dashed arrow in Fig. 5.6. Homodyne or heterodyne detection can be added into our current setup with little cost to the DNP efficiency as only a small amount of source power needs to be directed to

a mixer. This would greatly increase the EPR sensitivity allowing samples of unknown line-shapes, much broader lines, or lower concentrations to be studied.

Figure 5.6. A single scan, field swept, absorption EPR spectrum of 40 mM trityl (solid line, taken using configuration A) and the frequency swept DNP signal enhancements (open circles, taken using configuration B). The x-axis of the frequency swept data was converted to ΔB_0 for direct comparison with the EPR spectrum. The solid arrows indicate an unexplained DNP effect. The dashed arrow points to the g-anisotropy of the EPR spectrum.



Also shown with the EPR spectrum in Fig. 5.6 are the measured DNP signal intensities (open circles) after 3 minutes of microwave irradiation as the irradiation frequency was varied. The frequency axis was then converted to a ΔB_0 axis so the EPR spectrum and DNP data could be directly compared. The magnetic field could have been swept instead of the irradiation frequency; however, this would have required retuning of the NMR probe for each data point, which is not available in the current setup. The minimum and maximum enhancements are separated by 88 MHz, which is much narrower than the 150 MHz predicted by the solid effect for ^{13}C , indicating that thermal mixing is likely the dominant DNP mechanism. There is also an observed asymmetry in the DNP results. This is likely caused by the asymmetry of

the EPR line due the g-anisotropy. The data does show some evidence of a possible solid effect that is characterized by the maximum and minimum enhancements being located at $\omega = \omega_e \pm \omega_n$ where ω_n is the ^{13}C Larmor frequency [11]. The local minimum on the right side of Fig. 5.6 is located 28.5 Gauss away from the center, very near the 27 Gauss predicted by the solid effect. On the left side of Fig. 5.6, there is no local maximum, though a shoulder is clearly present (indicated by the arrow on the left). However, this shoulder is approximately 40 Gauss from the center, much further than expected for the ^{13}C solid effect. The appearance of a bump in the DNP versus frequency curve was also observed by Jóhannesson et. al. at 4.6 T. In their study, the bump occurred near the frequency expected for a ^1H solid effect, although the details of how this would be transferred to ^{13}C polarization in their experiment was unknown [177]. At 7 T, the ^1H solid effect would occur closer to 100 Gauss instead of 40 Gauss off the center frequency. Thus, this peak does not seem to correspond to location of a ^{13}C or ^1H solid effect and the nature of these peaks is currently unexplained.

D. Conclusion

In this chapter we demonstrated the successful implementation of a quasi-optical EPR bridge equipped with a low power, diode based, and tunable, 200 GHz source into an existing wide bore 7 T NMR magnet for parallel DNP and EPR experiments. The quasi-optical bridge has low loss transmission, excellent isolation from unwanted reflections, and the ability to employ circular polarization to increase the effective microwave power. While the experiments presented here at 4 K were not power

limited, this is not likely to be the case at higher temperatures as T_{1e} gets shorter, or with different samples that have lower DNP efficiencies. We have shown for the first time that a Martin-Puplett interferometer used to irradiate the sample with a circularly polarized microwave beam helps to overcome power limitations by delivering nearly twice the effective power as linear polarization. This resulted in a 28% gain in signal versus linear polarization, and should prove useful in future experiments at higher temperatures.

Our quasi-optical bridge is a versatile instrument for DNP and EPR measurements which also provides the possibility to implement homodyne or heterodyne cw-EPR detection in the future. The entire 200 GHz quasi-optical bridge and setup can be acquired and/or built at relatively low overall cost, and is less demanding on space requirements when compared with a commercially available gyrotron or dissolution DNP setups. These benefits come at the cost of available microwave power compared to a gyrotron, or the inability to quickly shuttle the sample for high resolution liquid NMR as with the dissolution setup. Our cw-DNP and EPR setup ideal applications where simultaneous EPR and DNP characterization provides interesting new information on electron-nuclei interactions. For example, recent work has used DNP to study e^- - nuclei interactions in many different types of silicon samples for applications in solar cells and imaging experiments [153, 183, 184].

VI. Conclusion

The work presented here, in partial consideration for a Ph.D. in physics, marks significant improvements in DNP theory, hardware, and application at both low and high magnetic fields. Nitroxide radicals are the most commonly used spin labels in EPR studies of biomolecules. Nitroxides have also been widely employed in both solution and solid state DNP experiments due to the strong dipolar coupling of the unpaired e^- to the ^1H nuclear spin of water. In solution state, using the Overhauser Effect, the size of the DNP enhancement is very sensitive to the local water dynamics near the nitroxide. Although all this was previously known, it is only recently in the Han group that measuring the DNP signal enhancements of water with spin labeled biomolecules was proposed as a method to study hydration dynamics. However, the three hyperfine states of the nitroxide radical complicate the interpretation of DNP results since the saturation factor can no longer be assumed to $\frac{1}{3}$. My theoretical work on the saturation factor, presented in chapter 2, was a crucial step in applying DNP to quantitatively study hydration dynamics. Also in chapter two, we showed the FFHS model does approximate the NMRD data well, justifying its use to approximate the timescale of the dipolar interaction; however, there is a discrepancy when applying this model to the DNP and NMRD data reflecting its shortcomings. My work in this area helped lead to several publications from the Han group [22-25] and continues to be utilized for current applications.

In chapter four I applied this technique we developed in the Han group to study the problem of protein folding with apoMb. Hydrophobic and hydrophilic interactions

drive the initial collapse of globular proteins, yet these interactions are very difficult to study. Our DNP technique is unique because the NMR signal of water is directly detected, and the size of the DNP signal enhancement is intimately linked to hydration dynamics. We were able to determine that the hydrophobic core of the apoMb appears ‘dry’ on the DNP timescale, but that the core is hydrated in the intermediate MG-state. This was an outstanding question due to the lack of experimental techniques available. We also showed that the hydration landscape is extremely heterogeneous, highlighting the importance of a site specific technique to study these interactions.

In chapters three and five, I show my efforts to improve the hardware used for both X-band, solution state DNP and 7 T DNP. At low magnetic fields, there are no commercial instruments available and so custom hardware must be designed. At the time reference [20] was submitted, our work resulted in the largest measured DNP signal enhancements at X-band frequencies. In contrast to other groups also working at X-band, our amplifier design is very compact and portable and routinely taken to an MRI lab for imaging experiments [98]. At 7 T, I worked to develop a 200 GHz DNP and EPR system using a quasi-optical bridge. The bridge allows us to manipulate the polarization of the microwave beam to optimal conditions for either DNP irradiation, or EPR detection. This was the first demonstration of circularly polarized microwaves being used to improve DNP performance that we are aware of. Additionally, as this instrument allows for both NMR-detected DNP and EPR we will be able to more fully characterize samples in which the e^- - nuclear spin interactions

of interest. Currently investigations are being carried in our out on amorphous silicon samples to study the nature of defects sites, while work is also continuing to be done to improve the instrumentation further. In many ways, if I may take a sentence to interject my personal opinion, it is sad to be leaving at this moment as I expect many interesting applications to come from this instrument that I spent much time working on. I will watch with great interest the work that comes from it.

References

- [1] A. Durazo, and M.M. Abu-Omar, "Deuterium NMR spectroscopy is a versatile and economical tool for monitoring reaction kinetics in ionic liquids." *Chem. Commun.* (2002) 66-67.
- [2] H. Koskela, M.L. Rapinoja, M.L. Kuitunen, and P. Vanninen, "Determination of Trace Amounts of Chemical Warfare Agent Degradation Products in Decontamination Solutions with NMR Spectroscopy." *Anal. Chem.* 79 (2007) 9098-9106.
- [3] K. Wuethrich, "Protein structure determination in solution by NMR spectroscopy." *J. Biol. Chem.* 265 (1990) 22059-22062.
- [4] I.L. Pykett, J.H. Newhouse, F.S. Buonanno, T.J. Brady, M.R. Goldman, J.P. Kistler, and G.M. Pohost, "Principles of nuclear magnetic resonance imaging." *Radiology* 143 (1982) 157-168.
- [5] L.M.K. Vandersypen, M. Steffen, G. Breyta, C.S. Yannoni, M.H. Sherwood, and I.L. Chuang, "Experimental realization of Shor's quantum factoring algorithm using nuclear magnetic resonance." *Nature* 414 (2001) 883-887.
- [6] A.W. Overhauser, "Polarization of Nuclei in Metals." *Phys. Rev.* 92 (1953) 411-415.
- [7] T.R. Carver, and C.P. Slichter, "Polarization of Nuclear Spins in Metals." *Phys. Rev.* 92 (1953) 212.
- [8] A. Abragam, "Overhauser Effect in Nonmetals." *Phys. Rev.* 98 (1955) 1729.
- [9] A. Abragam, and M. Borghini, "Dynamic polarization of nuclear targets." *Progr. Low Temp. Phys.* (C. J. Gorter, Ed.) 4 (1964) 384-449.
- [10] A. Abragam, and M. Goldman, "Principles of Dynamic Nuclear-Polarization." *Rep. Prog. Phys.* 41 (1978) 395-467.
- [11] R.A. Wind, M.J. Duijvestijn, C. van der Lugt, A. Manenschijn, and J. Vriend, "Applications of dynamic nuclear polarization in ^{13}C NMR in solids." *Prog. Nucl. Magn. Reson. Spec.* 7 (1985) 33-67.

- [12] C.T. Farrar, D.A. Hall, G.J. Gerfen, S.J. Inati, and R.G. Griffin, "Mechanism of dynamic nuclear polarization in high magnetic fields." *J. Chem. Phys.* 114 (2001) 4922-4933.
- [13] Z. Guo, D. Cascio, K. Hideg, T. Kálái, and W.L. Hubbell, "Structural determinants of nitroxide motion in spin-labeled proteins: Tertiary contact and solvent-inaccessible sites in helix G of T4 lysozyme." *Protein Sci.* 16 (2007) 1069-1086.
- [14] C.J. López, M.R. Fleissner, Z. Guo, A.K. Kusnetzow, and W.L. Hubbell, "Osmolyte perturbation reveals conformational equilibria in spin-labeled proteins." *Protein Sci.* 18 (2009) 1637-1652.
- [15] L. Zhang, L. Wang, Y.T. Kao, W. Qiu, Y. Yang, O. Okobiah, and D. Zhong, "Mapping hydration dynamics around a protein surface." *Proc. Nat. Acad. Sci. U.S.A.* 104 (2007) 18461-18466.
- [16] L. Zhang, Y. Yang, Y.-T. Kao, L. Wang, and D. Zhong, "Protein Hydration Dynamics and Molecular Mechanism of Coupled Water-Protein Fluctuations." *J. Am. Chem. Soc.* 131 (2009) 10677-10691.
- [17] B. Halle, "Cross-relaxation between macromolecular and solvent spins: The role of long-range dipole couplings." *J. Chem. Phys.* 119 (2003) 12372-12385.
- [18] B.D. Armstrong, and S. Han, "A new model for Overhauser enhanced nuclear magnetic resonance using nitroxide radicals." *J. Chem. Phys.* 127 (2007) 104508-10.
- [19] B.D. Armstrong, and S. Han, "Overhauser Dynamic Nuclear Polarization To Study Local Water Dynamics." *J. Am. Chem. Soc.* 131 (2009) 4641-4647.
- [20] B.D. Armstrong, M.D. Lingwood, E.R. McCarney, E.R. Brown, P. Blümmler, and S. Han, "Portable X-band system for solution state dynamic nuclear polarization." *J. Magn. Reson.* 191 (2008) 273-281.
- [21] D. Eliezer, J. Yao, H.J. Dyson, and P.E. Wright, "Structural and dynamic characterization of partially folded states of apomyoglobin and implications for protein folding." *Nat. Struct. Mol. Biol.* 18 (1998) 148-155.
- [22] R. Kausik, and S. Han, "Ultrasensitive Detection of Interfacial Water Diffusion on Lipid Vesicle Surfaces at Molecular Length Scales." *J. Am. Chem. Soc.* 131 (2009) 18254-18256.

- [23] E.R. McCarney, B.D. Armstrong, R. Kausik, and S. Han, "Dynamic Nuclear Polarization Enhanced Nuclear Magnetic Resonance and Electron Spin Resonance Studies of Hydration and Local Water Dynamics in Micelle and Vesicle Assemblies." *Langmuir* 24 (2008) 10062-10072.
- [24] R. Kausik, A. Srivastava, P.A. Korevaar, G. Stucky, J.H. Waite, and S. Han, "Local Water Dynamics in Coacervated Polyelectrolytes Monitored through Dynamic Nuclear Polarization-Enhanced ^1H NMR." *Macromolecules* 42 (2009) 7404-7412.
- [25] A. Pavlova, E.R. McCarney, D.W. Peterson, F.W. Dahlquist, J. Lew, and S. Han, "Site-specific dynamic nuclear polarization of hydration water as a generally applicable approach to monitor protein aggregation." *Phys. Chem. Chem. Phys.* 11 (2009) 6833-6839.
- [26] J.H. Ardenkjaer-Larsen, B. Fridlund, A. Gram, G. Hansson, L. Hansson, M.H. Lerche, R. Servin, M. Thaning, and K. Golman, "Increase in signal-to-noise ratio of $> 10,000$ times in liquid-state NMR." *Proc. Nat. Acad. Sci. U.S.A.* 100 (2003) 10158-10163.
- [27] V.S. Bajaj, C.T. Farrar, I. Mastovsky, J. Vieregg, J. Bryant, B. Elena, K.E. Kreisler, R.J. Temkin, and R.G. Griffin, "Dynamic nuclear polarization at 9T using a novel 250 GHz gyrotron microwave source." *J. Magn. Reson.* 160 (2003) 85-90.
- [28] C.P. Slichter, *Principles of magnetic resonance*, Springer-Verlag, Berlin; New York, 1990.
- [29] K.H. Hausser, and D. Stehlik, "Dynamic nuclear polarization in liquids." *Advan. Magn. Reson.* 3 (1968) 79-139.
- [30] I. Solomon, "Relaxation Processes in a System of 2 Spins." *Phys. Rev.* 99 (1955) 559-565.
- [31] F. Bloch, "Nuclear Induction." *Phys. Rev.* 70 (1946) 460.
- [32] A. Abragam, *The principles of nuclear magnetism*, Clarendon Press, Oxford, England, 1961.
- [33] G.M. Clore, C. Tang, and J. Iwahara, "Elucidating transient macromolecular interactions using paramagnetic relaxation enhancement." *Curr. Opin. Struct. Biol.* 17 (2007) 603-616.

- [34] B. Liang, J.H. Bushweller, and L.K. Tamm, "Site-Directed Parallel Spin-Labeling and Paramagnetic Relaxation Enhancement in Structure Determination of Membrane Proteins by Solution NMR Spectroscopy." *J. Am. Chem. Soc.* 128 (2006) 4389-4397.
- [35] C.S. Sheng Cai, Z. Kovacs, A.D. Sherry, and Y. Chen, "Sensitivity Enhancement of Multidimensional NMR Experiments by Paramagnetic Relaxation Effects." *J. Am. Chem. Soc.* 128 (2006) 13474-13478.
- [36] J.H. Freed, "Dynamic effects of pair correlation functions on spin relaxation by translational diffusion in liquids. II. Finite jumps and independent T_1 processes." *J. Chem. Phys.* 68 (1978) 4034-4037.
- [37] L. Helm, "Relaxivity in paramagnetic systems: Theory and mechanisms." *Prog. Nucl. Magn. Reson. Spec.* 49 (2006) 45-64.
- [38] L.-P. Hwang, and J.H. Freed, "Dynamic effects of pair correlation functions on spin relaxation by translational diffusion in liquids." *J. Chem. Phys.* 63 (1975) 4017-4025.
- [39] J.-P. Korb, and R.G. Bryant, "The physical basis for the magnetic field dependence of proton spin-lattice relaxation rates in proteins." *J. Chem. Phys.* 15 (2001) 10964-10974.
- [40] J.-P. Korb, and R.G. Bryant, "Magnetic field dependence of proton spin-lattice relaxation times." *Magn. Reson. Med.* 48 (2002) 21-26.
- [41] D. Kruk, T. Nilsson, and J. Kowalewski, "Outer-sphere nuclear spin relaxation in paramagnetic systems: a low-field theory," *Mol. Phys.* 99 (2001), pp. 1435 - 1445.
- [42] É. Tóth, L. Helm, and A. Merbach, "Relaxivity of MRI Contrast Agents." *Contrast Agents I*, 2002, pp. 61-101.
- [43] M.W. Hodges, D.S. Cafiso, C.F. Polnaszek, C.C. Lester, and R.G. Bryant, "Water translational motion at the bilayer interface: an NMR relaxation dispersion measurement." *Biophys. J.* 73 (1997) 2575-2579.
- [44] H. Jansson, F. Kargl, F. Fernandez-Alonso, and J. Swenson, "Dynamics of a protein and its surrounding environment: A quasielastic neutron scattering study of myoglobin in water and glycerol mixtures." *J. Chem. Phys.* 130 (2009) 205101-13.

- [45] J. Qvist, E. Persson, C. Mattea, and B. Halle, "Time scales of water dynamics at biological interfaces: peptides, proteins and cells." *Faraday Discuss.* 141 (2009) 131-144.
- [46] D. Russo, G. Hura, and T. Head-Gordon, "Hydration Dynamics Near a Model Protein Surface." *Biophys. J.* 86 (2004) 1852-1862.
- [47] S. Kiihne, and R.G. Bryant, "Protein-Bound Water Molecule Counting by Resolution of ^1H Spin-Lattice Relaxation Mechanisms." *Biophys. J.* 78 (2000) 2163-2169.
- [48] W.L. Hubbell, A. Gross, R. Langen, and M.A. Lietzow, "Recent advances in site-directed spin labeling of proteins." *Curr. Opin. Struc. Biol.* 8 (1998) 649-656.
- [49] D. Marsh, Electron spin resonance: spin labels. in: E. Grell (Ed.), *Membrane Spectroscopy. Molecular Biology, Biochemistry, and Biophysics*, Springer-Verlag, Berlin, 1981, pp. 51-142.
- [50] O.H. Griffith, P.J. Dehlinger, and S.P. Van, "Shape of the hydrophobic barrier of phospholipid bilayers (Evidence for water penetration in biological membranes)." *J. Membrane Biol.* 15 (1974) 159-192.
- [51] D. Kurad, G. Jeschke, and D. Marsh, "Lipid Membrane Polarity Profiles by High-Field EPR." *Biophys. J.* 85 (2003) 1025-1033.
- [52] S. Stoll, and A. Schweiger, "EasySpin, a comprehensive software package for spectral simulation and analysis in EPR." *J. Magn. Reson.* 178 (2006) 42-55.
- [53] D.E. Budil, S. Lee, S. Saxena, and J.H. Freed, "Nonlinear-Least-Squares Analysis of Slow-Motion EPR Spectra in One and Two Dimensions Using a Modified Levenberg-Marquardt Algorithm." *J. Magn. Reson. A* 120 (1996) 155-189.
- [54] K.A. Earle, and D.E. Budil, "Calculating Slow-Motion ESR Spectra of Spin-Labeled Polymers." in: S. Dr. Shulamith, (Ed.), *Advanced ESR Methods in Polymer Research*, 2006, pp. 53-83.
- [55] J.H. Freed, "Theory of Slow Tumbling ESR Spectra for Nitroxides." in: L.J. Berliner, (Ed.), *Spin Labeling Theory and Applications*, Academic Press, N.Y., 1976, pp. 53-132.

- [56] D.J. Schneider, and J.H. Freed, "Calculating Slo Motional Magnetic Resonance Spectra: A User's Guide." in: L.J. Berliner, and J. Reuben, (Eds.), *Biological Magnetic Resonance*, Plenum, NY, 1989, pp. 1-76.
- [57] R. Owenius, M. Osterlund, M. Lindgren, M. Svensson, O.H. Olsen, E. Persson, P.O. Freskgard, and U. Carlsson, "Properties of spin and fluorescent labels at a receptor-ligand interface." *Biophys. J.* 77 (1999) 2237-2250.
- [58] M. Alecci, I. Seimenis, S.J. McCallum, D.J. Lurie, and M.A. Foster, "Nitroxide free radical clearance in the live rat monitored by radio-frequency CW-EPR and PEDRI." *Phys. Med. Biol.* 43 (1998) 1899-1905.
- [59] W. Barros, and M. Engelsberg, "Enhanced Overhauser contrast in proton-electron double-resonance imaging of the formation of an alginate hydrogel." *J. Magn. Reson.* 184 (2007) 101-107.
- [60] D.J. Lurie, "Proton-electron double-resonance imaging (PEDRI)." *Biol. Magn. Reson.* 18 (2003) 547-578.
- [61] D.J. Lurie, D.M. Bussell, L.H. Bell, and J.R. Mallard, "Proton-electron double magnetic resonance imaging of free radical solutions." *J. Magn. Reson.* 76 (1988) 366-70.
- [62] D.J. Lurie, G.R. Davies, M.A. Foster, and J.M.S. Hutchison, Field-cycled PEDRI imaging of free radicals with detection at 450 mT. *Magnetic Resonance Imaging* 23 (2005) 175-181.
- [63] D.J. Lurie, M.A. Foster, D. Yeung, and J.M. Hutchison, "Design, construction and use of a large-sample field-cycled PEDRI imager." *Phys. Med. Biol.* 43 (1998) 1877-86.
- [64] D.J. Lurie, H. Li, S. Petryakov, and J. L. Zweier, "Development of a PEDRI free-radical imager using a 0.38 T clinical MRI system." *Magn. Reson. Med.* 47 (2002) 181-6.
- [65] A.M.F. Benial, K. Ichikawa, R. Murugesan, K. Yamada, and H. Utsumi, "Dynamic nuclear polarization properties of nitroxyl radicals used in Overhauser-enhanced MRI for simultaneous molecular imaging." *J. Magn. Reson.* 182 (2006) 273-282.
- [66] D. Grucker, T. Guiberteau, B. Eclancher, J. Chambron, R. Chiarelli, A. Rassat, G. Subra, and B. Gallez, "Dynamic Nuclear-Polarization with Nitroxides Dissolved in Biological-Fluids." *J. Magn. Reson. B* 106 (1995) 101-109.

- [67] I. Nicholson, D.J. Lurie, and F.J.L. Robb, "The Application of Proton-Electron Double-Resonance Imaging Techniques to Proton Mobility Studies." *J. Magn. Reson. B* 104 (1994) 250-255.
- [68] B.H. Robinson, D.A. Haas, and C. Mailer, "Molecular-Dynamics in Liquids - Spin-Lattice Relaxation of Nitroxide Spin Labels." *Science* 263 (1994) 490-493.
- [69] R.D. Bates, and W.S. Drozdowski, "Use of Nitroxide Spin Labels in Studies of Solvent-Solute Interactions." *J. Chem. Phys.* 67 (1977) 4038-4044.
- [70] W.L. DeLano, The PyMOL Molecular Graphics System. DeLano Scientific LLC Palo Alto, CA (2008).
- [71] D. Sezer, M. Gafurov, M.J. Prandolini, V.P. Denysenkov, and T.F. Prisner, "Dynamic nuclear polarization of water by a nitroxide radical: rigorous treatment of the electron spin saturation and comparison with experiments at 9.2 Tesla." *Phys. Chem. Chem. Phys.* 11 (2009) 6638-6653.
- [72] J.A. Weil, J.R. Bolton, and J.E. Wertz, *Electron paramagnetic resonance: elementary theory and practical applications*, Wiley, New York, 1994.
- [73] D.W. Peterson, H. Zhou, F.W. Dahlquist, and J. Lew, "A Soluble Oligomer of Tau Associated with Fiber Formation Analyzed by NMR." *Biochemistry.* 47 (2008) 7393-7404.
- [74] E.R. McCarney, and S. Han, "Spin-labeled gel for the production of radical-free dynamic nuclear polarization enhanced molecules for NMR spectroscopy and imaging." *J. Magn. Reson.* 190 (2008) 307-315.
- [75] E.R. McCarney, B.D. Armstrong, M.D. Lingwood, and S. Han, "Hyperpolarized water as an authentic magnetic resonance imaging contrast agent." *Proc. Nat. Acad. Sci. U.S.A.* 104 (2007) 1754-1759.
- [76] P. Hofer, G. Parigi, C. Luchinat, P. Carl, G. Guthausen, M. Reese, T. Carlomagno, C. Griesinger, and M. Bennati, "Field Dependent Dynamic Nuclear Polarization with Radicals in Aqueous Solution." *J. Am. Chem. Soc.* 130 (2008), pp. 3254-3255.
- [77] C.F. Polnaszek, and R.G. Bryant, "Nitroxide radical induced solvent proton relaxation: Measurement of localized translational diffusion." *J. Chem. Phys.* 81 (1984) 4038-4045.
- [78] C.L. Teng, S. Martini, and R.G. Bryant, "Local Measures of Intermolecular Free Energies in Solution." *J. Am. Chem. Soc.* 126 (2004) 15253-15257.

- [79] D. Sezer, M.J. Prandolini, and T.F. Prisner, "Dynamic nuclear polarization coupling factors calculated from molecular dynamics simulations of a nitroxide radical in water." *Phys. Chem. Chem. Phys.* 11 (2009) 6626-6637.
- [80] C.C. Lester, and R.G. Bryant, "Outer coordination sphere: characterization by nuclear magnetic relaxation dispersion." *J. Phys. Chem.* 94 (1990), pp. 2843-2847.
- [81] C.F. Polnaszek, and R.G. Bryant, "Self-diffusion of water at the protein surface: a measurement." *J. Am. Chem. Soc.* 106 (1984) 428-429.
- [82] M. Pavone, P. Cimino, O. Crescenzi, A. Sillanpaa, and V. Barone, "Interplay of Intrinsic, Environmental, and Dynamic Effects in Tuning the EPR Parameters of Nitroxides: Further Insights from an Integrated Computational Approach." *J. Phys. Chem. B* 111 (2007) 8928-8939.
- [83] M. Pavone, A. Sillanpaa, P. Cimino, O. Crescenzi, and V. Barone, "Evidence of Variable H-Bond Network for Nitroxide Radicals in Protic Solvents." *J. Phys. Chem. B* 110 (2006) 16189-16192.
- [84] D. van der Spoel, P.J. van Maaren, and H.J.C. Berendsen, "A systematic study of water models for molecular simulation: Derivation of water models optimized for use with a reaction field." *J. Chem. Phys.* 108 (1998) 10220-10230.
- [85] H.J.C. Berendsen, D. van der Spoel, and R. van Drunen, "GROMACS: A message-passing parallel molecular dynamics implementation." *Comput. Phys. Commun.* 91 (1995) 43-56.
- [86] W.L. Jorgensen, and J. Tirado-Rives, "The OPLS [optimized potentials for liquid simulations] potential functions for proteins, energy minimizations for crystals of cyclic peptides and crambin." *J. Am. Chem. Soc.* 110 (1988) 1657-1666.
- [87] G.A. Kaminski, R.A. Friesner, J. Tirado-Rives, and W.L. Jorgensen, "Evaluation and Reparametrization of the OPLS-AA Force Field for Proteins via Comparison with Accurate Quantum Chemical Calculations on Peptides." *J. Phys. Chem. B* 105 (2001) 6474-6487.
- [88] W.L. Jorgensen, J. Chandrasekhar, J.D. Madura, R.W. Impey, and M.L. Klein, "Comparison of simple potential functions for simulating liquid water." *J. Chem. Phys.* 79 (1983) 926-935.
- [89] H.J.C. Berendsen, J.R. Grigera, and T.P. Straatsma, "The missing term in effective pair potentials." *J. Phys. Chem.* 91 (1987) 6269-6271.

- [90] H.J.C. Berendsen, J.P.M. Postma, W.F. van Gunsteren, A. DiNola, and J.R. Haak, "Molecular dynamics with coupling to an external bath." *J Chem. Phys.* 81 (1984) 3684-3690.
- [91] B. Hess, H. Bekker, H.J.C. Berendsen, and J.G.E.M. Fraaije, "LINCS: A linear constraint solver for molecular simulations." *J. Comput. Chem.* 18 (1997) 1463-1472.
- [92] S. Miyamoto, and P.A. Kollman, "Settle: An analytical version of the SHAKE and RATTLE algorithm for rigid water models." *J. Comput. Chem.* 13 (1992) 952-962.
- [93] U. Essmann, L. Perera, M.L. Berkowitz, T. Darden, H. Lee, and L.G. Pedersen, "A smooth particle mesh Ewald method." *J. Chem. Phys.* 103 (1995) 8577-8593.
- [94] G. Schaftenaar, and J.H. Noordik, "Molden: a pre- and post-processing program for molecular and electronic structures." *J. Comput. Aid. Mol. Des.* 14 (2000) 123-134.
- [95] M.J. Frisch, and et. al, Gaussian 03, Revision D.02. Gaussian, Inc. Wallingford, CT. (2004).
- [96] C.I. Bayly, P. Cieplak, W. Cornell, and P.A. Kollman, "A well-behaved electrostatic potential based method using charge restraints for deriving atomic charges: the RESP model." *J. Phys. Chem.* 97 (1993) 10269-10280.
- [97] M.D. Lingwood, I.A. Ivanov, A.R. Cote, and S. Han, "Heisenberg spin exchange effects of nitroxide radicals on Overhauser dynamic nuclear polarization in the low field limit at 1.5 mT." *J. Magn. Reson.* 204 (2010) 56-63.
- [98] M.D. Lingwood, T.A. Siaw, N. Sailasuta, B.D. Ross, P. Bhattacharya, and S. Han, "Continuous flow Overhauser dynamics nuclear polarization of water in the fringe field of a clinical magnetic resonance imaging system for authentic image contrast." *J. Magn. Reson.* under review (2010).
- [99] W.E. Forsythe, Smithsonian Physical Tables, 9th revised ed., Knovel, 1954/2003, pp. 319.
- [100] K. Halbach, "Strong rare earth cobalt quadrupoles." *IEEE Trans. Nucl. Sci.* 26 (1979) 3882-3884.

- [101] T.R. Ni Mhiochain, J.M.D. Coey, D.L. Weaire, and S.M. McMurry, "Torque in nested Halbach cylinders." *IEEE Trans. Magn.* 35 (1999) 3968-3970.
- [102] H. Raich, and P. Blümler, "Design and construction of a dipolar Halbach array with a homogeneous field from identical bar magnets: NMR Mandhalas." *Concept. Magn. Reson. B* 23B (2004) 16-25.
- [103] D. Chandler, "Interfaces and the driving force of hydrophobic assembly." *Nature* 437 (2005) 640-647.
- [104] M.S. Cheung, A.E. Garcia, and J.N. Onuchic, "Protein folding mediated by solvation: Water expulsion and formation of the hydrophobic core occur after the structural collapse." *Proc. Nat. Acad. Sci. U.S.A.* 99 (2002) 685-690.
- [105] R. Zhou, X. Huang, C.J. Margulis, and B.J. Berne, "Hydrophobic Collapse in Multidomain Protein Folding." *Science* 305 (2004) 1605-1609.
- [106] K.A. Dill, "Dominant Forces in Protein Folding." *Biochemistry* 29 (1990) 7133-7155.
- [107] T. Kamei, M. Oobatake, and M. Suzuki, "Hydration of Apomyoglobin in Native, Molten Globule, and Unfolded States by Using Microwave Dielectric Spectroscopy." *Biophys. J.* 82 (2002) 418-425.
- [108] V.P. Denisov, B.H. Jonsson, B. Halle, "Hydration of denatured and molten globule proteins." *Nat. Struct. Biol.* 6 (1999) 253-260.
- [109] S.K. Jha, and J.B. Udgaonkar, "Direct evidence for a dry molten globule intermediate during the unfolding of a small protein." *Proc. Nat. Acad. Sci. U.S.A.* 106 (2009) 12289-12294.
- [110] A. Onufriev, D.A. Case, and D. Bashford, "Structural details, pathways, and energetics of unfolding apomyoglobin." *J. Mol. Biol.* 325 (2003) 555-567.
- [111] B.R. Rami, and J.B. Udgaonkar, "Mechanism of formation of a productive molten globule form of barstar." *Biochemistry* 41 (2002) 1710-1716.
- [112] O.B. Ptitsyn, D.A. Dolgikh, R.I. Gilmanishin, E.I. Shakhnovich, and A.V. Finkelshtein, "Oscillating State of the Protein Globule." *Mol. Biol.* 17 (1983) 451-456.
- [113] P.W. Fenimore, H. Frauenfelder, B.H. McMahon, and R.D. Young, "Bulk-solvent and hydration-shell fluctuations, similar to \hat{I}_{\pm} - and \hat{I}^2 -fluctuations in glasses, control protein motions and functions." *Proc. Nat. Acad. Sci. U.S.A.* 101 (2004) 14408-14413.

- [114] B. Halle, and L. Nilsson, "Does the Dynamic Stokes Shift Report on Slow Protein Hydration Dynamics?" *J. Phys. Chem. B* 113 (2009) 8210-8213.
- [115] M.E. Johnson, Malardier-Jugroot, C., Murarka, R. K., Head-Gordon, T., "Hydration water dynamics near biological interfaces." *J. Phys. Chem. B* 113 (2009) 4082-4092.
- [116] J.M. Sorenson, G. Hura, A.K. Soper, A. Pertsemliadis, and T. Head-Gordon, "Determining the role of hydration forces in protein folding." *J. Phys. Chem. B* 103 (1999) 5413-5426.
- [117] M. Davidovic, C. Mattea, J. Qvist, and B. Halle, "Protein Cold Denaturation as Seen From the Solvent." *J. Am. Chem. Soc.* 131 (2008) 1025-1036.
- [118] V.P. Denisov, B.H. Jonsson, and B. Halle, "Hydration of denatured and molten globule proteins." *Nat. Struct. Biol.* 6 (1999) 253-260.
- [119] E. Persson, and B. Halle, "Cell water dynamics on multiple time scales." *Proc. Nat. Acad. Sci. U.S.A.* 105 (2008) 6266-6271.
- [120] K. Venu, L. Anders Svensson, and B. Halle, "Orientational Order and Dynamics of Hydration Water in a Single Crystal of Bovine Pancreatic Trypsin Inhibitor." *Biophys. J.* 77 (1999) 1074-1085.
- [121] H. Nakagawa, Joti, Y., Kitao, A., Kataoka, M., "Hydration affects both harmonic and anharmonic nature of protein dynamics." *Biophys. J.* 95 (2008) 2916-2923.
- [122] D. Russo, G.L. Hura, J.R.D.Copley, "Effects of hydration water on protein methyl group dynamics in solution." *Phys. Rev. E* 75 (2007) 040902-1-3.
- [123] D. Russo, G. Hura, and T. Head-Gordon, "Hydration Dynamics Near a Model Protein Surface." *Biophys. J.* 86 (2004) 1852-1862.
- [124] J.C. Smith, "Protein dynamics: comparison of simulations with inelastic neutron scattering experiments." *Q. Rev. Biophys.* 24 (1991) 227-291.
- [125] J.M. Zanotti, G. Hervé, and M.C. Bellissent-Funel, "Picosecond dynamics of T and R forms of aspartate transcarbamylase: A neutron scattering study." *BBA - Proteins Proteom.* 1764 (2006) 1527-1535.

- [126] J.J. Dwyer, A.G. Gittis, D.A. Karp, E.E. Lattman, D.S. Spencer, W.E. Stites, and B. García-Moreno E, "High Apparent Dielectric Constants in the Interior of a Protein Reflect Water Penetration." *Biophys. J.* 79 (2000) 1610-1620.
- [127] T. Kamei, M. Oobatake, and M. Suzuki, "Hydration of Apomyoglobin in Native, Molten Globule, and Unfolded States by Using Microwave Dielectric Spectroscopy." *Biophys. J.* 82 (2002) 418-425.
- [128] U. Heugen, Schwaab, G., Bruendermann, E., Heyden, M., Yu, X., Leitner, D. M., Havenith, M., "Solute-induced retardation of water dynamics probed directly by terahertz spectroscopy." *Proc. Nat. Acad. Sci. U.S.A.* 103 (2006) 12301-123-6.
- [129] S.K. Pal, Peon, J., Zewail, A. H., "Biological water at the protein surface: dynamical solvation probed directly with femtosecond resolution." *Proc. Nat. Acad. Sci. U.S.A.* 99 (2002) 1763-1768.
- [130] S.K. Pal, Peon, J., Zewail, A. H., "Ultrafast surface hydration dynamics and expression of protein functionality: α -Chymotrypsin." *Proc. Nat. Acad. Sci. U.S.A.* 99 (2002) 15297-15302.
- [131] T. Li, A.A. Hassanali, Y.-T. Kao, D. Zhong, and S.J. Singer, "Hydration Dynamics and Time Scales of Coupled Water-Protein Fluctuations." *J. Am. Chem. Soc.* 129 (2007) 3376-3382.
- [132] S. Cavagnero, C. Nishimura, S. Schwarzinger, H.J. Dyson, and P.E. Wright, "Conformational and Dynamic Characterization of the Molten Globule State of an Apomyoglobin Mutant with an Altered Folding Pathway." *Biochemistry* 40 (2001) 14459-14467.
- [133] D. Eliezer, J. Chung, H.J. Dyson, and P.E. Wright, "Native and Non-native Secondary Structure and Dynamics in the pH 4 Intermediate of Apomyoglobin." *Biochemistry* 39 (2000) 2894-2901.
- [134] D. Eliezer, P.A. Jennings, H.J. Dyson, and P.E. Wright, "Populating the equilibrium molten globule state of apomyoglobin under conditions suitable for structural characterization by NMR." *FEBS Lett.* 417 (1997) 92-96.
- [135] D. Eliezer, and P.E. Wright, Is Apomyoglobin a Molten Globule? "Structural Characterization by NMR." *J. Mol. Biol.* 263 (1996) 531-538.

- [136] V. Tsui, C. Garcia, S. Cavagnero, G. Siuzdak, H.J. Dyson, and P.E. Wright, "Quench-flow experiments combined with mass spectrometry show apomyoglobin folds through an obligatory intermediate." *Protein Science* 8 (1999) 45-49.
- [137] C. Nishimura, H.J. Dyson, and P.E. Wright, "Enhanced picture of protein-folding intermediates using organic solvents in H/D exchange and quench-flow experiments." *Proc. Nat. Acad. Sci. U.S.A* 102 (2005) 4765-4770.
- [138] T. Uzawa, C. Nishimura, S. Akiyama, K. Ishimori, S. Takahashi, H.J. Dyson, and P.E. Wright, "Hierarchical folding mechanism of apomyoglobin revealed by ultra-fast H/D exchange coupled with 2D NMR." *Proc. Nat. Acad. Sci. U.S.A.* 105 (2008) 13859-13864.
- [139] A.M. Bertagna, and D. Barrick, Nonspecific hydrophobic interactions stabilize an equilibrium intermediate of apomyoglobin at a key position within the AGH region. *Proc. Nat. Acad. Sci. U.S.A.* 101 (2004) 12514-12519.
- [140] J. Kuriyan, S. Wilz, M. Karplus, and G.A. Petsko, "X-Ray Structure and Refinement of Carbon-Monoxide (Fe-II)-Myoglobin at 1.5-Å Resolution." *J. Mol. Biol.* 192 (1986) 133-154.
- [141] B.D. Armstrong, P. Soto, J.-E. Shea, and S. Han, "Overhauser dynamic nuclear polarization and molecular dynamics simulations using pyrroline and piperidine ring nitroxide radicals." *J. Magn. Reson.* 200 (2009) 137-141.
- [142] V.A. Makarov, B.K. Andrews, P.E. Smith, and B.M. Pettitt, "Residence Times of Water Molecules in the Hydration Sites of Myoglobin." *Biophys. J.* 79 (2000) 2966-2974.
- [143] C.C. Chow, C. Chow, V. Raghunathan., T.J. Huppert, E.B. Kimball, and C. S. Cavagnero, "Chain length dependence of apomyoglobin folding: structural evolution from misfolded sheets to native helices." *Biochemistry* 42 (2003).
- [144] P.A. Jennings, M.J. Stone, and P.E. Wright, "Overexpression of myoglobin and assignment of its amide, α - and β -resonances." *J. Biomol. NMR* 6 (1995) 271-276.
- [145] V.S. Bajaj, M.L. Mak-Jurkauskas, M. Belenky, J. Herzfeld, and R.G. Griffin, "Functional and shunt states of bacteriorhodopsin resolved by 250 GHz dynamic nuclear polarization enhanced solid-state NMR." *Proc. Nat. Acad. Sci. U.S.A.* 106 (2009) 9244-9249.

- [146] M. Rosay, A.C. Zeri, N.S. Astrof, S.J. Opella, J. Herzfeld, and R.G. Griffin, "Sensitivity-enhanced NMR of biological solids: dynamic nuclear polarization of Y21M fd bacteriophage and purple membrane." *J. Am. Chem. Soc.* 123 (2001) 1010-1011.
- [147] C. Hilty, G. Wider, C. Fernandez, and K. Wuethrich, "Membrane protein - lipid interactions in mixed micelles studied by NMR spectroscopy with the use of paramagnetic reagents." *ChemBioChem* 5 (2004) 467-473.
- [148] S. Bowen, and C. Hilty, "Temporal Chemical Shift Correlations in Reactions Studied by Hyperpolarized Nuclear Magnetic Resonance." *Anal. Chem.* 81 (2009) 4543-4547.
- [149] S. Bowen, and C. Hilty, "Time-Resolved Dynamic Nuclear Polarization Enhanced NMR Spectroscopy." *Angew. Chem. Int. Ed.* 47 (2008) 5235-5237.
- [150] K. Golman, R. Zandt, and M. Thaning, "Real-time metabolic imaging." *Proc. Nat. Acad. Sci. U.S.A.* 103 (2006) 11270-11275.
- [151] L. Frydman, and D. Blazina, "Ultrafast two-dimensional nuclear magnetic resonance spectroscopy of hyperpolarized solutions." *Nat. Phys.* 3 (2007) 415-419.
- [152] V. Weis, and R.G. Griffin, "Electron-nuclear cross polarization." *Solid State Nucl. Magn. Reson.* 29 (2006) 66-78.
- [153] D.R. McCamey, J. van Tol, G.W. Morley, and C. Boehme, "Fast Nuclear Spin Hyperpolarization of Phosphorus in Silicon." *Phys. Rev. Lett.* 102 (2009) 027601.
- [154] G.W. Morley, J. van Tol, A. Ardavan, K. Porfyraakis, J. Zhang, and G.A.D. Briggs, "Efficient Dynamic Nuclear Polarization at High Magnetic Fields." *Phys. Rev. Lett.* 98 (2007) 220501.
- [155] K.N. Hu, H.h. Yu, T.M. Swager, and R.G. Griffin, "Dynamic Nuclear Polarization with Biradicals." *J. Am. Chem. Soc.* 126 (2004) 10844-10845.
- [156] Y. Matsuki, T. Maly, O. Ouari, H. Karoui, F. Le Moigne, E. Rizzato, S. Lyubenova, J. Herzfeld, T. Prisner, P. Tordo, and Robert G. Griffin, "Dynamic Nuclear Polarization with a Rigid Biradical." *Angew. Chem. Int. Ed.* 48 (2009) 4996-5000.

- [157] H. Blok, J.A.J.M. Disselhorst, S.B. Orlinskii, and J. Schmidt, "A continuous-wave and pulsed electron spin resonance spectrometer operating at 275 GHz." *J. Magn. Reson.* 166 (2004) 92-99.
- [158] K.A. Earle, Freed, J.H., "Quasioptical Hardware for a Flexible FIR-EPR Spectrometer." *App. Magn. Reson.* 16 (1999) 26.
- [159] K.A. Earle, D.E. Budil, J.H. Freed, and S.W. Warren, "Millimeter wave electron spin resonance using quasioptical techniques." *Advan. Magn. Opt. Reson.* Academic Press (1996) 253-323.
- [160] W. Hofbauer, K.A. Earle, C.R. Dunnam, J.K. Moscicki, and J.H. Freed, "High-power 95 GHz pulsed electron spin resonance spectrometer." *Rev. Sci. Instrum.* 75 (2004) 1194-1208.
- [161] B. Náfrádi, R. Gaál, A. Sienkiewicz, T. Fehér, and L. Forró, "Continuous-wave far-infrared ESR spectrometer for high-pressure measurements." *J. Magn. Reson.* 195 (2008) 206-210.
- [162] G.M. Smith, J.C.G. Lesurf, R.H. Mitchell, and P.C. Riedi, "Quasi-optical cw mm-wave electron spin resonance spectrometer." *Rev. Sci. Instrum.* 69 (1998) 3924-3937.
- [163] S. Takahashi, D.G. Allen, J. Seifter, G. Ramian, M.S. Sherwin, L.-C. Brunel, and J. van Tol, "Pulsed EPR spectrometer with injection-locked UCSB free-electron laser." *Infrared Phys. Techn.* 51 (2008) 426-428.
- [164] J. van Tol, L.C. Brunel, and R.J. Wylde, "A quasioptical transient electron spin resonance spectrometer operating at 120 and 240 GHz." *Rev. Sci. Instrum.* 76 (2005) 074101-8.
- [165] W.B. Lynch, K.A. Earle, and J.H. Freed, "1-mm wave ESR spectrometer." *Rev. Sci. Instrum.* 59 (1988) 1345-1351.
- [166] P.A.S. Cruickshank, D.R. Bolton, D.A. Robertson, R.I. Hunter, R.J. Wylde, and G.M. Smith, "A kilowatt pulsed 94 GHz electron paramagnetic resonance spectrometer with high concentration sensitivity, high instantaneous bandwidth, and low dead time." *Rev. Sci. Instrum.* 80 (2009) 103102-15.
- [167] D.H. Martin, and E. Puplett, "Polarised interferometric spectrometry for the millimetre and submillimetre spectrum." *Infrared Phys.* 10 (1969) 105-109.

- [168] M.J. Prandolini, V.P. Denysenkov, M. Gafurov, B. Endeward, and T.F. Prisner, "High-Field Dynamic Nuclear Polarization in Aqueous Solutions." *J. Am. Chem. Soc.* 131 (2009) 6090-6092.
- [169] K.R. Thurber, W.-M. Yau, and R. Tycko, "Low-Temperature Dynamic Nuclear Polarization at 9.4 Tesla With a 30 Milliwatt Microwave Source." *J. Magn. Reson.* 10.1016/j.jmr.2010.01.016 (2010).
- [170] D.H. Martin, and R.J. Wylde, "Wideband Circulators for Use at Frequencies Above 100 GHz to Beyond 350 GHz." *IEEE Trans. Microw. Theory* 57 (2009) 99-108.
- [171] H. Kogelnik, and T. Li, "Laser Beams and Resonators." *Appl. Optics* 5 (1966) 1550-1567.
- [172] A. Balkcum, R. Ellis, D. Boyd, and S. Guharay, "Generation of millimeter wave Gaussian beams and their propagation in a dielectric waveguide." *Int. J. Infrared Milli.* 13 (1992) 1321-1340.
- [173] T. Stich, S. Lahiri, G. Yeagle, M. Dicus, M. Brynda, A. Gunn, C. Aznar, V. DeRose, and R. Britt, "Multifrequency pulsed EPR studies of biologically relevant manganese(II) complexes." *Appl. Magn. Reson.* 31 (2007) 321-341.
- [174] R.R. Ernst, "Numerical Hilbert transform and automatic phase correction in magnetic resonance spectroscopy." *J. Magn. Reson.* 1 (1969) 7-26.
- [175] J.H. Ardenkjaer-Larsen, S. Macholl, and H. Jóhannesson, "Dynamic Nuclear Polarization with Trityls at 1.2 K." *Appl. Magn. Reson.* 34 (2008) 509-522.
- [176] P. Belland, and J.P. Crenn, "Matching of a Gaussian beam into hollow oversized circular waveguides." *Int. J. Infrared Milli.* 10 (1989) 1279-1287.
- [177] H. Jóhannesson, S. Macholl, and J.H. Ardenkjaer-Larsen, "Dynamic Nuclear Polarization of [1-¹³C]pyruvic acid at 4.6 tesla." *J. Magn. Reson.* 197 (2009) 167-175.
- [178] L.R. Becerra, G.J. Gerfen, R.J. Temkin, D.J. Singel, and R.G. Griffin, "Dynamic nuclear polarization with a cyclotron resonance maser at 5 T." *Phys. Rev. Lett.* 71 (1993) 3561.
- [179] G.J. Gerfen, L.R. Becerra, D.A. Hall, R.G. Griffin, R.J. Temkin, and D.J. Singel, "High frequency (140 GHz) dynamic nuclear polarization: polarization transfer to a solute in frozen aqueous solution." *J. Chem. Phys.* 102 (1995) 9494-7.

- [180] J.A. Murphy, "Distortion of a simple Gaussian beam on reflection from off-axis ellipsoidal mirrors." *Int. J. Infrared Milli.* 8 (1987) 1165-1187.
- [181] J. Granwehr, J. Leggett, and W. Köckenberger, "A low-cost implementation of EPR detection in a dissolution DNP setup." *J. Magn. Reson.* 187 (2007) 266-276.
- [182] K.N. Hu, V.S. Bajaj, M. Rosay, and R.G. Griffin, "High-frequency dynamic nuclear polarization using mixtures of TEMPO and trityl radicals." *J. Chem. Phys.* 126 (2007) 044512.
- [183] J.W. Aptekar, M.C. Cassidy, A.C. Johnson, R.A. Barton, M. Lee, A.C. Ogier, C. Vo, M.N. Anahtar, Y. Ren, S.N. Bhatia, C. Ramanathan, D.G. Cory, A.L. Hill, R.W. Mair, M.S. Rosen, R.L. Walsworth, and C.M. Marcus, "Silicon Nanoparticles as Hyperpolarized Magnetic Resonance Imaging Agents." *ACS Nano* 3 (2009) 4003-4008.
- [184] A.E. Dementyev, D.G. Cory, and C. Ramanathan, Dynamic Nuclear Polarization in Silicon Microparticles. *Phys. Rev. Lett.* 100 (2008) 127601.